THERMODYNAMIC EQUILIBRIUM AND CLOUD DYNAMICS OF ORGANIC AEROSOLS

Yi Ming

A DISSERTATION
PRESENTED TO THE FACULTY
OF PRINCETON UNIVERSITY
IN CANDIDACY FOR THE DEGREE
OF DOCTOR OF PHILOSOPHY

RECOMMENDED FOR ACCEPTANCE
BY THE DEPARTMENT OF
CIVIL AND ENVIRONMENTAL ENGINEERING

December 2002

I certify that I have read this thesis and that in my opinion it is fully adequate, in scope and in quality, as a dissertation for the degree of Doctor of Philosophy.

Lynn M. Russell
(Principal Adviser)

I certify that I have read this thesis and that in my opinion it is fully adequate, in scope and in quality, as a dissertation for the degree of Doctor of Philosophy.

Catherine A. Peters

I certify that I have read this thesis and that in my opinion it is fully adequate, in scope and in quality, as a dissertation for the degree of Doctor of Philosophy.

Approved for the Princeton University Graduate School:

Dean of the Graduate School

Preface

This thesis tells you all you need to know about...

Acknowledgements

I would like to thank...

Contents

Chapter 1

Introduction

A technical definition of aerosol is "a suspension of fine solid or liquid particles in gas" (Seinfeld and Pandis, 1998). Various natural and anthropogenic sources (i.e. dessert dust, sea spray, volcanos and combustion of diesel) give rise to aerosol in the atmosphere. As long as aerosol particles remain airborne, their size and composition can be altered by condensation of gas species, coagulation with other particles, chemical reaction and activation to droplets in the presence of supersaturated water vapor. Aerosol is eventually removed from the atmosphere through depositing at the Earth's surface (dry deposition) and raining out after being incorporated into droplets (wet deposition). Both mechanisms lead to relatively short residence times of aerosol in the troposphere, which vary only from a few days to a few weeks.

Aerosol reduces the short-wave radiation reaching the Earth's surface through direct and indirect effects. In cloudless sky, aerosol particles directly backscatter and absorb incoming sunlight resulting in a decrease in the net radiative forcing at the top-of-atmosphere (TOA) and net cooling. In the presence of cloud, aerosol particles can act as cloud condensation nuclei (CCN), increasing cloud albedo and lifetime. This indirect effect is also estimated to be a net cooling. For example, sulfate aerosol from burning sulfur-containing fuels has a direct radiative forcing estimated at -0.95

W m^{-2} (Adams et al., 2001), counteracting about 60% of the warming effect of CO_2 (1.5 W m^{-2}).

There is growing epidemiological evidence identifying substantial economic costs from air pollution (Hall et al., 1992). The economic costs of human health damage due to air pollution have been estimated for the UK to be 2.7% of GNP (Pearce and Crowards, 1994) and for China 11.1% of GNP (Florig, 1993). Aerosol is playing an important role in shaping the look of our environment in the twenty-first century.

Aerosol particles in the atmosphere often consist of complex mixtures of inorganic and organic components (Duce et al., 1983; Rogge et al., 1993; Middlebrook et al., 1998). As a result of the presence of water-soluble components, dry aerosol particles can absorb water to grow into bigger wet particles in humid air. This behavior is defined as hygroscopic growth. The estimated direct radiative forcing of aerosol is very sensitive to its hygroscopic property (Adams et al., 2001) Soluble components also enable particles to activate as cloud condensation nuclei (CCN) in meteorological conditions favorable for supersaturation. The CCN efficiency of aerosol affects the albedo and lifetime of cloud, both of which are crucial for understanding indirect radiative forcing.

Organic compounds are emitted into the atmosphere by a variety of natural and anthropogenic sources. Organic species account for up to 50% of the total aerosol mass at marine and urban locations (Middlebrook et al., 1998; Turpin et al., 1991). The amount of water absorbed by aerosol particles at subsaturated relative humidity (RH) can be significantly altered by the presence of organics (Saxena et al., 1995; Saxena and Hildemann, 1997). However hygroscopic properties of aerosol have been attributed to only the inorganic fraction of the particles (Köhler, 1921; Meng and Seinfeld, 1995). The behavior of common salts, such as NaCl and $(NH_4)_2SO_4$ and their

combinations have been measured precisely (Tang et al., 1986; Tang and Munkelwitz, 1994). A series of thermodynamic models have been developed that use these experimental data and specific mixing rules to predict the properties of mixtures that have not been measured (Wexler and Seinfeld, 1991; Clegg et al., 1998).

Organic compounds are capable of dissolving into water and lowering surface tension of wet particles (Facchini et al., 2000). Both effects assist in CCN activation by decreasing the critical supersaturation needed for growing particles into droplets (Facchini et al., 1999). There are some laboratory and field measurements indicating that particles composed mainly of organic species are able to activate as CCN (Cruz and Pandis, 1997; Corrigan and Novakov, 1999; Russell et al., 2000). A recent calculation shows that soluble organic components increase CCN number concentrations by up to 13%, 97% and 110% for typical marine, rural and urban aerosols, respectively, as compared to aerosol composed completely by inorganic salts (Mircea et al., 2002).

Despite the important influences of organic compounds on the behavior of particles in the atmosphere, they have not been incorporated into computer models used to estimate phase equilibria of aerosol at different temperatures and relative humidities in the atmosphere (Wexler and Seinfeld, 1991). Modeling of organic aerosol is handicapped by two gaps in our current knowledge. First, the chemical composition of organic particulate matter is very complex and not well understood. Typically only 10% or less of the total organic mass in particles can be identified as individual compounds by field sampling and analysis (Rogge et al., 1993). Saxena and Hildemann (1996) examined the available solubility and vapor pressure data of organic compounds and concluded that compounds with between two (C2) and seven (C7) carbon atoms and more than one functional group (multifunctional) were among the

most likely water–soluble organic species in the atmosphere. Multifunctional organic compounds are also known to dominate in natural aerosol sources, such as sea salt particles (Ming and Russell, 2001). The second obstacle is the lack of thermodynamic models applicable to organic compounds of various structures and their mixtures. The available empirical models describing the organic solution are not able to represent multifunctional organic species accurately (Pividal and Sandler, 1990; Ansari and Pandis, 2000; Clegg et al, 2001).

One of the goals of our research is to develop an approach to calculating the phase equilibria of complex mixtures of organic species (including multifunctional compounds) with electrolytes in particles, using a generalized semi-empirical approach modified from the work of Li et al. (1994) in a self-consistent framework for calculating activity coefficients analogous to that described by Clegg et al. (2001).

For inorganic salts and a few organic species, careful measurements have been undertaken to predict the relative humidity at which water uptake is initiated (deliquescence) and the amount of water that particles of different compositions will accrete as the relative humidity continues to rise after this deliquescence point (Tang et al., 1986; Cruz and Pandis, 2000; Hämeri et al., 2000; Prenni et al., 2001). In all but one case (Hämeri et al., 2000), these studies have focussed on particles with initial dry diameters of 100 nm or greater. Measuring smaller particles has been precluded by experimental limitations on particle detection and trace contamination.

Physical descriptions of the deliquescence process have been provided by a series of standard texts for particles that are sufficiently large that the surface tension of the liquid/vapor interface is negligible (Defay et al., 1996; Adamson, 1996). More recently Mirabel et al. (2000) provided an idealized approach to the question of small particle deliquescence and addressed with an elegant model the predicted relative humidity

for prompt (or uncoated) deliquescence and its change with smaller particle sizes. In a similarly constrained physical system, we intend to show that the non–ideal aspects of the problem ultimately change the predicted behavior of the system such that our coated model predicts an inverse dependence of deliquescence relative humidity on particle size as opposed to the proportional dependence predicted by the idealized, uncoated deliquescence model.

Sea salt aerosol particles in the marine boundary layer (MBL) are produced from the evaporation of sea spray (Blanchard, 1983). Surface active organic materials in seawater can contribute to the aerosol phase as part of the bubble-bursting process (Hoffman and Duce, 1976). The resulting internally mixed aerosol of salt ions and organic species form a significant fraction of the aerosol particles in the marine boundary layer (Blanchard, 1964). These particles contribute to atmospheric radiative transfer indirectly by serving as cloud condensation nuclei and directly by scattering light in subsaturated conditions (Seinfeld and Pandis, 1997; Haywood et al., 1999).

The optical properties of aerosol particles are greatly influenced by their chemical composition as well as their size (Tang et al., 1997). Organic components will affect the particle refractive index and the size that a particle becomes by taking up water from the vapor phase in humid conditions. Water-soluble components of aerosol are more likely to take up water because the resulting aqueous solution will have a reduced water activity. Since both salts and organic components can be internally mixed in sea salt aerosol, particle hygroscopicity is determined by complex solutions of electrolytes, organic species, and water. The variety of chemical structures of organic compounds found in aerosol leads to a wide range of physical and chemical properties. This complexity poses difficulties for identifying particle components.

In addition to needing a model of the solution thermodynamics, an accurate description of the phase equilibrium of electrolyte-organic solutions requires knowing the composition of sea salt particles. Since only some sea salt components have been identified to date, we propose an estimated sea salt composition that incorporates all of the known organic and inorganic species in particles of different sizes. This model serves as a reference to study the sensitivity of hygroscopic growth to uncertainties in composition as well as in organic-water and organic-electrolyte interactions that control equilibrium. We use our thermodynamic model to calculate the hygroscopic growth of sea salt aerosol. In this way, we are allowed to compare the behavior of the model composition to field measurements of ambient aerosol.

Despite the potentially important influence of organic aerosol on CCN efficiency, there are currently few studies of kinetic simulation of fog/cloud formation that explicitly model organic aerosol as individual species and associated solvation and surface effects. This gap results from a poor understanding of chemical composition of organic aerosol (Rogge et al., 1993) and lack of thermodynamic approaches for calculating the properties of various organic compounds (Clegg et al., 2001). Fortunately, some latest progresses in both aspects offer us the opportunity to probe the roles that individual organic compounds in different types of aerosol play in kinetic CCN activation. Decesari et al. (2000) proposed a new approach to characterize water-soluble organic compounds (WSOC) with a combination of chromatographic separation, proton nuclear magnetic resonance (HNMR), and total organic carbon (TOC) analysis. This technique provides valuable information about the functional groups comprising organic aerosol, and hence polarity and solubility. Another advantage of this technique is that it is able to close the mass balance of WSOC within reasonable accuracy (Decesari et al., 2001). Based on the quantitative measurements of organic carbon

concentrations and HNMR-derived proton concentrations of main functional groups, seven model compounds commonly found in the atmosphere are chosen to represent the chemical composition of entire WSOC mass (Fuzzi et al., 2001. Our thermodynamic model treats organic compounds as combinations of functional groups so that the interaction parameters between groups correlated from available experimental data can be used to predict properties of unknown compounds. This approach can be utilized to calculate the thermodynamic properties (i.e. activity coefficient of water) of fog/cloud droplets containing both inorganic and organic species.

Fog forms as a result of the cooling of air near the Earth's surface due to radiation to space. Polluted fog events in densely populated areas are characteristic of high concentrations of particles and acidic gases (i.e. SO_2 and NO_2) and have serious detrimental effects on human health (Wyzga and Folinsbee, 1995). Studies on the chemical and microphysical processes in fog systems help to better understand the role of fog in producing (i.e. enhanced aqueous-phase oxidation of SO_2) and removing (i.e. wet deposition) particulate matter (PM) (Lillis et al., 1999). In our study, we use an aerosol dynamic model with detailed microphysical processes to simulate fog events in a polluted rural area (the Po Valley, Italy). The organic fraction of aerosol is explicitly represented by the compounds suggested by Fuzzi et al (2001).

Aerosol particles in clean marine environment differ from rural aerosols in several aspects. Due to the lack of anthropogenic sources, marine aerosols are less abundant than rural aerosols. The concentrations of marine aerosols are normally between 100 and 300 cm^{-3}, which are much lower than those of rural aerosols that could be as high as around 9000 cm^{-3}. In terms of chemical compositions, rural aerosols are composed mainly of NH_4NO_3 and $(NH_4)_2SO_4$, both of which originate from industrial pollution (NO_2, SO_2 and NH_3). They jointly account for around 80% of rural aerosol mass

(Decesari et al., 2001). Though a large number of fine particles consist of $(NH_4)_2SO_4$ produced from the oxidization of Dimethyl Sulfide (DMS), marine aerosol mass is dominated by sea salt aerosol generated from evaporating sea sprays. In our study, we simulate the evolution of chemical compositions and size distributions of marine aerosols and the formation of marine clouds in clean environment.

From a perspective of climate policy, there is a need to include the climate and health effects of sulfate aerosol into integrated-assessment models in order to formulate appropriate policies. Our research extends to the policy arena to study the influences of different climate policies on future temperature trend. The approach we use is to optimize investment rate given the costs incurred by global warming due to GHGs (and mitigated by the cooling effect of aerosol) and by the detrimental effects of sulfate aerosol on human health.

Chapter 2

Thermodynamic Equilibrium of Organic–Electrolyte Mixtures

2.1 Phase Equilibrium

The Gibbs free energy (G) of a particle with coexisting liquid and solid phases suspended in a vapor is expressed as:

$$G = \mu_S n_S + \mu_L n_L + \mu_V n_V + \sigma^{LV} a^{LV} + \sigma^{SL} a^{SL} \tag{2.1}$$

where the subscripts S, L and V refer to the solid, liquid and vapor phases (assuming only one phase of each type), respectively. μ is the chemical potential, and n is the number of moles of each phase. σ^{LV} and σ^{SL} are the interfacial tensions on the surface areas a^{LV} between liquid and vapor phases and a^{SL} between solid and liquid phases, respectively (Mirabel et al., 2000).

The phase equilibrium system of aerosol is composed of one vapor phase V, liquid phases with index l and solid phases with index s coexisting. Based on Eq. 2.1, the total Gibbs free energy of the system (G) for a particle with multiple ionic species i, organic species o, and water partitioned into one or more liquid phases l or solid

phases s is

$$\begin{aligned} G &= \sum_s \left(\sum_i n_i^s \mu_i^s + \sum_o n_o^s \mu_o^s \right) \\ &+ \sum_l \left(\sum_i n_i^l \mu_i^l + \sum_o n_o^l \mu_o^l + n_w^l \mu_w^l \right) + n_w^V \mu_w^V \\ &+ \sum_l \sigma^{lV} a^{lV} + \sum_l \sum_s \sigma^{sl} a^{sl} \end{aligned} \tag{2.2}$$

The contributions to the total Gibbs free energy are from both the chemical potential of species present in all phases and from the interfacial energy caused by the interfacial tension σ over the interfacial area a between these phases.

Before mixing, the initial state for water is vapor as quantified by relative humidity RH, whereas the initial states for organic and ionic species are their respective pure solids. Thus, the total initial Gibbs free energy G^o that describes each of the species in its unmixed state is expressed as

$$\begin{aligned} G^o &= \sum_s \left(\sum_i n_i^s \mu_i + \sum_o n_o^s \mu_o \right) \\ &+ \sum_l \left(\sum_i n_i^l \mu_i + \sum_o n_o^l \mu_o + n_w^l \mu_w^V \right) \\ &+ n_w^V \mu_w^V \end{aligned} \tag{2.3}$$

where μ_o and μ_i are the chemical potentials of organic and inorganic species at their respective pure solid states.

Noting that

$$\mu_o = \mu_o^s \tag{2.4}$$

$$\mu_i = \mu_i^s \tag{2.5}$$

if the unmixed solid states are pure solid phases, the change in Gibbs free energy due to mixing ΔG is given by

$$\Delta G \equiv G - G^o$$

$$
\begin{aligned}
&= \sum_l \left(\sum_i (\mu_i^l - \mu_i) n_i^l + \sum_o (\mu_o^l - \mu_o) n_o^l + (\mu_w^l - \mu_w^V) n_w^l \right) \\
&+ \sum_l \sigma^{lV} a^{lV} + \sum_l \sum_s \sigma^{sl} a^{sl} \qquad (2.6)
\end{aligned}
$$

The chemical potentials can be written in terms of their reference state chemical potentials (μ_i^o, μ_o^o, μ_w^o) and their activities as follows:

(i) inorganic ions:

$$\mu_i^l = \mu_i^o + RT \ln(x_i^l \gamma_i^l) \qquad (2.7)$$

$$\mu_i^s = \mu_i^o + RT \ln(\bar{x}_i^l \bar{\gamma}_i^l) \qquad (2.8)$$

(ii) organic species:

$$\mu_o^l = \mu_o^o + RT \ln(x_o^l \gamma_o^l) \qquad (2.9)$$

$$\mu_o^s = \mu_o^o + RT \ln(\bar{x}_o^l \bar{\gamma}_o^l) \qquad (2.10)$$

(iii) water:

$$\mu_w^l = \mu_w^o + RT \ln(x_w^l \gamma_w^l) \qquad (2.11)$$

$$\mu_w^V = \mu_w^o + RT \ln\left(\frac{RH}{100}\right) \qquad (2.12)$$

where x and γ are the mole fraction and activity coefficient, respectively. $\bar{x}$ and $\bar{\gamma}$ refer to the mole fraction and activity coefficient at the solubility limit of the pure solid. By substituting Eq. 2.7–2.12 into Eq. 2.6, the chemical potentials at their respective reference states are cancelled so that the Gibbs free energy change ΔG simplifies to

$$
\begin{aligned}
\Delta G &\equiv G - G^o \\
&= RT \sum_l \sum_i \ln\left(\frac{x_i^l \gamma_i^l}{\bar{x}_i^l \bar{\gamma}_i^l}\right) n_i^l + RT \sum_l \sum_o \ln\left(\frac{x_o^l \gamma_o^l}{\bar{x}_o^l \bar{\gamma}_o^l}\right) n_o^l \\
&+ RT \sum_l \ln\left(\frac{x_w^l \gamma_w^l}{\frac{RH}{100}}\right) n_w^l \\
&+ \sum_l \sigma^{lV} a^{lV} + \sum_l \sum_s \sigma^{sl} a^{sl} \qquad (2.13)
\end{aligned}
$$

The distribution of species among phases at chemical equilibrium is determined by minimizing the Gibbs free energy change ΔG. In our work, the total amount of each non–water component in the equilibrium system is fixed in order to compare results with a constant dry mass basis. At a specific relative humidity, the amount of water in the liquid phases is allowed to vary to achieve the configuration of lowest Gibbs free energy. In searching for the optimal water content, the number of solution phases and the amounts of each component in each phase are also allowed to vary to find the lowest Gibbs free energy change. The compounds with similar polarities have a tendency to form a homogeneous solution, while different polarities cause species to separate from each other due to the nonideality of resulting solutions (Saxena and Hildemann, 1996).

Noting that

$$\bar{x}_k^l \bar{\gamma}_k^l = \frac{f_k^L}{f_k^S} \tag{2.14}$$

where f_k^l is the pure liquid fugacity and f_k^s is the pure solid fugacity, and that the equilibrium constant at solubility limit K_i^{eq} can be rewritten as $\bar{x}_k^l \bar{\gamma}_k^l = K_i^{eq}$ for electrolytes, we can rewrite Eq. 2.13 as

$$\begin{aligned}
\Delta G &\equiv G - G^o \\
&= RT \sum_l \sum_i \ln\left(\frac{x_i^l \gamma_i^l}{K_i^{eq}}\right) n_i^l + RT \sum_l \sum_o \ln\left(\frac{x_o^l \gamma_o^l}{\frac{f_o^L}{f_o^S}}\right) n_o^l \\
&+ RT \sum_l \ln\left(\frac{x_w^l \gamma_w^l}{\frac{RH}{100}}\right) n_w^l \\
&+ \sum_l \sigma^{lV} a^{lV} + \sum_l \sum_s \sigma^{sl} a^{sl}
\end{aligned} \tag{2.15}$$

The values of K_i^{eq} for various salts are compiled in Clegg et al. (1998). The approach to calculating the fugacity ratio of organic compounds is based on an empirical model of organic properties described in the next section.

The activity coefficient γ_i^l of component i in solution l is a function of the chemical composition represented by $x_n^l,\ n = 1, 2, ..., N$ (N is the number of species present). In order to evaluate the Gibbs free energy change ΔG as shown by Eq. 2.15, we need to describe the activity coefficients as functions of the composition. This model of solution activity, coupled with a composition–dependent parameterization of surface tension, allows us to search for the minimum Gibbs free energy at a specified composition and thus to identify the equilibrium phase partitioning of the system.

Solution Activity While cloud droplets are frequently sufficiently dilute to allow us to assume that solute activities are linearly dependent on mole fractions, subsaturated particles at relative humidities between 35% and 95% frequently behave nonideally. In such nonideal solutions the chemical potentials of components vary both with their own mole fraction and with the overall composition. In general, two types of both electrolyte and organic solution models have been developed for a variety of applications.

Zhang et al. (2000) summarized existing models of aqueous solutions of electrolytes including the Zdanovski–Stokes–Robinson (ZSR) and Pitzer approaches. One such model is the Pitzer-Simonson-Clegg model, based on the concept of ion interaction in which interactions between ions are used to describe the solution nonideality (Clegg et al., 1992).

Unlike electrolytes, organic species have diverse chemical structures and possess quite different properties, both from each other and from electrolytes. The concept of Group Contribution Methods (GCM) utilizes functional groups, instead of molecules, as the interacting entities in order to reduce to about 20 groups the number of parameters needed to describe hundreds of organic species (Fredenslund et al., 1977). UNIFAC (UNIQUAC Functional Group Activity Coefficients Model, where

UNIQUAC stands for Universal Quasi-Chemical) uses a GCM-based approach and has been shown to be effective in predicting the properties of mixtures in various applications (Gmehling, 1995). The phase equilibrium model for internal mixtures of organics and electrolytes that we have developed is based on the Pitzer-Simonson-Clegg approach to electrolytes and the UNIFAC approach to organic species. Since pure organic and pure electrolyte solutions are limiting cases of the general model, the accuracy of mixture predictions is expected to be comparable to existing models (Clegg et al., 2001).

Three different types of components are present in the solution. They are inorganic ions (electrolytes), organic compounds, and water. The activity coefficient of each component varies with particle composition, namely the mole fraction x_m of a species m, where

$$x_m = \frac{n_m}{n_w + \sum_o n_o + \sum_i n_i} \tag{2.16}$$

The subscripts w, o, and i of mole number n represent water, organic compound, and ion, respectively. The summations are over all organics and ions present in the system. The binary interactions involved in the general model are ion–water (IW) and organic–water/organic–ion (OW/OI), where here we use "ion" to refer only to inorganic ions (Kikic et al.,, 1991). The activity coefficient of each component γ_m includes contributions from these two types of interactions, as described by

$$\ln \gamma_m = \ln \gamma_m^{IW} + \ln \gamma_m^{OW/OI} \tag{2.17}$$

where independent interactions are assumed to have additive contributions (Li et al., 1994). The ion–water interactions are calculated as in previously proposed models (Clegg et al., 1992; Wexler and Seinfeld, 1991). Organic–water and organic–ion interactions are described with a UNIFAC–based approach using measurements of

"salting–out" constants for different ions (Kikic et al., 1991; Yan et al., 1999; Sutton and Calder, 1974). Recent work has also calculated properties for specific binary (single inorganic ion–single organic species–water) mixtures for which detailed data are available (Clegg et al., 2001). In this work, we use a general approach to quantify electrolyte–organic interactions in aqueous solutions that accurately represents the range of species commonly found in atmospheric particles. The following sections describe the algorithms that underly these three different types of molecular interactions in order to calculate the phase equilibrium.

Ion–Water Interactions The Pitzer-Simonson-Clegg model is used to calculate the ion–water contribution γ_m^{IW} in Eq. 2.17 to the overall activity coefficient γ_m (Clegg et al., 1992). The interactions between ions and water molecules are considered to be independent of the organic species existing in solution (all corrections for interactions with organic species are included in $\gamma_m^{OW/OI}$). The inorganic mole fraction $x_m^\star$ appropriate in this context is the number of moles of ions normalized by the total number of non–organic constituents, namely

$$x_m^\star = \frac{n_m}{n_w + \sum_i n_i} \tag{2.18}$$

where m refers to either a water molecule or an ion (Clegg et al., 2001). The electrolyte–water contribution to activity coefficient γ_m^{IW} is the combination of long–range (LR) and short–range (SR) effects:

$$\ln \gamma_m^{IW} = \ln \gamma_m^{LR} + \ln \gamma_m^{SR} \tag{2.19}$$

where the specific expressions for γ_m^{LR} and γ_m^{SR} are given by Eq. 24–26 and Eq. 15–17 of Clegg et al. (1992). Short–range interactions dominate in concentrated solutions and long–range in dilute solutions.

A complete parameter set for experimental data for Na^+, NH_4^+, H^+, Cl^-, SO_4^{2-} and HSO_4^- is available from Clegg et al. (1998). Two additional ions of interest in marine air (Mg^{2+} and Ca^{2+}) have been added using parameters in Clegg et al. (1992). The missing binary and ternary interaction parameters were set to zero. The model predictions agreed with existing mixture data for systems composed of Na^+–Mg^{2+}–Cl^-–H_20, Na^+–Mg^{2+}–SO_4^{2-}–H_20, Na^+–Cl^-–SO_4^{2-}–H_20, and Ca^{2+}–Mg^{2+}–Cl^-–H_20 within 1% (Clegg et al., 1992). Since Mg^{2+} and Ca^{2+} account for small fractions of inorganic mass in seawater (Mg^{2+} 3.7%, Ca^{2+} 1.1%) (Riley and Chester, 1971), the error introduced by setting missing parameters to zero is negligible for sea salt aerosol. For other types of aerosol, in which Mg^{2+} and Ca^{2+} and other ions that we have omitted (such as NO_3^-) are more prevalent, more detailed laboratory results on the interactions of these ions are needed. The accuracy of the inorganic ion interactions with water is illustrated in Fig. 2.1.

The activity coefficients $\gamma_m^{LR\star}$ and $\gamma_m^{SR\star}$ are translated from the inorganic–only mole fraction ($x_m^\star$) to the solution mole fraction (x_m) in order to obtain γ_m^{LR} and γ_m^{SR} using the following relationship:

$$\ln \gamma_m^{LR} = \ln \gamma_m^{LR\star} - \ln\left(1 - \sum_o x_o\right) \tag{2.20}$$

$$\ln \gamma_m^{SR} = \ln \gamma_m^{SR\star} - \ln\left(1 - \sum_o x_o\right) \tag{2.21}$$

These activity coefficients can then be used to calculate γ_m^{IW} with Eq. 2.19.

Organic–Water and Organic–Ion Interactions

In the original UNIFAC model (Fredenslund et al., 1975), the contribution to the activity coefficient of each component m in solution comes from two sources: the

Figure 2.1: Comparison of correlated solubilities of salts in four ternary ion solutions with measurements: (a): NaCl (open circle) in Na–Mg–Cl–H_2O solution; (b): $Na_2SO_4 \cdot 10H_2O$ (open circle), $Na_2Mg(SO_4)_2 \cdot 4H_2O$ (open square), and $MgSO_4$ (open triangle) in Na–Mg–SO_4–H_2O solution; (c): $Na_2 \cdot 10H_2O$ (open circle), Na_2SO_4 (open square), and NaCl (open triangle) in Na–Cl–SO_4–H_2O solution; (d): $MgCl_2 \cdot 6H_2O$ (open circle), $Mg_2CaCl_6 \cdot 12H_2O$ (open square), and $CaCl_2 \cdot 6H_2O$ (open triangle) in Mg–Ca–Cl–H_2O solution. Experimental data are compiled in Silcock (1979).

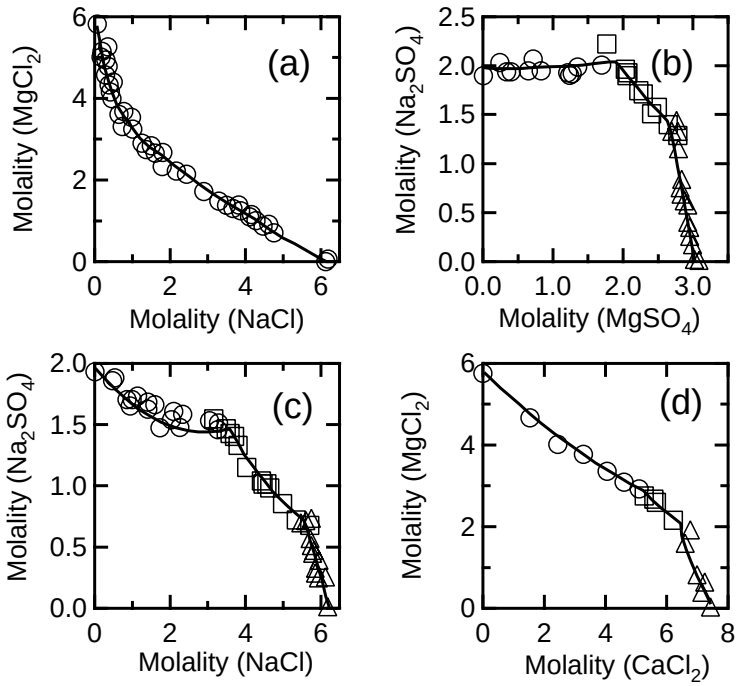

combinatorial part (γ_m^C) and the residual part (γ_m^R):

$$\ln \gamma_m^{OW/OI} = \ln \gamma_m^C + \ln \gamma_m^R \tag{2.22}$$

Here m refers to organic compounds, inorganic compounds, or water. The expressions for $\ln \gamma_m^C$ and $\ln \gamma_m^R$ were given by Eq. 2 to Eq. 9 of Fredenslund et al. (1975).

Limitations of UNIFAC models preclude their use for predicting aerosol properties (Saxena and Hildemann, 1997; Ansari and Pandis, 2000). The original purpose of UNIFAC was to assist the design of chemical separation processes (Ghmeling, 1995). For these applications the compounds of most interest are small monofunctional compounds with solution systems that are usually highly concentrated. However, common organic species in atmospheric particles include both long–chain monofunctional and short–chain multifunctional compounds (Saxena and Hildemann, 1997). Water can account for a large fraction of aerosol mass, making the solution both dilute and polar. This mismatch of mixture type in traditional UNIFAC models means that existing correlation parameters will not accurately describe aerosol phase equilibrium for the complex solutions found in the atmosphere. In addition to correlating data with appropriate measurement data sets, the model accuracy can be improved by defining more specific types of functional groups that use different compounds for correlation.

The proximity of two or more polar functional groups in the same multifunctional compounds make the assumption of independent groups inappropriate (Pividal and Sandler, 1990). Wu and Sandler (1989; 1991) provided proof for the strong interaction between polar groups within a molecule from *ab initio* molecular orbital calculations. To improve the prediction of the behavior of multifunctional organics, new "meta–groups" for different combinations of groups were correlated from available experimental data (Wu and Sandler, 1991). For example, to account for the effects of multiple functional groups in one molecule, we define meta–groups consisting of pairs

of functional groups as shown in Table 2.1 (for example, –COOH in hydroxy–acids, –OH in monosaccharides, and –COOH in diacids). In addition, multiple types of alkyl groups, CH_n ($n = 0, 1, 2, 3$) can be used to represent the carbons in short–chain and long–chain alkanes, as well as in monosaccharides, hydroxy–acids and diacids. This expanded set of groups and their correlated interaction parameters are listed in Table 2.1.

For monofunctional compounds, most existing UNIFAC parameter sets are correlated from short–chain species with carbon numbers less than 5. These parameters cannot be used successfully to represent the infinite dilution activity coefficients (IDAC) of long–chain insoluble compounds (Zhang et al., 1998). Most nonpolar organic species measured in marine and polluted aerosol are long–chain alkanes, alkanols and carboxylic acids (Gagosian et al., 1981; Gogou et al, 1998). Zhang et al. (1998) showed that existing UNIFAC models predict infinite dilution activity coefficients of long–chain monofunctional compounds with mean relative deviations from measured values of 45% to 72%.

Dissolved electrolytes can interact with organic components in solution. The solubilities of most organic compounds are lowered with increasing salt concentrations (known as the "salting–out effect"), although some species become more soluble due to the presence of salts (known as the"salting–in" effect) (Long and McDevit, 1952). Despite the relatively small number of electrolytes, the variety of organic species and their different properties make the electrolyte–organic interaction quite complicated. We can consider this type of interaction by treating ions as groups in UNIFAC. Since the interaction between ions and water is assessed by γ_m^{IW} from the Pitzer-Simonson-Clegg model, no additional interactions for water and ions are included here. Therefore, the activity coefficients of water and ions predicted by this extended

Table 2.1: Group interaction parameters used in this model. Parameters marked with an asterisk were correlated in this work; all other parameters were correlated by Gmehling et al. (1982).

	Na^+	NH_4^+	Cl	SO_4^{2}	-CH_n[a]	-OH	-COOH[c]	-CH_nCO-[d]	-CH_n[e]	-CH_nO	-OH	-CH_n	-COOH[i]	-OH	-CH_n	-COOH[l]	H_2O
Na^+	0	0	0	0	7794	6654	6654	6654	376	203	147	2292	1958	1849	2532	132	0
NH_4^+	0	0	0	0	7794	6654	6654	6654	376	203	147	2292	1958	1849	2532	132	0
Cl	0	0	0	0	8093	53760	53760	53760	719	638	366	2623	2289	2180	2864	132	0
SO_4^{2}	0	0	0	0	8093	53760	53760	53760	719	638	366	2623	2289	2180	2864	132	0
-CH_n[a]	7771	7771	8107	8107	0	986.5	663.5	476.4	0	251.5	986.5	0	663.5	986.5	0	663.5	1318
-OH	5768	5768	7032	7032	156.4	0	199	84	156.4	28.06	0	156.4	199	0	156.4	199	1000
-COOH[c]	5768	5768	7032	7032	315.3	-151	0	-297.8	315.3	-338.5	-151	315.3	0	-151	315.3	0	1000
-CH_nCO-[d]	5768	5768	7032	7032	26.76	164.5	669.4	0	26.76	5.202	164.5	26.76	669.4	164.5	26.76	669.4	1000
-CH_n[e]	636	636	1027	1027	0	986.5	663.5	476.4	0	251.5	986.5	0	663.5	986.5	0	663.5	1318
-CH_nO	-640	-640	-720	-720	83.36	237.7	664.6	52.38	83.36	0	237.7	83.36	664.6	237.7	83.36	664.6	2007
-OH	184	184	488	488	156.4	0	199	84	156.4	28.06	0	156.4	199	0	156.4	199	-189.7
-CH_n	1008	1008	1491	1491	0	986.5	663.5	476.4	0	251.5	986.5	0	663.5	986.5	0	663.5	1318
-COOH[i]	-23.3	-23.3	-123.1	-123.1	315.3	-151	0	-297.8	315.3	-338.5	-151	315.3	0	-151	315.3	0	-163.3
-OH	208.8	208.8	781.6	781.6	156.4	0	199	84	156.4	28.06	0	156.4	199	0	156.4	199	-92.3
-CH_n	1231	1231	1593	1593	0	986.5	663.5	476.4	0	251.5	986.5	0	663.5	986.5	0	663.5	4694
-COOH[l]	-324	-324	2134	2134	315.3	-151	0	-297.8	315.3	-338.5	-151	315.3	0	-151	315.3	0	-186.3
H_2O	0	0	0	0	541.3	-959	-530	-471	300	193.1	171.3	300	64.6	224.4	304	86	0

Experimental data were not available; parameters of Na^+ have been substituted.

Experimental data were not available; parameters of Cl have been substituted.

[a] -CH_n (n=0,1,2,3) in long–chain monofunctional compounds

-OH in long–chain monofunctional compounds

[c] -COOH in long–chain monofunctional compounds

[d] -CH_nCO (n=2,3) in long–chain monofunctional compounds

[e] -CH_n (n=0,1,2,3) in monosaccharides

-CH_nO (n=0,1,2) in monosaccharides

-OH in monosaccharides

-CH_n (n=0,1,2,3) in hydroxy-acids

[i] -COOH in hydroxy-acids

-OH in hydroxy-acids

-CH_n (n=0,1,2,3) in diacids

[l] -COOH in diacids

UNIFAC approach should reduce to unity for aqueous solutions of pure electrolytes. This constraint requires setting the interaction parameters describing ionic groups and water ($\alpha_{i,w}$ and $\alpha_{w,i}$ in Eq. 9 of Fredenslund et al. (1975)) to zero as indicated in Table 2.1. The volume and area parameters R_i and Q_i of ionic group i in Eq. 4 of Fredenslund et al. (1975) are arbitrarily set equal to those for water so that the combinatorial part of the UNIFAC equations will be zero in the absence of organics. This assumption is tested in the discussion on model sensitivity.

Surface Tension Algorithm Since the contribution of interfacial energy to the total Gibbs free energy of the multiphase equilibrium in Eq. 2.1 is always positive, it increases the Gibbs free energy relative to the bulk case without interfacial tension. As a result, higher relative humidities are required for smaller particles to reach equilibrium with a specified solution.

The surface tension of the solution is determined by its chemical composition. Organic species lower the surface tension of aqueous solutions to below that of pure water (Li et al, 1999). Aqueous solutions of electrolytes have higher surface tensions than pure water (Nath, 1999). In this work, both types of solutes coexist in the solution and affect the surface tension. To calculate the surface tension from the chemical composition of an electrolyte–organic aqueous solution, the solution phase is divided into a surface phase and a bulk phase. The surface phase is a thin layer immediately adjacent to the vapor phase and serves as a boundary to separate the bulk solution phase from the vapor phase. All species present in the solution are distributed between the surface and bulk phases, and the composition of the bulk phase is the same as the overall chemical composition of solution, since the mass of the surface phase is negligibly small.

The chemical composition of the surface phase is independent of the overall composition and can be determined from measured mixture properties. The chemical potential μ_m^B of component m (which may be either water or an organic species) in the bulk phase (B) is represented as:

$$\mu_m^B = \mu_m^{B,o} + RT \ln(x_m^B \gamma_m^B) \tag{2.23}$$

where $\mu_m^{B,o}$ is the chemical potential at the reference state of m in the bulk phase. x_m^B and γ_m^B are the mole fraction and activity coefficient of m in the bulk phase. The chemical potential μ_m^S of component m in the surface layer is given by:

$$\mu_m^S = \mu_m^{S,o} + RT \ln(x_m^S \gamma_m^S) - \overline{A}_m \sigma \tag{2.24}$$

where $\mu_m^{S,o}$ is the chemical potential at the reference state of m in the surface phase. x_m^S and γ_m^S are the mole fraction and activity coefficient of m in the surface phase. $\overline{A}_m$ is the partial molar area of m in solution and σ is the surface tension of solution. The reference states of organic components and water are their respective pure liquid phases. The chemical potentials at the reference states in the bulk and surface phase are related by:

$$\mu_m^{B,o} + A_m \sigma_m = \mu_m^{S,o} \tag{2.25}$$

where σ_m is the surface tension of m in pure liquid phase and A_m is the corresponding molar area.

In order to reach equilibrium between the surface and bulk phases, the chemical potentials of each species in the bulk and surface phases should be equal to each other, namely

$$\mu_m^B = \mu_m^S \tag{2.26}$$

Substituting Eq. 2.23, 2.24 and 2.25 in 2.26 and noting that the partial molar area

$\overline{A}_m$ can be approximated as the molar area A_m (Li et al., 1999), we find

$$\sigma = \sigma_m + \frac{RT}{A_m} \ln \frac{x_m^S \gamma_m^S}{x_m^B \gamma_m^B} \tag{2.27}$$

For electrolytes, the concentrations of ions in the surface phase are assumed to be proportional to those in the bulk phase.

$$x_{i,S} = k_i x_{i,B} \tag{2.28}$$

where k_i is correlated from the measurements of surface tension for each species (Li et al., 1999). Laaksonen (1993) calculated the interior concentration of aerosol particles created by dispersion of surfactant solutions depending on the overall concentration (the concentration of bulk solution from which aerosol is generated) and particle size by solving Gibbs-Duhem equation. To assess the impact of our assumption of constant concentration, we allowed the concentration to vary in the particle for two cases, $(NH_4)_2SO_4$ and glutaric acid solutions. For a 100 nm dry particle of $(NH_4)_2SO_4$, the solute increases the surface tension of the solution, the gradient in concentration between the interior and overall compositions increases the growth by 2%. Since glutaric acid lowers the surface tension of the solution, the hygroscopic growth decreases by 3%.

2.2 Empirical Correlations

Thermodynamic data collected from published measurements were used to fit the interaction parameters described above. The different types of data are summarized below:

(1) **Infinite dilution activity coefficient**

Figure 2.2: Comparison of correlated infinite dilution activity coefficients (γ^{∞}) with measurements of four types of long–chain monofunctional compounds: (a) alkane, (b) alcohol, (c) acid and (d) ketone. The measurements (crosses) are compiled in Kojima et al. (1997). Correlations are from this work (solid line) along with predictions from the original UNIFAC (Fredenslund et al., 1977; thin dashed line), VLE–UNIFAC(Skjold–Jørgensen et al., 1979; thin dotted line), LLE–UNIFAC(Magnussen et al., 1981; thin dashed–dotted line) and IDAC–UNIFAC (Bastos et al., 1988; dashed line).

The infinite dilution activity coefficient (IDAC) is the limit of the activity coefficient of a solute in water when the concentration of the solute is infinitely small. In this situation, a single solute molecule is completely surrounded by water molecules. Therefore, the IDAC largely reflects the interaction between solute and water in the absence of other solutes. Kojima et al. (1997) described an accurate method for measuring IDAC and collected a comprehensive database of available measurements for a variety of compounds. Comparisons to these data are shown in Fig. 2.2.

(2) **Solubility and activity coefficient at saturation**

At the solubility limit, the solute reaches chemical equilibrium with its pure state. For organic compound o existing as solid in pure state, the activity at saturation is equal to the corresponding ratio of liquid-solid reference fugacities $\frac{f_o^L}{f_o^S}$.

$$x_o^{sat}\gamma_o^{sat} = \frac{f_o^L}{f_o^S} \tag{2.29}$$

The mole fraction at the solubility limit and the activity coefficient at saturation are denoted by x_o^{sat} and γ_o^{sat}, respectively. The fugacity ratio is a quantitative measurement of energy used to melt organic solid o (Peters et al., 2000). From the enthalpy of melting ΔH_m and melting temperature T_m, the fugacity ratio

at temperature T can be calculated as

$$\ln \frac{f_o^L}{f_o^S} = \frac{\Delta H_m}{RT_m}\left(\frac{T_m}{T} - 1\right) \tag{2.30}$$

where R is the universal gas constant. If the fugacity ratio of an organic compound is known, the activity coefficient at saturation can be calculated from the measured solubility according to Eq. 2.29.

(3) **Salting–out constant**

The impact of dissolved electrolytes on the solubility of organic compounds was described by the Setchenow equation as

$$\log\left(\frac{C_o}{C_{o,s}}\right) = k_s C_s \tag{2.31}$$

where C_o and $C_{o,s}$ are the solubility of organic compound o (mol L^{-1}) in pure water and in aqueous salt solution, respectively. C_s is the corresponding salt concentration (mol L^{-1}) (Sutton and Calder, 1974). The empirical "salting–out" constant k_s is correlated from experimental data (Long and McDevit, 1952). Eq. 2.31 assumes the organic concentration is low, in which case it can be rewritten in terms of mole fractions of organic compounds in water (x_o) and of organic compounds in salt solution ($x_{o,s}$):

$$\log\left(\frac{x_o}{x_{o,s}}\right) = \log\left(\frac{\gamma_{o,s}}{\gamma_o}\right) = k_s C_s \tag{2.32}$$

where γ_o and $\gamma_{o,s}$ are the activity coefficient at saturation in pure water and in aqueous salt solution, respectively. At high organic concentrations, Eq. 2.31 is inaccurate. The ion–organic interaction parameters derived from these parameters are summarized in Table 2.1.

Using these types of thermodynamic data, the least–square approach was used to estimate the model parameters from experimental data. The objective function

$$F(\tau) = \min \sum_{j} \sum_{(k)} (X_{j(k)} - \widehat{X}_{j(k)})^2 \tag{2.33}$$

for any data type j, for example β_{io}, is used to minimize the difference between the measured data $X_{j(k)}$ and the fitted parameterization $\widehat{X}_{j(k)}$ for the kth measured and calculated data points, respectively. τ is the optimal parameter vector (Magnussen et al., 1981). The software package MINPACK that implements the Levenberg–Marquardt algorithm was employed to minimize the objective function and fit the model parameters (More et al., 1980). The resulting parameter set is included in Table 2.1. The available experimental data of aqueous solution of organic species were used to correlate the interaction parameters between organic groups and water and between organic and ionic groups from measurements using the datasets summarized in Table 2.2. For each type of correlation, Table 2.2 lists the data set used, the parameters derived, and the precision of the fit to the data. The following sections describe each of these fits and illustrate them graphically.

Long–chain monofunctional compounds Most well developed UNIFAC models were based on experimental data of short–chain (less than 5 carbons) monofunctional compounds (Fredenslund et al., 1977; Skjold-Jørgensen et al., 1979; Magnussen et al., 1981). Zhang et al. (1998) reported that the available UNIFAC parameter sets cannot be reliably utilized to predict the infinite dilution activity coefficients of long–chain monofunctional compounds. The new groups listed in Table 2.1 are used to represent methyl (CH_n), hydroxyl (–OH), carboxylic acid (–COOH) and carboxyl (–$COCH_n$) in long–chain monofunctional compounds. The model correlations together with those from other UNIFAC models are compared with measured infinite dilution activity coefficients (IDACs) of alkane, alcohol, acid and ketone collected by Kojima

Table 2.2: Summary on experimental data used in fitting model parameters. The sequence of correlations is the same as the order in which they are listed in this table.

Solution System	Data Type	Concentration Range	Reference	Percentage Error	UNIFAC Parameters Correlated
Alkane-water (C5-C12) Alcohol-water (C4-C18) Acid-water (C4-C13) Ketone-water (C4-C7)	Activity coecien ts of organic compounds	Innite dilution	Kojima et al. (1997)	8%	Between long-chain monofunctional organic compound (-CH $_n$, -OH, -COOH and -CH $_n$CO-) and water
Alkane (C12, C14, C16, C18)-NaCl-water	Activity coecien ts of alkane	NaCl (0-5.3 mol L ^{1})	Sutton and Calder (1974)	7%	Between -CH $_n$ in long-chain monofunctional compounds and ionic groups (Na $^+$ and Cl)
Hexanol-NaCl-water	Activity coecien ts at solubility of hexanol	NaCl (0-5.3 mol L ^{1})	Zdenek et al. (1980)	3%	Between -OH in long-chain monofunctional compounds and ionic groups (Na $^+$ and Cl)
Glucose-water Fructose-water	Relative humidity	Glucose (0-4 mol L ^{1}) Fructose (0-6.3 mol L ^{1})	Peres and Macedo (1996)	3%	Between groups in monosaccharides (-CH$_n$, -CH$_n$O and -OH) and water
Glucose-NaCl-water Fructose-NaCl-water	Relative humidity	Glucose, Fructose (0-3.0 mol L ^{1}) NaCl (0-3.5 mol L ^{1})	Comesana et al. (1999)	0.1%	Between groups in monosaccharide (-CH $_n$, -CH$_n$O and -OH) and ionic groups (Na $^+$ and Cl)
Malic acid-water Tartaricacid-water Citric acid-water	Relative humidity	Malic acid (0-4.4 mol L ^{1}) Tartaricacid (0-4.2 mol L ^{1}) Citric acid (0-2.8 mol L ^{1})	Velezmoro and Meirelles (1998)	2%	Between groups in hydroxy-acids (CH$_n$, -COOH and -OH) and water
Tartaricacid-NaCl-water	Activity coecien ts at saturation of tartaricacid	NaCl (0-5.3 mol L ^{1})	Herz and Hiebenthal (1929)	53%	Between groups in hydroxy-acids (CH $_n$, -COOH and -OH) and ionic groups (Na $^+$ and Cl)
Diacid (C4-C13)-water	Activity coecien ts at solubility of diacids	Diacids (0-solubility)	Acree (1991) Freier (1976)	20%	Between groups in diacids (-CH $_n$ and -COOH) and water
Succinic acid-NaCl-water	Solubility of succinic acid	NaCl (0-5.3 mol L ^{1})	Herz (1909)	1%	Between groups in diacids (-CH $_n$ and -COOH) and ionic groups (Na $^+$ and Cl)

et al. (1997) in Fig. 2.2. In general, the compounds tend to have higher IDACs with increasing carbon numbers as indicated by UNIFAC–based models (Zhang et al., 1998). However, our results agree well with the data, giving values within 8% of measured data for all four types of compounds. The IDACs of isomers that have the same carbon number but different chemical structures depend on the specific configurations of carbon chains, but cannot be predicted with the UNIFAC approach (Fredenslund et al., 1977).

The "salting–out" constants of NaCl with four long–chain alkanes including dodecane (C12), tetradecane (C14), hexadecane (C16) and octadecane (C18) were reported by Sutton and Calder (1974). Their activity coefficients at saturation for different concentrations of NaCl were calculated according to Eq. 2.29. From these data, the interaction parameters between ionic groups (Na^+ and Cl^-) and long–chain CH_n were fitted. The results are plotted in Fig. 2.3. The "salting–out" effect causes the activity coefficients of organic solutes to increase with higher concentrations of NaCl. Consequently the compounds become less soluble with increasing salt concentration. At saturation for NaCl (ca. 5.3 mol L^{-1}), the activity coefficients of four alkanes are normally 10 to 100 times larger than those in the absence of salt. The fitted correlations to measurements represent the general trend of the "salting–out" effect satisfactorily over much of the concentration range of NaCl, while deviations from experimental data are significant at the high concentration end. These errors are up to 30% in mixtures of alkanes with high NaCl concentrations (5.3 mol L^{-1}), but the model agrees with the empirical parameterization within 10% at NaCl concentrations less than 2.0 mol L^{-1}.

The "salting–out" constant of hexanol provided data for the dependence of activity coefficients of hexanol on NaCl concentration (Zdenek et al., 1980). The interaction

Figure 2.3: Comparison of correlated activity coefficients at saturation in NaCl aqueous solution with parameterized experimental measurements of four long–chain alkanes that are (a) dodecane (C12), (b) tetradecane (C14), (c) hexadecane (C16), (d) octadecane (C18). The correlation and empirical parameterization are represented by solid and dashed lines, respectively, in each panel. The empirical parameterization is taken from Sutton and Calder (1974).

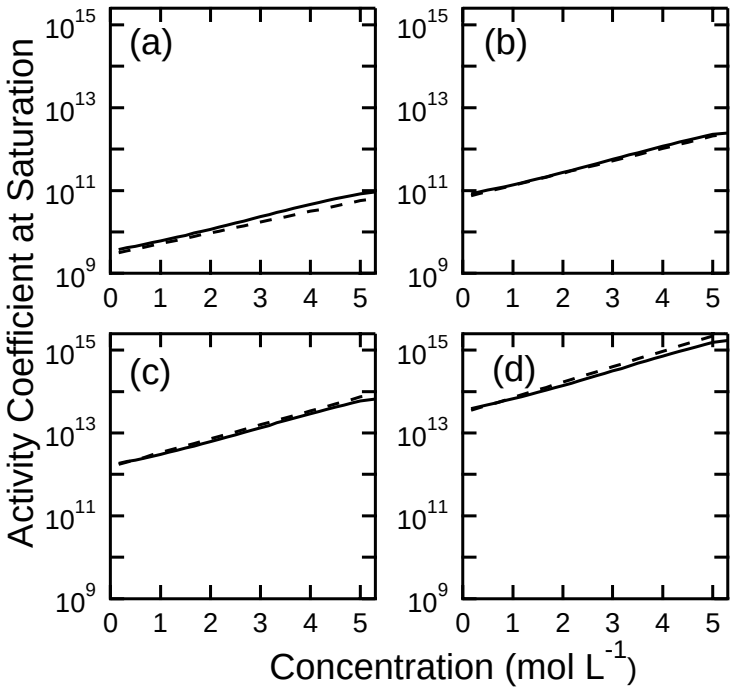

Figure 2.4: Comparison of correlated activity coefficients at saturation in NaCl aqueous solution with parameterized experimental measurements of hexanol. The correlation and empirical parameterization are represented by solid and dashed lines, respectively. The empirical parameterization is taken from Zdenek et al. (1980).

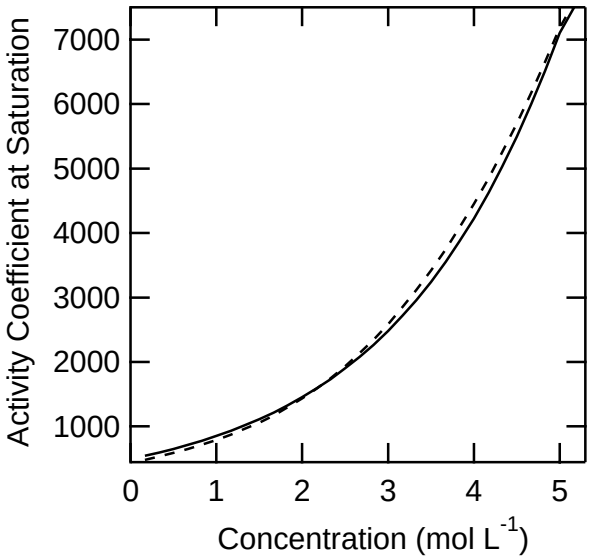

parameters between NaCl and the long–chain –OH group were fitted from these data as shown in Fig. 2.4. The "salting–out" effect results in higher activity coefficients for the organic solute in increasingly concentrated salt solutions. With the solution saturated by NaCl, the activity coefficient of hexanol is approximately 8 times greater than that in pure water. The largest error of 5% occurs in the mixture of hexanol with a saturated NaCl concentration of 5.3 mol L^{-1}. For salt concentrations lower than 2.5 mol L^{-1}, the data correlations are within 3% of experimental measurements.

Multifunctional compounds Glucose and fructose are two representative monosaccharide compounds for which a large amount of phase equilibrium data is available. The equilibrium relative humidity was measured at various concentrations of aqueous solution of glucose and fructose (Peres and Macedo, 1996). Two groups, alcohol (–OH)

in monosaccharides and carboxyl (–$COCH_n$) in monosaccharides, are introduced to represent their ring structure. Because of the large number of polar functional groups existing in the relatively short carbon chains of sugars, the carbon groups in this type of compounds are thought to be similar to those in short–chain monofunctional compounds, for example ethanol and acetic acid. Since the interaction parameters involving CH_n groups in solutions containing short–chain monofunctional compounds have been well studied by LLE–UNIFAC (Magnussen et al., 1981), they are used to describe the carbons in short–chain multifunctional compounds. The correlations shown in Fig. 2.5 are fitted directly to measurements to obtain each parameter. In the aqueous solution of glucose and fructose, the increasing concentrations of solutes lower the concentration of water, and thus the relative humidity. The highest concentrations of two organic solutes correspond to their respective solubility limits. Because glucose (7 mol kg^{-1}) is 50% less soluble than fructose (22 mol kg^{-1}), these two compounds are used to represent low–solubility and high–solubility sugars, respectively. In Fig. 2.5, the calculated relative humidities follow the measurements closely up to solubility limits. The results show that the same set of parameters are applicable to solutes of different solubilities. The errors associated with these correlations are less than 3%.

In hydroxy–acids including malic, tartaric and citric acids, multiple alcohol and carboxylic acid groups coexist in the same short carbon chain. Due to the high ratios of polar to nonpolar groups in diacids, special multifunctional groups, alcohol (–OH) and carboxylic acid (–COOH) in hydroxy–acid, are introduced to incorporate this type of compounds. LLE–UNIFAC parameters are used to describe the carbon groups present in hydroxy-acids. The correlations shown in Fig. 2.6 are fitted to

Figure 2.5: Comparison of correlated relative humidity with measurements at various solute concentrations in aqueous solutions of (a) glucose and (b) fructose. The correlation and experimental measurements are represented by a solid line and open circles, respectively. Experimental data are from Peres and Macedo (1996).

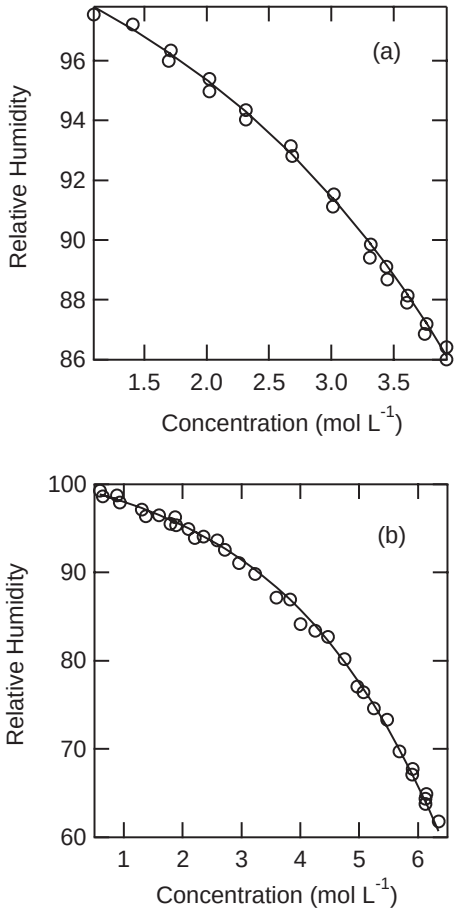

experimental data (Velezmoro and Meirelles, 1998) to obtain parameters for hydroxy-acid interactions with water. The agreement between them is generally good for all three acidgf

s. The largest errors of 2% occur at high concentrations of malic and tartaric acid.

From enthalpy of melting and melting temperature data collected in Acree (1991), the fugacity ratios of a series of diacids (C4–C13 except C11) were calculated from Eq. 2.30. Using the limited solubility data of these compounds (Freier, 1976) in Eq. 2.29, we calculated the activity coefficient at saturation for each species from its known fugacity ratio and solubility. By using two new groups, methyl (CH_n) and carboxylic acid (–COOH) in diacids, the measured activity coefficients between 0.8 to 10^4 at saturation were fit as shown in Fig. 2.7. The diacids with larger carbon numbers usually have higher activity coefficients, a trend shown more distinctly by the fitted correlation. Our correlations agree reasonably well with measurements over the broad range of carbon number of 4 to 13, with a mean deviation of 20%.

The solution systems of glucose–NaCl–water and fructose–NaCl–water for different compositions and their corresponding relative humidities measured by Comesana et al. (1999) were used to fit interaction parameters between ionic groups and multi-functional groups in sugars (Fig. 2.8). Fig. 2.8 (a) and (b) compare the correlations with the experimental results of relative humidity for these ternary systems. For the measured data points, the correlations of the experimental data have errors less than 0.1%. In Fig. 2.8 (c) and (d), the data are reproduced with constant relative humidity isopleths and the measured values. Each line represents a series of concentrations of NaCl and organic solute that have the same relative humidity. The correlated relative humidity decreases with increasing sugar and NaCl concentrations,

Figure 2.6: Comparison of correlated relative humidity with measurements at various solute concentrations in aqueous solutions of (a) malic acid, (b) tartaric acid, and (c) citric acid. The correlation and experimental measurements are represented by solid line and open circles, respectively, in each panel. Experimental data are from Velezmoro and Meirelles (1998).

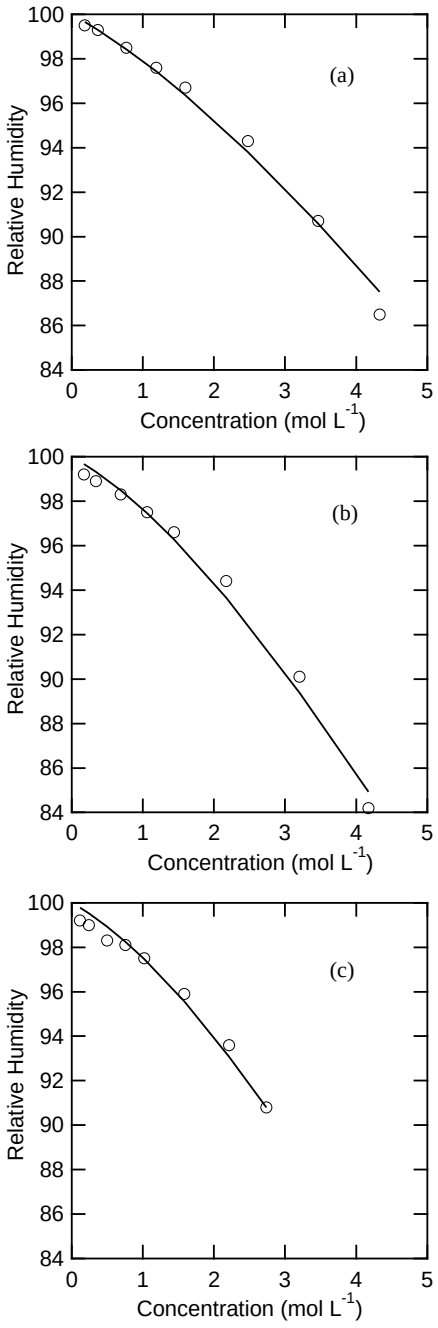

Figure 2.7: Comparison of correlated activity coefficients at saturation in NaCl aqueous solution predicted with measurements for a series of diacids. The correlation and experimental measurements are represented by a solid line and open circles, respectively. Experimental data are from Acree (1991) and Freier (1976).

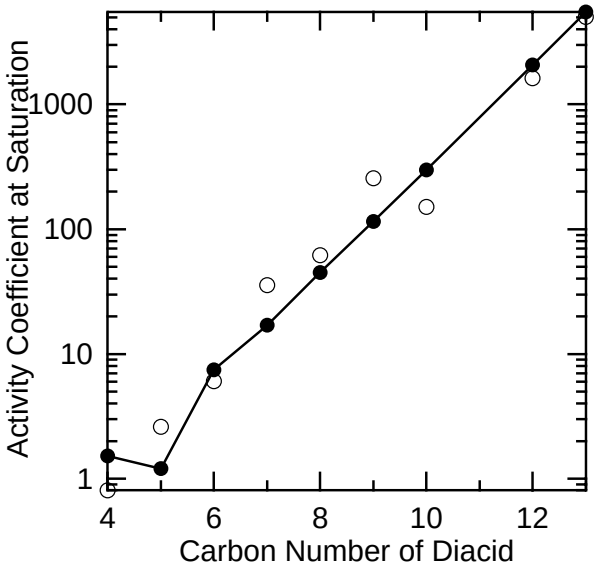

corresponding within 0.1%. This type of simple two-parameter description of the interactions between electrolytes and organic species has also been used successfully to represent measured data by Clegg et al. (2001).

The activity coefficients of tartaric acid calculated from measured aqueous solubilities at different NaCl concentrations (Herz and Hiebenthal, 1929) were fit to interaction parameters between ionic groups and multifunctional groups in hydroxy–acids (Fig. 2.9). The nonideality of the measured solutions is not well predicted by our correlations with average errors up to 53%, but the general trend is reproduced fairly well. More recent measurements of this system were not available to assess the reproducibility of the measurements.

Herz (1909) reported the variation of solubility of succinic acid with the concentration of NaCl aqueous solution. These data were used to fit interaction parameters between groups in diacids and ionic groups (Fig. 2.10). The correlations for solubilities differ less than 1% from the measured solubilities.

2.3 Equilibrium Predictions

Water uptake by soluble components in aerosol results in a change in particle size depending on the relative humidity. In order to quantitatively describe the amount of water absorbed by particles, the hygroscopic growth factor (GF) is defined as the ratio of the diameter $D_{p,RH}$ at a specified relative humidity RH over the original dry diameter $D_{p,dry}$ (measured at a relative humidity that is predicted to be below the efflorescence humidity of all solutes present) (Hämeri et al., 2000):

$$GF(RH) = \frac{D_{p,RH}}{D_{p,dry}} \tag{2.34}$$

Figure 2.8: Comparison of correlated relatively humidity with measurements in glucose–NaCl–water and fructose–NaCl-water solutions. Panels (a) and (b) are the direct comparison for glucose and fructose, respectively. In panels (c) and (d), the correlated lines of constant relative humidity are plotted with data points. Data are grouped according to their corresponding relative humidities. For glucose, five groups, 85%–88% (open diamonds), 88%–91% (open downward-pointing triangles), 91%–94% (open upward-pointing triangles), 94%–97% (open squares), and above 97% (open circles) are represented. For fructose, four groups, 86%–89% (open downward-pointing triangles), 89%–92% (open upward-pointing triangles), 92%–95% (open squares), and above 95% (open circles) are represented. Experimental data are from Comesana et al. (1999).

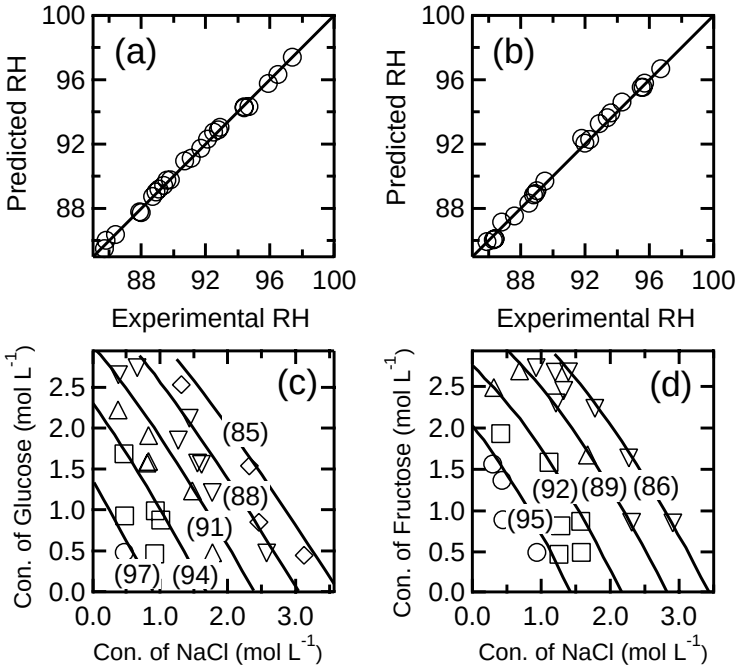

Figure 2.9: Comparison of correlated activity coefficients at saturation in NaCl aqueous solution with measurements for tartaric acid. The correlation and experimental measurements are represented by a solid line and open circles, respectively. Experimental data are from Herz and Hiebenthal (1929).

Figure 2.10: Comparison of correlated solubility in NaCl aqueous solution with parameterized experimental measurements for succinic acid. The model correlation and empirical parameterization are represented by solid and dashed lines, respectively. The empirical parameterization is from Herz (1909).

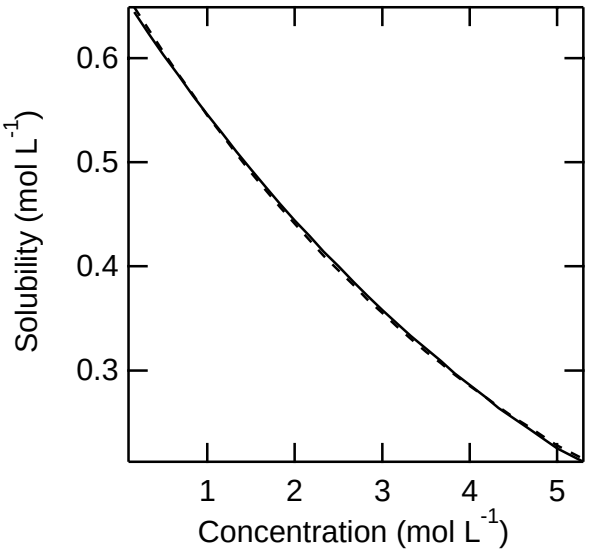

The relative humidity (RH) at equilibrium is related to the activity of water as

$$RH = 100 x_w \gamma_w \tag{2.35}$$

in the bulk solution where the influence of interfacial energy is negligible. For particles smaller than 50 nm in diameter, the Kelvin effect makes the relative humidity at equilibrium higher than the water activity of the aerosol solution (Seinfeld and Pandis, 1997).

The hygroscopic growth factors of marine aerosol have been measured in several field campaigns (Berg et al., 1998; Swietlicki et al., 2000; Zhou et al., 2001). Ming and Russell (2001) present growth factors of sea salt aerosol calculated at various organic contents and initial dry particle sizes using the estimated sea salt particle chemical compositions and comparisons of the model predictions with field measurements. To study the influence of organic compounds of different solubilities on water uptake, here we compare hygroscopic properties of relatively simple mixed ion–organic aerosol predicted by our model to published laboratory measurements (Hämeri et al., 2001; Cruz and Pandis, 2000). In this study, the aerosol is formed by mixing one of three diacids (malonic acid, succinic acid and glutaric acid) with an inorganic salt (either NaCl or $(NH_4)_2SO_4$) at different ratios. The presence of this type of diacid in the atmosphere has been observed by Kawamura et al. (1990). The aqueous solubilities and other chemical information of these compounds are listed in Table. 2.3. Malonic acid and glutaric acid are highly soluble, while succinic acid is only slightly soluble. These three compounds are used as representatives of the soluble (solubility greater than 3 mol L^{-1}) and insoluble (solubility less than 1 mol L^{-1}) organic species present in aerosol particles. Since measured salting-out constants of organic species in $(NH_4)_2SO_4$ solutions are not available, we cannot correlate the interaction parameters of NH_4^+ and SO_4^{2+} with organic groups. Consequently, we have resorted to

assuming their salting-out behavior is similar to Na^+ and Cl^-. Since this assumption is likely to be inaccurate, we estimated the error introduced in this assumption by also assuming no NH_4^+–organic and no SO_4^{2+}–organic interactions (as discussed in the section on model sensitivity). Further refinement of the model to include data for $(NH_4)_2SO_4$ or more similar compounds salting-out constants may improve the model significantly when those data are available.

Pure Substances The predicted hygroscopic growth curves of pure NaCl and $(NH_4)_2SO_4$ are plotted in Fig. 2.11. In aqueous solutions only containing electrolytes, our results reduce to the Pitzer-Simonson-Clegg model, which was shown to represent the experimental data of aqueous solutions of NaCl and $(NH_4)_2SO_4$ within 1% accuracy (Clegg et al., 1992; 1998). The growth factors of particles composed of pure NaCl and pure $(NH_4)_2SO_4$ as measured by Cruz and Pandis (2000) and Hämeri et al. (2001) are included in Fig. 2.11. The measured deliquescence relative humidity (DRH) of each salt agrees with theoretical values (NaCl at 75%; $(NH_4)_2SO_4$ at 80%), although the measured deliquescence processes are not as sharp as predicted. Above the DRH, the particles are predicted to experience smooth growth with increasing relative humidity. However, the measurements of Cruz and Pandis (2000) of $(NH_4)_2SO_4$ differ from those of Hämeri et al. (2001) between relative humidities of 85% and 99% by between 20% and 30%. The strictly inorganic salt hygroscopic growth studies of Hämeri et al. (2000) show better agreement at these high relative humidities for the pure salt cases. The predicted hygroscopic growth of $(NH_4)_2SO_4$ lies between these two measurements for this humidity range.

Predictions for malonic acid and glutaric acid indicate deliquescence at 70% and 92%, respectively, while succinic acid does not take up water until 99% (Fig. 2.12). By constraining the model with solubility data listed in Table 2.3, the compounds

Table 2.3: Properties of inorganic and organic compounds studied in this work.

Compounds	Molecular weight (g mol ^{1})	Solubility (mol L ^{1}) at 298.15 K	Density (g cm ^{3})
NaCl	58.44	4.53	2.17
$(NH_4)_2SO_4$	132.14	3.28	1.77
Malonic acid	104.06	5.98[a]	1.62
Succinic acid	118.09	0.68[a]	1.55
Glutaricacid	132.11	4.07[a]	1.42

[a]Saxena and Hildemann(1996)

Lide (2000)

Figure 2.11: Comparison of predicted and measured hygroscopic growth curves of particles composed of pure NaCl (solid line for bulk case; dotted line for dry diameter of 100 nm) and pure $(NH_4)_2SO_4$ (dashed line for bulk case; dashed–dotted line for dry diameter of 100 nm). The experimental data are from Tang et al. (1986) (solid square for NaCl of bulk case), Tang and Munkelwitz (1994) (solid triangle for $(NH_4)_2SO_4$ of bulk case), Cruz and Pandis (2000) (open square for NaCl of dry diameter of 100 nm; open circle for $(NH_4)_2SO_4$ of dry diameter of 100 nm), Hämeri et al. (2000) (solid diamond for $(NH_4)_2SO_4$ of dry diameter of 50 nm) and Hämeri et al. (2001) (open triangle for $(NH_4)_2SO_4$ of dry diameter of 100 nm). For curves with multiple equilibria near deliquescence, shaded lines show the deliquescence path and shaded dotted lines show unstable equilibria. The same scheme is also used in other figures.

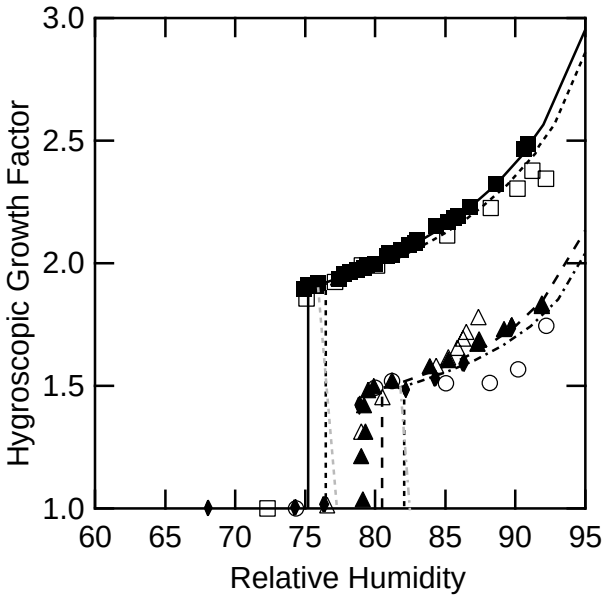

Figure 2.12: Comparison of predicted hygroscopic growth of particles composed of pure substances: (1) solid line for NaCl; (2) dashed line for $(NH_4)_2SO_4$; (3) dotted line for malonic acid; (4) dashed–dotted line for glutaric acid.

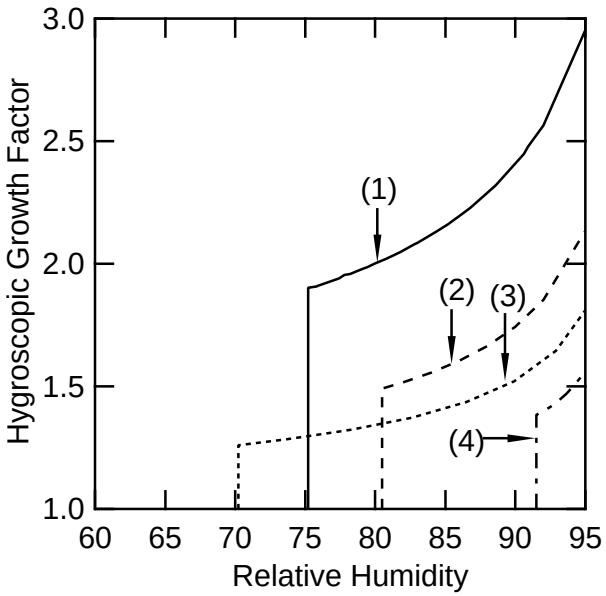

with higher solubility generally tend to deliquesce at lower relative humidity, lowering the predicted DRH. The DRH of glutaric acid measured by Cruz and Pandis (2000) is 85%±5%, roughly consistent with the model prediction.

NaCl with 50% Glutaric Acid (Base Case) The DRH of glutaric acid is between those of malonic acid and succinic acid. Aerosol particles consisting of internally mixed NaCl and glutaric acid each accounted for half of the total dry mass in the base case in this study. In Fig. 2.13, the predicted hygroscopic growth curve of the base case at dry initial diameter of 100 nm together with the measurements by Cruz and Pandis (2000) is compared with the pure NaCl case. Mixing with glutaric acid decreases the DRH of NaCl from 75% to 68% according to the model prediction, whereas the experiments indicate a decrease of less than 3%. At deliquescence, glutaric acid is completely dissolved, while only part of NaCl is dissolved. After that, the

remaining NaCl continues to dissolve and results in almost linear growth with relative humidity between 68% and 72%. After all NaCl dissolves at 72%, the particles grow smoothly with increasing relative humidity. Although the predicted phenomenon of decreased DRH due to mixing with organic species was not observed by Cruz and Pandis (2000), other observational and modeling studies agree with this prediction (Andrews and Larson, 1993; Hansson et al., 1998; Wexler and Seinfeld, 1991). Despite the discrepancy in DRH, the measured growth factors between 75% and 90% relative humidity match the prediction. Compared with the pure NaCl case, the presence of 50% glutaric acid shows a decrease of 30% in growth at relative humidities above 75%, while significant growth occurs between 68% and 75% as a result of decreased DRH.

Varied Organic Fractions The fraction of the total aerosol mass occupied by glutaric acid is increased to 80% to study the impact of the organic fraction on hygroscopic growth. The predicted growth curve and measured data points are shown together with the base case of 50% glutaric acid in Fig. 2.13. Since the DRH is independent of the relative fractions of components, deliquescence still occurs at 68%. However, the increased organic fraction further decreases the growth as compared to the base case. In general, the hygroscopic growth decreased 65% relative to the pure NaCl. In the relative humidity range between 75% and 90%, the predictions and measurements agree within 20%.

Particle Size Variation The growth curves for the base case composition (50% NaCl and 50% glutaric acid) with 15 nm, 35 nm, 50 nm, 75 nm, 100 nm, and 165 nm dry diameter are compared with the bulk case in Fig. 2.14. Surface tension decreases the hygroscopic growth by 3% at 100 nm, 4% at 50 nm, 10% at 35 nm, and 20% at 15 nm relative to the bulk case. The presence of negatively–sloped deliquescence regions

Figure 2.13: Predicted hygroscopic growth of particles (dry diameter 100 nm) with varying organic compositions. The two compositions studied are (1) 50% NaCl and 50% glutaric acid (model prediction: dashed line; experimental measurements: open circle); (2) 80% NaCl and 20% glutaric acid (model prediction: dotted line; experimental measurements: open square); and (3) 100% NaCl (solid line) is included for reference. Experimental data are from Cruz and Pandis (2000).

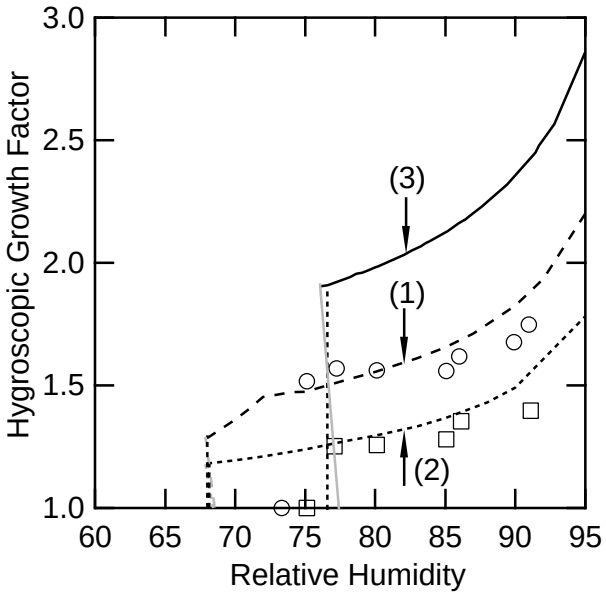

Figure 2.14: Influence of surface tension on hygroscopic growth of 50% NaCl and 50% glutaric acid. The initial dry diameters studied are (1) 15 nm (thick dashed line), (2) 35 nm (thick dotted line), (3) 50 nm (dashed line), (4) 75 nm (dotted line), (5) 100 nm (dashed–dotted line), (6) 165 nm (solid line), and (7) bulk case (thick solid line).

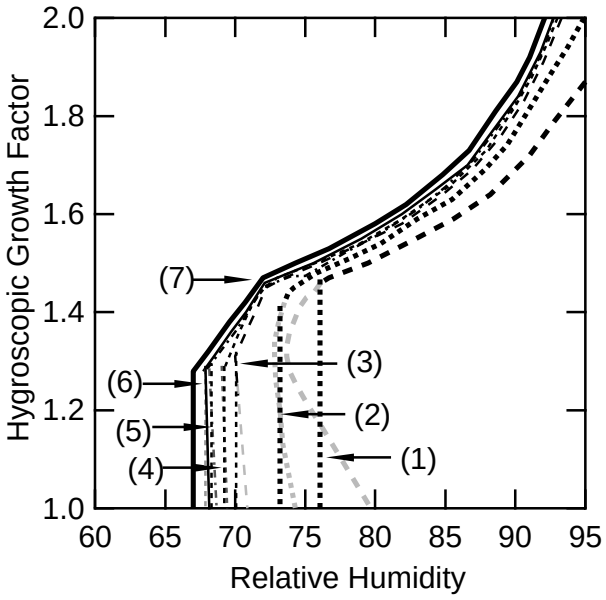

in the smallest particle sizes results from surface tension effects and is discussed in Russell and Ming (2001).

$(NH_4)_2SO_4$ with Organic Acids In Fig. 2.15, the predicted hygroscopic growth curves of three mixtures (50% $(NH_4)_2SO_4$ with 50% malonic acid, $(NH_4)_2SO_4$ with 50% succinic acid, and 50% $(NH_4)_2SO_4$ with 50% glutaric acid) are plotted together with measurements. The inclusion of malonic acid lowers the DRH of pure $(NH_4)_2SO_4$ from 80% to 58%. Hämeri et al. (2001) reported that the particles of this composition grew continuously with increasing relative humidity from 62%. Good agreement between predicted and measured growth occurs in the relative humidity range from 60% to 80%. As in the pure $(NH_4)_2SO_4$ case, the predicted growth is less than the measurements above 80%. The predicted DRH of $(NH_4)_2SO_4$ with 50% succinic acid

Figure 2.15: Predicted hygroscopic growth of particles (dry diameter 100 nm) with varying compositions. The compositions studied are (1) 50% $(NH_4)_2SO_4$ and 50% malonic acid (model prediction: dashed line; experimental measurements: open circles), (2) 50% $(NH_4)_2SO_4$ and 50% succinic acid (model prediction: dotted line; experimental measurements: open squares), (3) 50% $(NH_4)_2SO_4$ and 50% glutaric acid (model prediction: dashed–dotted line), and (4) 100% $(NH_4)_2SO_4$ (solid line). Experimental data are from Hämeri et al. (2001).

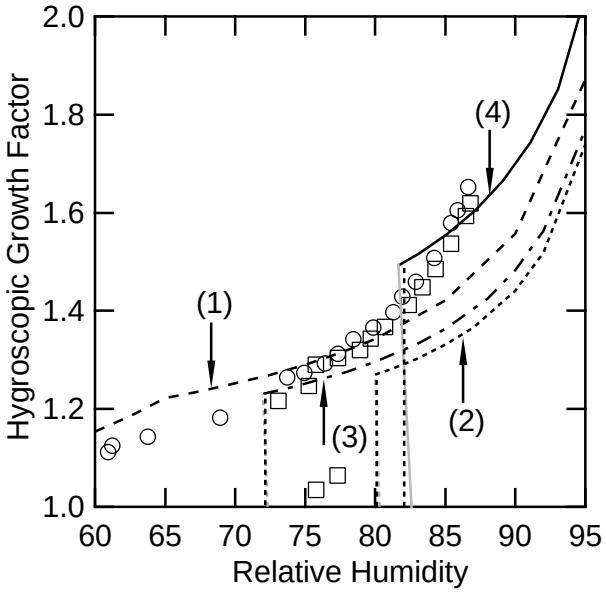

remains at 80% since the solubility of succinic acid is small. At the relative humidity above 80%, the predicted growth is well below measurements. Similar to malonic acid, glutaric acid is also able to decrease the DRH of $(NH_4)_2SO_4$ from 80% to 72%. Above 80%, its growth is slightly higher than succinic acid and significantly lower than malonic acid. Although the presence of all three diacids lowers the water uptake after 80%, the particles containing the more soluble organic species tend to grow bigger than those with the less soluble species. The model predicts that the presence of 50% malonic acid decreases the growth by 20% relative to pure $(NH_4)_2SO_4$, while 50% glutaric acid and 50% succinic acid cause decreases of 35% and 38%, respectively.

2.4 Model Sensitivity

In order to assess the sensitivity of the model to the many empirical parameterizations that we have employed, we compare here a series of different approaches to our most important assumptions, namely the organic-ion interaction parameters, interactions between $(NH_4)_2SO_4$ and organics, internal and external mixing states, and empirical correlations of diacids.

Organic–Ion Interaction Parameters In the calculation of organic–ion interaction parameters for UNIFAC, the volume and area parameters R_i and Q_i of ion i in Eq. 4 of Fredenslund et al. (1975) are arbitrarily set to be equal to those of water. Hence the combinatorial contribution to activity coefficient reduces to zero for inorganic–only aqueous solutions. Because the Pitzer-Simonson-Clegg model solely determines the properties of such solutions, the predictive accuracy of our model is the same as the Pitzer-Simonson-Clegg model that has been well developed for inorganic solutions. Macedo et al. (1990) suggested treating R_i and Q_i as adjustable parameters and fitting them to experimental data. The Kikic et al. (1991) model used the R_i and Q_i values given by Macedo et al. (1990). Fig. 2.16 compares these alternative parameterizations to our approach of setting them equal to those of water.

In Fig. 2.16, the hygroscopic growth curves of pure NaCl predicted in two cases are compared with experimental data (Tang et al., 1986). Using identical values of R_i and Q_i as for water cancels the combinatorial contribution to the overall activity coefficients. Our model fully accounts for the growth and compares well with measurements. In the Macedo et al. (1990) approach, the non–zero combinatorial contribution shifted the predicted DRH of pure NaCl to 80%. At relative humidities higher than DRH, the growth predicted by this approach is 5% lower than our model and the measurements of Tang et al. (1986).

Figure 2.16: Comparison of predicted and measured hygroscopic growth curves of particles (dry diameter 100 nm) composed of pure NaCl. The predictions show (1) this work (solid line) and (2) Macedo et al., 1991 (dashed line). Data (solid square) are from Tang et al. (1986).

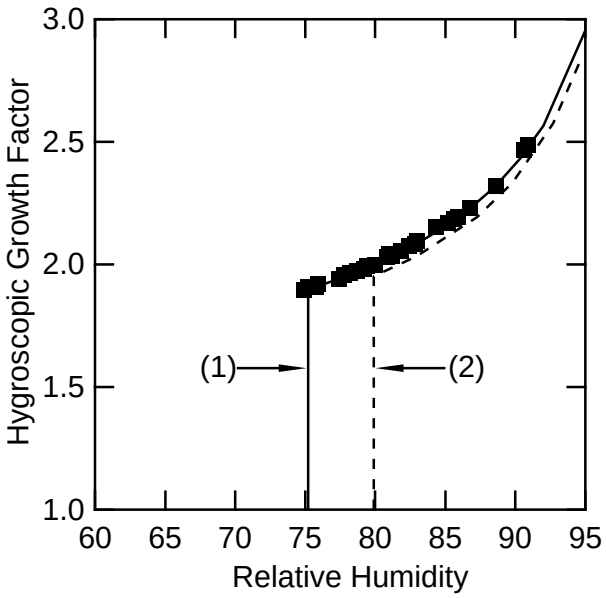

Figure 2.17: Comparison of predicted solubility in NaCl aqueous solution with parameterized experimental measurements for succinic acid. The predictions are based on (1) this work (dashed line) and (2) Macedo et al., 1991 (dotted line). Experimental data (3, solid line) are from Herz and Hiebenthal (1929).

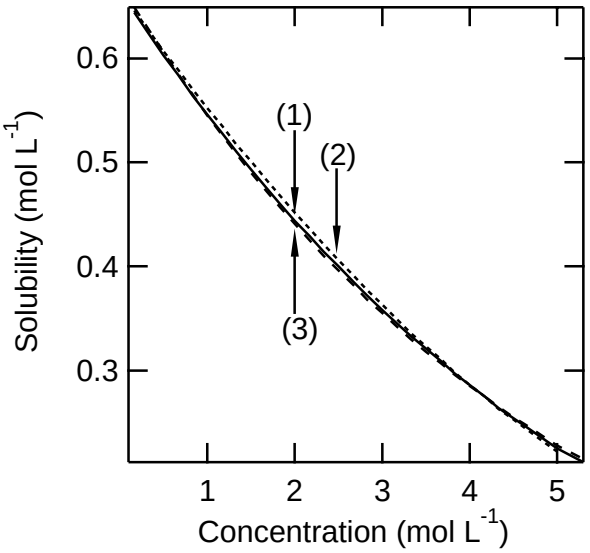

The ability of different R_i and Q_i values to also represent the "salting–out" effect is illustrated in Fig. 2.17. Both types of parameters are able to correlate the general trend of solubility of succinic acid in NaCl aqueous solution. Our correlation agrees with measurements generally within 2%, while using the parameters given by Macedo et al. (1990) results in an average deviation of 6%.

The hygroscopic growth curves of particles with a composition of 50% NaCl and 50% glutaric acid are calculated from the interaction parameters fitted from solubility data. With the Macedo et al. (1990) parameters, the mixture deliquesces at a relative humidity of 77%, slightly higher than that of pure NaCl (75%) as shown in Fig. 2.18.

Interactions between $(NH_4)_2SO_4$ and organics In the previous calculations, the interaction parameters of NH_4^+ and SO_4^{2-} with organic groups are replaced by

Figure 2.18: Comparison of predicted hygroscopic and measured hygroscopic growth curves of particles (dry diameter 100 nm) of 50% NaCl and 50% glutaric acid. The curves illustrate (1) model predicted mixture behavior from this work (dashed line) and (2) Macedo et al., 1991 (dotted line); and (3) pure NaCl. Data (open circles) are from Cruz and Pandis (2000).

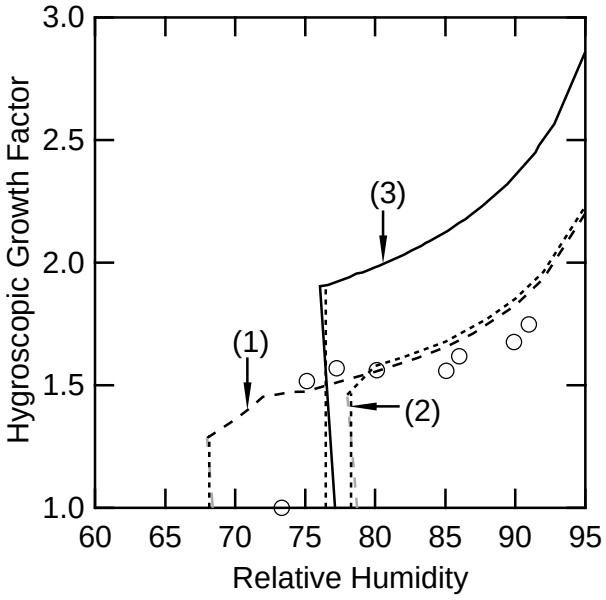

Figure 2.19: Influence of interaction between $(NH_4)_2SO_4$ and organic compounds on hygroscopic growth of 50% $(NH_4)_2SO_4$ and 50% glutaric acid. Predictions were calculated (1) with interaction (solid line), (2) without interaction (dashed line) and (3) with interaction twice as strong as NaCl (dotted line).

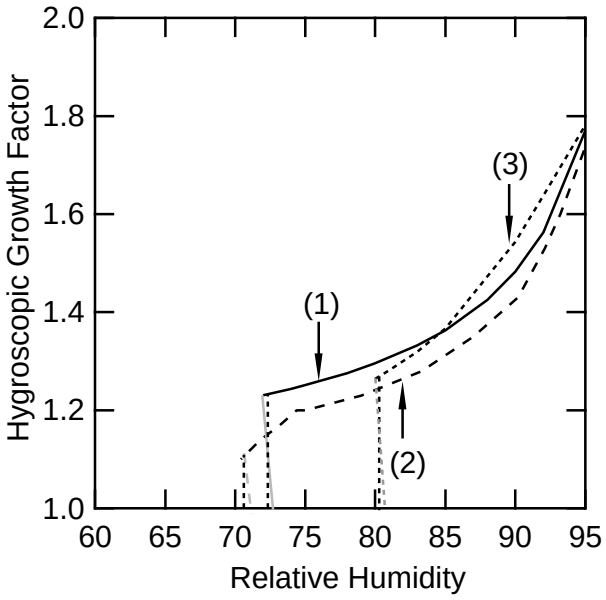

those of Na^+ and Cl^-. In order to test the uncertainty caused by this assumption on hygroscopic growth, we recalculate the growth curve of 50% glutaric acid with 50% $(NH_4)_2SO_4$ by assuming no interaction and doubling the interaction between them and comparing to the growth curve with interaction in Fig. 2.19. In general, the interaction between $(NH_4)_2SO_4$ and glutaric acid assists the water uptake. The growth without interaction is 10% lower than that with interaction; doubling the strength of the interaction results in a 10% increase in the growth factor. The elimination of ion–organic interaction also reduces the DRH to 71%, while the DRH remains at 80% with doubling the strength.

Internal and External Mixing States In the previous model calculation, we assume that the inorganic and organic components in aerosol are internally mixed.

Compared to the pure salt case, mixing with organic compounds decreases water uptake at relative humidities above the DRH. In addition, the soluble organic compounds lower the mixture DRH from that of the pure salt and result in considerable growth at low relative humidities. Since measurements suggest that particles often exist in external mixtures, we study here the influence of mixing state on hygroscopic growth.

The normalized water content (WC) is defined as the ratio of the mass of absorbed water in particles $m_{w,RH}$ at a specific relative humidity RH over the total dry particle mass $m_{p,dry}$:

$$WC(RH) = \frac{m_{w,RH}}{m_{p,dry}} \tag{2.36}$$

The average water content of an externally mixed aerosol is defined as

$$WC(RH) = \varepsilon_O WC_O(RH) + (1 - \varepsilon_O) WC_S(RH) \tag{2.37}$$

where $WC_O(RH)$ and $WC_S(RH)$ are the water contents of a pure organic compound and salt at relative humidity RH, respectively, and ε_O is the organic mass fraction in the dry particle. The average water contents for particles of four different compositions are calculated by assuming external mixing, and the results are compared with the respective internal cases in Fig. 2.20. In the externally mixed case, the DRH of each component is unchanged from its pure value. Therefore, there is no growth until the relative humidity increases to the lowest DRH of all pure components. Each component begins to contribute to the overall growth only when its DRH is reached. For particles containing soluble compounds such as malonic acid and glutaric acid, the external growth is less than internal growth before the organic component is dissolved. After the dissolution of the organic component, the externally mixed aerosol grows more than the internally mixed one. In the case of the low–solubility succinic

Figure 2.20: Predicted average water contents of particles by assuming internal (solid line) and external (dashed line) mixing for (a) 50% NaCl and 50% glutaric acid, (b) 50% $(NH_4)_2SO_4$ and 50% malonic acid, (c) 50% $(NH_4)_2SO_4$ and 50% succinic acid, and (d) 50% $(NH_4)_2SO_4$ and 50% glutaric acid.

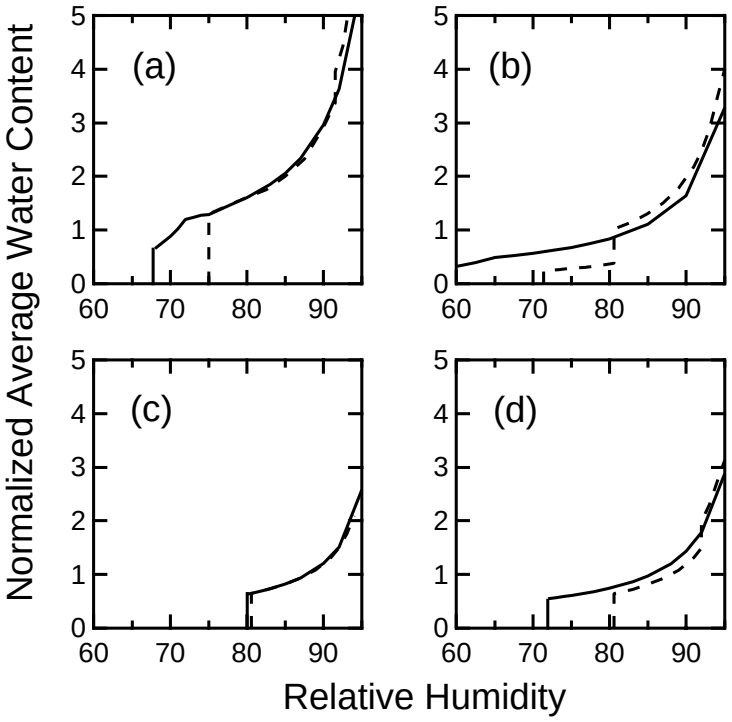

acid, the external growth is approximately the same as the internal growth, since the DRH of succinic acid is higher than 99% . The largest deviation of 10% between internal and external growth is observed in the case containing the highly soluble species malonic acid. For less soluble succinic acid and glutaric acid, the two types of growth generally agree within 3%.

Empirical Correlations of Diacids The uncertainties of the measurements used for model parameterization result in analogous uncertainties in the model calculations. Since experimental errors can be propagated in our calculation, the individual model parameters were varied to quantify the resulting errors associated with the predicted

hygroscopic growth factors.

The model sensitivity to the interaction parameters involving monofunctional compounds, sugars and hydroxy-acids has been examined by Ming and Russell (2001). Two other types of interactions used in the base case (50% NaCl with 50% glutaric acid) are (1) interactions between diacids and water and (2) interactions between diacids and electrolytes. The sensitivity of the base case calculation is summarized in Table 2.4. At two representative relative humidities 73% and 85%, the change in the calculated hygroscopic growth factors caused by errors in experimental data used is less than 1%.

2.5 Conclusions

A thermodynamic model was developed to describe the phase equilbria of electrolyte-organic mixtures in aerosol particles. Three types of contributions to activity coefficients including ion–water, organic–water and ion–organic interactions are accounted for by combining the Pitzer-Simonson-Clegg model and the UNIFAC framework into a general model. The model is parameterized by fitting interaction parameters from experimental data collected in the literature. The accuracy of the model correlations compare well with available measurements. The hygroscopic growth curves calculated by the model achieve good agreement with measurements (Cruz and Pandis, 2000; Hämeri et al, 2001). The results show that the water uptake by ion–organic mixtures is influenced by the solubility of organic components. The presence of 50% malonic acid in $(NH_4)_2SO_4$ reduces the growth by 20%, while a 30% decrease is incurred by 50% succinic acid. The soluble organic components can also decrease the DRH of a pure salt. The model predicts that mixing with 50% malonic acid lowers the DRH of

Table 2.4: Sensitivity of model predictions to experimental uncertainty in data used in empirical correlations.

Parametersin model	Type of input data	Uncertainty of input data	Sensitivity [a] of growth factor at 73% (85%) relative humidity
Volume and area parameters for organic–ion interactions	Parameterstted from experimental data (Macedo et al., 1991)	±50%	1.656±0.003
Salting–outeect of NH_4^+ and SO_4^{2-}	Solubility of succinic acid in NaCl aqueous solution (Herz, 1909)	±5%	1.1552±0.085 [c] 1.306±0.063
Externalmixtures	Field measurements (Middlebrook et al., 1998)	100% external, 100% internal	1.656±0.001
Interaction parameters between CH_n and H_2O in diacids	Activity coecien ts at saturation (Acree, 1991; Freier, 1976)	±50%	1.462±0.008 1.656±0.003
Interaction parameters between ions and groups in diacids	Solubility of succinic acid in NaCl aqueous solution (Herz, 1909)	±5%	1.462±0.014 1.656±0.012

[a] ± Variationrepresents the sensitivity of the predictionto the uncertainty in the experimental data used in the correlationof model parameters.

Uncertainty is given at 85% relative humidity because 73% is below the deliquescence relative humidity.

[c] The growth factors and associated uncertainties are calculatedfor 50% $(NH_4)_2SO_4$ and 50% glutaricacid.

$(NH_4)_2SO_4$ from 80% to 58%.

The approach of treating the volume and area parameters in UNIFAC as adjustable (Kikic et al, 1991) shifted the predicted DRH of pure NaCl to 80%, as opposed to 75% predicted by our model and measured by Tang et al. (1986). Doubling and eliminating the ion-organic interaction between $(NH_4)_2SO_4$ and glutaric acid increase and lower the hygroscopic growth factor by 10%, respectively. Comparisons of the growth curves of internally and externally mixed aerosol indicate that the DRH of an internal mixture is lower than that of an external mixture, and the external mixture grows over 3% more than the internal mixture after all soluble components are dissolved. The change in the hygroscopic growth factors caused by errors in experimental data used in the model parameterization is less than 1%.

References

Acree, W. E. (1991). Thermodynamic Properties of Organic Compounds: Enthalpy of Fusion and Melting Point Temperature Compilation, *Thermochimica Acta* 189:37-56.

Andrews, E., and Larson, S. M. (1993). Effect of Surfactant Layers on the Size Changes of Aerosol-Particles as a Function of Relative-Humidity, *Environ. Sci. Technol.* 857-865.

Ansari, A. S., and Pandis, S. N. (2000). Water Absorption by Secondary Organic Aerosol and Its Effect on Inorganic Aerosol Behavior, *Environ. Sci. Technol.* 34:71-77.

Bastos, J. C., Soares, M. E., and Medina, A. G. (1988). Infinite Dilution Activity Coefficients Predicted by UNIFAC Group Contribution, *Ind. Eng. Chem. Res.*

27:1269-1277.

Berg, O. H., Swietlicki, E., Krejci, R. (1998). Hygroscopic growth of Aerosol Particles in the Marine Boundary Layer over the Pacific and Southern Oceans During the First Aerosol Characterization Experiment (ACE 1), *J. Geophys. Res.* 103:16535-16545.

Clegg, S. L., Pitzer, K. S., and Brimblecombe, P. (1992). Thermodynamics of Multicomponent, Miscible, Ionic-Solutions. 2. Mixtures Including Unsymmetrical Electrolytes, *J. Phys. Chem.* 96:9470-9479.

Clegg, S. L., Pitzer, K. S., and Brimblecombe, P. (1994). Correction, *J. Phys. Chem.* 98:1368.

Clegg, S. L., Pitzer, K. S., and Brimblecombe, P. (1995). Correction, *J. Phys. Chem.* 99:6755.

Clegg, S. L., Brimblecombe, P., and Wexler, A. S. (1998). Thermodynamic Model of the System H^+-NH_4^+-Na^+-SO_4^{2-}-NO_3^--Cl^--H_2O at 298.15 K, *J. Phys. Chem. A* 102:2155-2171.

Clegg, S. L., Seinfeld, J. H., and Brimblecombe, P. (2001). Thermodynamic Modelling of Aqueous Aerosols Containing Electrolytes and Dissolved Organic Compounds, *J. Aerosol Sci.* 32:713-738.

Comesana, J. F., Correa, A., and Sereno, K. (1999). Measurements of Water Activity in "Sugar" Plus Sodium Chloride Plus Water Systems at 25 Degrees C, *J. Chem. Eng. Data* 44:1132-1134.

Corrigan, C. E., and Novakov, T. (1999). Cloud Condensation Nucleus Activity of Organic Compounds: A Laboratory Study, *Atmos. Environ.* 33A:2661-2668.

Cruz, C. N., and Pandis, S. N. (1997). A Study of the Ability of Pure Secondary

Organic Aerosol to Act as Cloud Condensation Nuclei, *Atmos. Environ.* 31A:2205-2214.

Cruz, C. N. and Pandis, S. N. (2000). Deliquesence and Hygroscopic Growth of Mixed Inorganic–Organic Atmoshperic Aerosol, *Environ. Sci. Technol.* 34:4313-4319.

Duce, R. A., Mohnen, V. A., Zimmerman, P. R., Grosjean, D., Cautreels, W., Chatfield, R., Jaenicke, R., Ogren, J. A., Pellizzari, E. D., and Wallace, G. T. (1983). Organic Material in the Global Troposhpere, *Rev. Geophys.* 21:921-952.

Fredenslund, A., Gmehling, J., and Rasmussen, P. (1977). *Vapor-Liquid Equilibrium Using UNIFAC*, Elsevier, Amsterdam.

Fredenslund, A., Jones, and R. L., Prausnitz, J. M. (1975). Group-Contribution Estimation of Activity Coefficients in Nonideal Liquid Mixtures, *AIChE J.* 21:1086-1099.

Freier, R. K. (1976). *Aqueous Solutions Data for Inorganic and Organic Compounds.* W. De Gruyter, New York.

Gagosian, R. B., Peltzer, E. T., and Zafiriou, O. C. (1981). Atmospheric Transport of Continentally Derived Lipids to the Tropical North Pacific, *Nature* 291:312-315.

Gmehling J., Rasmussen P., and Fredenslund, A. (1982). Vapor-liquid Equilibria by UNIFAC Group Contribution. Revision and Extension. 2, *Ind. Eng. Chem. Process Des. Dev.* 21:118-127.

Gmehling, J. (1995). From UNIFAC to Modified UNIFAC to PSRK with the Help of DDB, *Fluid Phase Equilibr.* 107:1-29.

Gogou, A. I., Apostolaki, M., and Stephanou, E. G. (1998). Determination of Organic Molecular Markers in Marine Aerosols and Sediments: One-step Flash Chromatography Compound Class Fractionation and Capillary Gas Chromatographic

Analysis, *J. Chromatogr. A* 799:215-231.

Hämeri, K., Charlson, R., and Hansson, H. C. (2001). Hygroscopic Properties of Particles Containing Ammonium Sulphate Mixed with Carboxylic Acids, *AIChE J.* submitted to this issue.

Hämeri, K., Väkevä, M., Hansson, H. C., and Laaksonen, A. (2000). Hygroscopic Growth of Ultrafine Ammonium Sulfate Aerosol Measured Using a Ultrafine Tandem Differential Mobility Analyzer, *J. Geophys. Res.* 105:22231-22242.

Hansson, H. C., Rood, M. J., Koloutsou-Vakakis, S., Hämeri, K., Orsini, D., and Wiedensohler, A. (1998). NaCl Aerosol Particle Hygroscopicity Dependence on Mixing with Organic Compounds, *J. Atmos. Chem.* 31:321-346.

Herz, W. (1909). Ein Beispiel von Löslichkeitsbeeinflussung, *Z. anorg. Chem.* 65:341-344.

Herz, W., and Hiebenthal, F. (1929). Über Löslichkeitsbeeinflussungen, *Z. anorg. allgem. Chem.* 177:363-380.

Kawamura, K., and Gagosian, R. B. (1990). Midchain Ketocarboxylic Acids in the Remote Marine Atmosphere – Distribution Patterns and Possible Formation Mechanisms, *J. Atmos. Chem.* 11:107-122.

Kikic, I., Fermeglia, M., and Rasmussen P. (1991). UNIFAC Prediction of Vapor–Liquid Equilibria in Mixed Solvent–Salt Systems, *Chem. Engng. Sci.* 46:2775-2780.

Köhler, H. (1921). Zur Kondensation des Wasserdampfe in der Atmoshpäre, *Geofys. Publ.* 2:3-15.

Kojima, K., Zhang, S., and Hiaki, T. (1997). Measuring Methods of Infinite Dilution Activity Coefficients and A Database for Systems Including Water, *Fluid Phase Equilibria* 131:145-179.

Laaksonen, A. (1993). The Composition Size Dependence of Aerosols Created by

Dispersion of Surfactant Solutions, *J. Colloid Interf. Sci.* 159:517-519.

Li, J. D., Polka, H. M., and Gmehling, J. (1994). A G(E) Model for Single and Mixed-Solvent Electrolyte System. 1. Model and Results for Strong Electrolytes, *Fluid Phase Equilibr.* 94:89-114.

Li, Z. B., Li, Y. G., and Lu, J. F. (1999). Surface Tension Model for Concentrated Electrolyte Aqueous Solutions by the Pitzer Equation, *Ind. Eng. Chem. Res.* 38:1133-1139.

Lide, D. R., Ed. (2000). *CRC Handbook of Chemistry and Physics.* CRC Press, Boca Raton.

Long, F. A., and McDevit, W. F. (1952). Activity Coefficients of Nonelectrolyte Solutes in Aqueous Salt Solutions, *Chem. Rev.* 51:119-169.

Macedo, E., Skovborg, P., and Rasmussen P. (1990). Calculation of Phase Equilibria for Solutions of Strong Electrolytes in Solvent–Water Mixtures, *Chem. Engng. Sci.* 45: 875-882.

Magnussen, T., Rasmussen, P., and Fredenslund, A. (1981). UNIFAC Parameter Table for Prediction of Liquid-Liquid Equilibria, *Ind. Eng. Chem. Process Des. Dev.* 20:331-339.

Meng, Z. Y., Seinfeld, J. H., Saxena, P., and Kim, Y. P. (1995). Atmospheric Gas– Aerosol Equilibrium. 4. Thermodynamics of Carbonates, *Aerosol Sci. Technol.* 23:131-154.

Middlebrook, A. M., Murphy, D. M., and Thomson, D. S. (1998). Observations of Organic Material in Individual Marine Particles at Cape Grim During the First Aerosol Characterization Experiment (ACE 1), *J. Geophys. Res.* 103:16475-16483.

Ming, Y., and Russell, L. M. (2001). Predicted Hygroscopic Growth of Sea Salt Aerosol, *J. Geophys. Res.* 106:28259-28274.

Mirabel, P., Reiss, H., and Bowles, R. K. (2000). A Theory for the Deliquescence of Small Particles, *J. Chem. Phys.* 113:8200-8205.

More, J. J., Garbow, B. S., and Hillstrom, K. E. (1980). *User Guide for MINPACK-1.* Argonne National Laboratory, Argonne, Il.

Nath, S. (1999). Surface Tension of Nonideal Binary Liquid Mixtures as a Function of Composition, *J. Colloid Interf. Sci.* 209:116-122.

Park, J. H., Lee, J. E., and Carr P. W. (1991). The Predictive Accuracy for Estimating Infinite Dilution Activity Coefficients by γ^{∞}-Based UNIFAC, *J. Solution Chem.* 20:1189-1198.

Peters, C. A., Wammer, K. H., and Knightes, C. D. (2000). Multicomponent NAPL Solidification Thermodynamics, *Transport Porous Med.* 38:57-77.

Pividal, K. A., and Sandler, S. I. (1990). Neighbor Effects on the Group Contribution Method – Infinite Dilution Activity-Coefficients of Binary–Systems Containing Primary Amines and Alcohols, *J. Chem. Eng. Data* 35:53-60.

Peres, A. M., and Macedo, E. A. (1997). A Modified UNIFAC Model for the Calculation of Thermodynamic Properties of Aqueous and Non-aqueous Solutions Containing Sugars, *Fluid Phase Equilibr.* 139:47-74.

Reid, R.C., Prausnitz, J. M., and Poling, B.E. (1987). *The Properties of Gases and Liquids.* McGraw-Hill, Boston.

Riley, J. P., and Chester, R. (1971). *Introduction to Marine Chemistry.* Academic Press, 1971.

Rogge, W. F., Mazurek, M. A., Hildemann, L. M., Cass, G. R., and Simoneit B. R. T. (1993). Quantification of Urban Organic Aerosols at a Molecular–Level – Identification, Abundance and Seasonal–Variation, *Atmos. Environ.* 27A:1309-1330.

Russell, L. M., and Ming, Y. (2001). Deliquescence of Small Particles, *J. Chem.*

Phys. in press.

Russell, L. M., Noone, K. J., Ferek, R. J., Pockalny R. A., Flagan R. C., and Seinfeld J. H. (2000). Combustion Organic Aerosol as Cloud Condensation Nuclei in Ship Tracks, *J. Atmos. Sci.* 57:2591-2606.

Saxena, P., and Hildemann, L. M. (1996). Water–Soluble Organics in Atmospheric Particles: a Critical Review of the Literature and Application Of Thermodynamics to Identifyy Candidate Compounds, *J. Atmos. Chem.* 24:57-109.

Saxena, P., and Hildemann, L. M. (1997). Water Absorption by Organics: Survey of Laboratory Evidence and Evaluation of UNIFAC for Estimating Water Activity, *Environ. Sci. Technol.* 31:3318-3324.

Saxena, P., Hildemann, L. M., McMurry, P., and Seinfeld, J. H. (1995). Organics Alter Hygroscopic Behavior of Atmospheric Particles, *J. Geophys. Res.* 100:18755-18770.

Seinfeld, J. H., and Pandis, S. N. (1997) *Atmospheric Chemistry and Physics.* John Wiley & Sons, New York.

Silcock, H. L. (1979) *Solubilities of Inorganic and Organic Compounds* Pergamon, Oxford.

Skjold-Jørgensen, S., Kolbe, B., Gmehling, J., and Rasmussen, P. (1979). Vapor-Liquid Equilibria by UNIFAC Group Contribution. Revision and Extension, *Ind. Eng. Process Des. Dev.* 18:714-722.

Stokes, R. H., and Robinson, R. A. (1966). Interactions in Aqueous Nonelectrolyte Solutions: I. Solute–Solvent Equilibria, *J. Phys. Chem.* 70:2126-2130.

Sutton, C., and Calder, J. A. (1974). Solubility of Higher–Molecular–Weight *n*-Paraffins in Distilled Water and Seawater, *Environ. Sci Technol.* 8:654-657.

Swietlicki, E., Zhou, J. C., Covert, D. S., Hämeri, K., Busch, B., Väkeva, M.,

Dusek, U., Berg, O. H., Wiedensohler, A., Aalto, P., Mäkelä, J., Martinsson, B. G., Papaspiropoulos, G., Mentes, B., Frank, G., and Stratmann, F. (2000). Hygroscopic Properties of Aerosol Particles in the Northeastern Atlantic during ACE-2, *Tellus B* 52:750-778.

Tang, I. N., and Munkelwitz, H. R. (1994). Water Activities, Densities, and Refractive Indices of Aqueous Sulfates and Sodium Nitrate Droplets of Atmospheric Importance, *J Geophys. Res.* 99:18801–18808.

Tang, I. N., Munkelwitz, H. R., and Wang N. (1994). Water Activity Measurements with Single Suspended Droplets: The NaCl-H_2O and KCl-H_2O Systems, *J. Colloid Interface Sci.* 114:409-415;

Turpin, B. J., Huntzicker, J. J., Larson, S. M., and Cass, G. R. (1991). Los–Angeles Summer Midday Particulate Carbon – Primary and Secondary Aerosol, *Environ. Sci. Technol.* 25:1788-1793.

Velezmoro, C. E., and Meirelles, A. J. A. (1998). Water Activity in Solutions Containing Organic Acids, *Dry Technol.* 16:1789-1805.

Wexler, A. S., Seinfeld, J. H. (1991). 2nd–Generation Inorganic Aerosol Model, Atmos. Environ. A 25:2731-2718.

Wu, H. S., and Sandler, S. I. (1989). Proximity Effects on the Predictions of the UNIFAC Model. 1. Ethers, *AIChE J.* 35:168-172.

Wu, H. S., and Sandler, S. I. (1991). Use of Ab Initio–Quantum Mechanics Calculations in Group Contribution Methods. 2. Test of New Groups in UNIFAC, *Ind. Eng. Chem. Res.* 30:889-897.

Yan, W. D., Topphoff, M., Rose, C., and Gemhling, J. (1999). Prediction of Vapor-Liquid Equilibria in Mixed-Solvent Electrolyte Systems Using the Group Contribution Concept, *Fluid Phase Equilibria* 162:97-113.

Zdenek, S., Strnadova, L., and Rod, V. (1980). Contribution to the Application of Scaled Particle Theory to Prediction of the Salting Coefficient, *Coll. Czech. Chem. Commun.* 45:679-689.

Zhang, S., Hiaki, T., Hongo, M., and Kojima K. (1998). Prediction of Infinite Dilution Activity Coefficients in Aqueous Solutions by Group Contribution Models. A Critical Evaluation, *Fluid Phase Equilibria*, 144:97-112.

Zhang, Y., Seigneur, C., Seinfeld, J. H., Jacobson, M., Clegg, S. L., and Binkowski, F. S. (2000) A Comparative Review of Inorganic Aerosol Thermodynamic Equilibrium Modules: Similarities, Differences, and Their Likely Causes, *Atmos. Environ.* 34:117-137.

Zhou, J., Swietlicki, E., Berg, O. H., Aalto, P. P., Hämeri, K., Nilsson, E. D., and Leck, C. (2001). Hygroscopic Properties of Aerosol Particles over the Central Arctic Ocean during Summer, *J. Geophys. Res.,* in press.

Chapter 3

Deliquescence of Small Particles

3.1 Deliquescence of Wetted Particles

Mirabel et al. (2000) proposed a scenario for prompt deliquescence of particles that identified the deliquescence relative humidity predicted for a change from a dry crystal particle to a dissolved salt droplet. This approach relies on the particle being dry at the point of deliquescence. While this assumption may hold for some salts, several studies have shown that water adsorbs approximately two monolayers of water on the crystal surface by the time the relative humidity reaches 45%, with four layers accumulating at 70% (Lad, 1968; Barraclough and Hall, 1974; Estel et al., 1976; Ghosal and Hemminger, 1999; Finlayson-Pitts and Hemminger, 2000). In fact, recent work has suggested anomalously high water amounts below the deliquescence relative humidity of 400 nm particles (Weis and Ewing, 1999). Hence, for deliquescence points at higher relative humidities, the Gibbs free energy of the phase change should be predicted by difference of the dissolved particle compared to the wetted particle rather than a dry crystal (Wang et al., 1998). The systems described by the coated and uncoated models are illustrated schematically in Fig. 3.1.

The difficulty of this approach is that it requires describing the free energy of the

Figure 3.1: Schematic diagram of deliquescence of a salt crystal with two models: the coated model assumes that prior to deliquescence multiple water layers will be adsorbed on the crystal surface whereas the uncoated model assumes the interface is the solid crystal. The difference for dry particles smaller than 100 nm dry diameter is that, when compared with the deliquescence of a bulk phase, the uncoated model predicts lower deliquescence relative humidities and the coated model predicts higher deliquescence relative humidities.

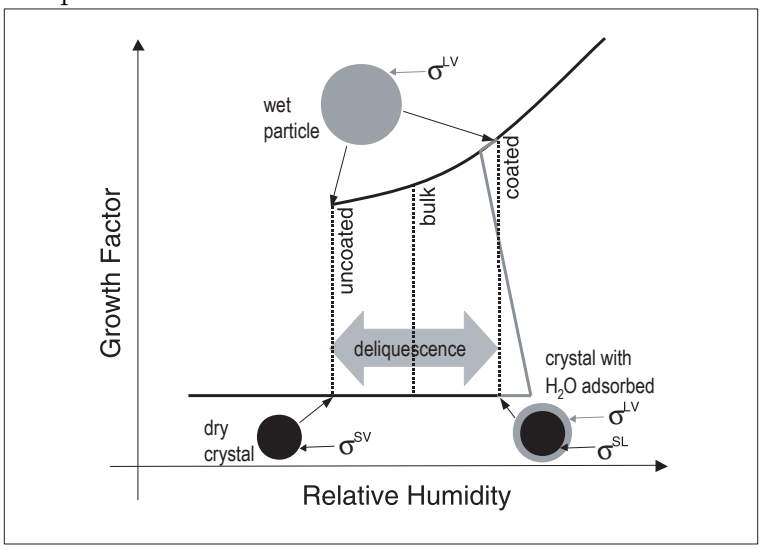

adsorbed water layer and its interface, since the surface energy of a thin adsorbed layer on a crystal of unknown geometry is poorly constrained. However, Peters and Ewing have shown that the properties of the adsorbed layer in humid conditions are indistinguishable from an aqueous salt solution, so that the use of bulk liquid surface properties is appropriate (Peters and Ewing, 1997; Foster and Ewing, 1999; Foster and Ewing, 2000). Consequently, we make the simplifying assumption that the crystal or any remaining undissolved fraction is spherical. For the case of a powder or a partially dissolved crystal, this approach has considerable support (Espenschied et al., 1964; Defay et al., 1966).

The second assumption is that the surface energy of the interior and exterior interfaces of this spherical shell of water can be described by such a crude concept as bulk surface tension. Several authors have noted the inadequacy of bulk surface tension for finite–molecule systems such as nucleating clusters, and the same criticism applies to our current usage (Defay et al., 1966; Girshick and Chiu, 1990; Wilemski, 1995). We believe this approach is more appropriate regardless for the non–prompt case, since these limitations are primarily relevant to the early stages of water condensation onto the particle. For both cases the point at which deliquescence occurs is dependent on the adsorbed liquid amount and the surface energy of that thin layer. We believe that bulk surface tension values are the best estimate currently available for this purpose, and recent work experimentally verifying the Kelvin effect for cyclohexane bubbles as small as 4 nm suggests that it may be appropriate in some cases (Fisherand Israelachvili, 1979). To quantify the potential impact of variation of surface tension for finite–molecule situations (Girshick and Chiu, 1990), we have studied the sensitivity of this prediction to size–dependent surface tension using a simple Tolman length model (Defay et al., 1966).

The coated model is described by the following equation for the free energy G of the aerosol system (including solid S NaCl, liquid L consisting of water and dissolved NaCl, and vapor V containing water and air):

$$G_{\text{coated}} = \mu^{\text{S}}_{\text{coated}} n^{\text{S}}_{\text{coated}} + \mu^{\text{L}}_{\text{coated}} n^{\text{L}}_{\text{coated}} + \mu^{\text{V}}_{\text{coated}} n^{\text{V}}_{\text{coated}} + \sigma^{\text{SL}} a^{\text{SL}}_{\text{coated}} + \sigma^{\text{LV}} a^{\text{LV}}_{\text{coated}} \quad (3.1)$$

where μ_S, μ_L, and μ_V are the chemical potentials of the solid, liquid and vapor phases (assuming only one phase of each type), respectively, and n_S, n_L, and n_V are the numbers of moles of the solid, liquid, and vapor phases, respectively (Mirabel et al., 2000). Note that μ_{L} is a function of the mole fraction of NaCl dissolved, x_{NaCl}. The free energies of the solid–liquid (SL) and liquid–vapor (LV) interfaces are given by the products of their surface tensions σ^{SL} and σ^{LV} and the interfacial areas a^{SL} and a^{LV}. The subscript coated is used to indicate the phase model described for the two models illustrated in Fig. XXZ. The particle before deliquescence in the uncoated model has no liquid phase and is simply represented by

$$G_{\text{uncoated}} = \mu^{\text{S}}_{\text{uncoated}} n^{\text{S}}_{\text{uncoated}} + \mu^{\text{V}}_{\text{uncoated}} n^{\text{V}}_{\text{uncoated}} + \sigma^{\text{SV}} a^{\text{SV}}_{\text{uncoated}} \quad (3.2)$$

. Once the crystal phase has disappeared in either model, there is only a liquid phase and a vapor phase such that the free energy simplifies to the following for the wet droplet

$$G_{\text{wet}} = \mu^{\text{L}}_{\text{wet}} n^{\text{L}}_{\text{wet}} + \mu^{\text{V}}_{\text{wet}} n^{\text{V}}_{\text{wet}} + \sigma^{\text{LV}} a^{\text{LV}}_{\text{wet}} \quad (3.3)$$

In order to compare free energies of these wet and dry (coated and uncoated) particles, we reference the free energy to standard reference states, such that

$$\Delta G_{\text{coated}} \equiv G_{\text{coated}} - G^0 \quad (3.4)$$

Note that the reference state G^0 is the same for both wet and dry forms in both the coated and uncoated models since it is dependent only on the total amounts of NaCl

and H_2O in all phases of the system:

$$G^0 \equiv G^0_{\rm wet} \equiv G^0_{\rm coated} \equiv G^0_{\rm uncoated} \tag{3.5}$$

The change in free energy due to deliquescence is then described by the difference between the wet droplet and the dry particle, so that for the coated particle model we can write

$$\begin{aligned} \Delta G^{\rm deliq}_{\rm coated} &\equiv \Delta G_{\rm wet} - \Delta G_{\rm coated} \\ &= \mu^{\rm L}_{\rm wet} n^{\rm L}_{\rm wet} + \mu^{\rm V}_{\rm wet} n^{\rm V}_{\rm wet} + \sigma^{\rm LV} a^{\rm LV}_{\rm wet} \\ &- \mu^{\rm S}_{\rm coated} n^{\rm S}_{\rm coated} - \mu^{\rm L}_{\rm coated} n^{\rm L}_{\rm coated} - \mu^{\rm V}_{\rm coated} n^{\rm V}_{\rm coated} - \sigma^{\rm SL} a^{\rm SL}_{\rm coated} - \sigma^{\rm LV} a^{\rm LV}_{\rm coated} \end{aligned} \tag{3.6}$$

in which the reference states have cancelled out. For the uncoated model, the free energy change at deliquescence is dependent on the solid/vapor interfacial energy rather than the solid/liquid energies. It can be written as:

$$\begin{aligned} \Delta G^{\rm deliq}_{\rm uncoated} &\equiv \Delta G_{\rm wet} - \Delta G_{\rm uncoated} \\ &= \mu^{\rm L}_{\rm wet} n^{\rm L}_{\rm wet} + \mu^{\rm V}_{\rm wet} n^{\rm V}_{\rm wet} + \sigma^{\rm LV} a^{\rm LV}_{\rm wet} \\ &- \mu^{\rm S}_{\rm uncoated} n^{\rm S}_{\rm uncoated} - \mu^{\rm V}_{\rm uncoated} n^{\rm V}_{\rm uncoated} - \sigma^{\rm SV} a^{\rm SV}_{\rm uncoated} \end{aligned} \tag{3.7}$$

Deliquescence occurs when the free energy of the completely wet droplet ($G_{\rm wet}$) equals that of the water–coated crystal ($G_{\rm coated}$), which can be expressed as the difference in those free energies $\Delta G^{\rm deliq}$ for either the coated or uncoated model equalling zero:

$$\Delta G^{\rm deliq}_{\rm coated} = 0 \tag{3.8}$$

and

$$\Delta G^{\rm deliq}_{\rm uncoated} = 0 \tag{3.9}$$

The equilibria found from this equation are not necessarily stable points, so we examine later the question of which predicted equilibrium point is stable for specified

conditions. After dissolution of solid species, both Eq. (3.8) and (3.9) reduce to the familiar Kelvin equation

$$\begin{aligned} RH &\equiv \frac{100 \times p_w(D_p)}{p_w^o} \\ &= 100 \times x_w \gamma_w \exp(\frac{4M_w\sigma^{LV}}{RT\rho_w D_p}) \end{aligned} \tag{3.10}$$

where RH is the relative humidity of water vapor, p_w is the water vapor pressure in equilibrium with a particle of diameter D_p, p_w^o is the saturation vapor pressure of water, σ^{LV} is the surface tension at the liquid/vapor interface, x_w and γ_w are the mole fraction and activity coefficient of water in the aerosol phase, respectively, and M_w and ρ_w are the molecular weight and density of water at temperature T.

3.2 Comparison of Deliquescence Models

To illustrate the behavior of the coated model to the idealized, uncoated model, Fig. 3.2 shows the dependence of the predicted deliquescence relative humidity ratio R on particle size, where

$$R \equiv \frac{DRH(D_p)}{DRH(D_p^\infty)} \tag{3.11}$$

and DRH is the Deliquescence Relative Humidity, or the relative humidity at which the wet droplet is stable with respect to the dry (coated or uncoated) salt crystal, D_p is the dry particle diameter, and D_p^∞ is a diameter sufficient large that the particle behavior is negligibly different from a bulk solution (i.e. typically greater than 100 nm diameter for the species studied in this work). The coated model predicts higher values of DRH and R than the idealized uncoated model for all values of surface tension (Mirabel et al., 2000).

Since a sodium chloride solution is highly nonideal, the ideal solution assumption

Figure 3.2: Predicted deliquescence relative humidity ratio R as a function of dry particle size. The thick and thin curves correspond to σ^{SV} values at (a) 100 and (b) 270 mN m^{-1}, respectively. The different line styles represent (1) uncoated model (Mirabel et al., 2000) with ideal solution, constant partial molar volume $\bar{v}$, and σ^{LV}=70 mN m^{-1} (dotted line), (2) uncoated particle model with ideal solution, measured $\bar{v}$, and σ^{LV}=70 mN m^{-1} (dashed line), (3) uncoated particle model with ideal solution, measured $\bar{v}$, and σ^{LV}=83 mN m^{-1} (dashed-dotted line), (4) uncoated particle model with real solution, constant $\bar{v}$, and σ^{LV}=70 mN m^{-1} (dashed-dotted-dotted line), and (5) coated particle model with real solution, measured $\bar{v}$, and σ^{LV}=83 mN m^{-1} (solid line) (this work).

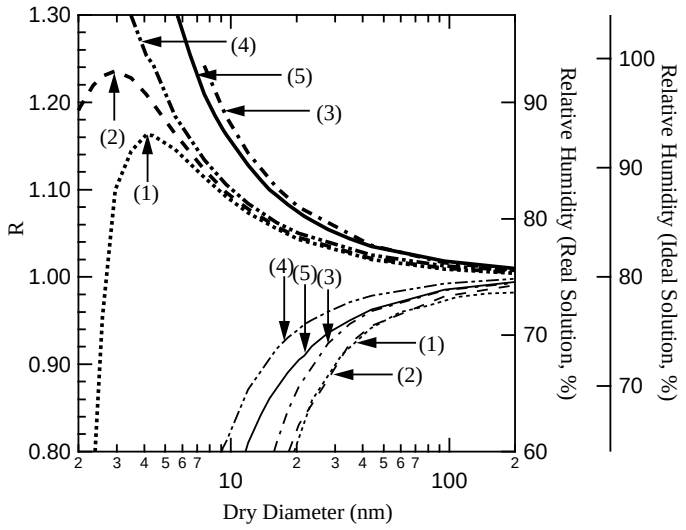

and assigned solubility of 0.20 changes $DRH(D_p^{\infty})$ from 75% to 80% (Mirabel et al., 2000), but this assumption shows only a small change on the value of the R in Fig. 3.2 since these values have been normalized to remove this discrepancy. Nonetheless the actual DRH changes significantly as is illustrated by the comparison of R values to the equivalent real–solution DRH and ideal–solution DRH in the right–hand axes of Fig. 3.2.

The assumption that a particle will be coated prior to deliquescence when it is in equilibrium at a relative humidity of 70% accounts for the majority of the increase in R. The uncoated model compares the change in free energy from dry crystal to droplet, so that the only interface in the undeliquesced particle is the solid/vapor interface. This interfacial energy is characterized by the crystal surface tension which has been measured to be 213 mN m^{-1} (Adamson, 1996), although the uncertainty is large and ranges from 100 to 270 mN m^{-1}. For the coated model, the undeliquesced particle has two interfaces, the solid/liquid and liquid/vapor interfaces with surface tensions $\sigma^{\mathrm{SL}} = 29 \pm 20$ mN m^{-1} and $\sigma^{\mathrm{LV}} = 83 \pm 2$ mN m^{-1} (Abramzon and Gauberk, 1993; Adamson, 1996; Wu and Nancollas, 1999). The coated model then has significantly higher R, since the liquid/vapor interfacial pressure partially counteracts the solid/liquid interfacial pressure and since the solid/liquid interfacial tension is much lower than that of a solid/vapor interface (Wang et al., 1998).

Figure 3.3 show the impact of surface tension on the predicted deliquescence relative humidity ratio R. Figures 3.4 and 3.5 illustrate the range of probable values for these surface tensions in order to summarize the behavior of each model given current surface tension measurements (Abramzon and Gauberk, 1993; Adamson, 1996; Wu and Nancollas, 1999). The isopleths show the boundary between $R > 1$ and $R < 1$ for three sizes of dry particle for which the coated particle model predicts a significant

variation of DRH with particle size. The shaded ranges illustrate the best current reported measurements for both models. While there is some uncertainty in these values, current measurements predict the coated model to be $R > 1$ and the uncoated model to give $R < 1$ for respective surface tension ranges appropriate for NaCl. The robustness of the coated results mean that the use of bulk σ may not introduce a significant error from the size–dependent behavior of small surfaces, so that the results predicted here will be retained qualitatively once the dependence of surface tension on clusters of small sizes can be measured. A lower bound for this model is 8 nm dry diameter since smaller particles do not deliquesce below saturation with the coated model.

The weakness of this approach is in modeling the thin liquid layer as bulk liquid interfaces to the solid and vapor phases. It is likely that the solid–liquid interface is characterized by an interfacial region of quasi–solid, quasi–liquid molecules that has properties dissimilar from bulk liquid and solid phases. For particles greater than 15 nm dry diameter, this liquid layer will be sufficiently thick for growth factors greater than 1.2 (corresponding to approximately a 20–water molecule thick layer) that the bulk properties are appropriate to use. Section 3.4 investigates the role of this assumption is studied by evaluating the hygroscopic growth with a Tolman length dependence of surface tension on size (Defay et al., 1966). However, recent work suggests that even three to four layers of adsorbed water will exhibit properties of bulk water, suggesting that the bulk interface behavior may be appropriate (Peters and Ewing, 1997a; Peters and Ewing, 1997b; Foster and Ewing, 1999; Foster and Ewing, 2000).

Incorporating concentration–varying density in the calculation also increases the predicted deliquescence relative humidity (Tang et al., 1986). This approach accounts

Figure 3.3: Comparison of deliquescence relative humidity ratio R predicted with dry and coated models. For the uncoated particle model (thin lines), Mirabel et al. (2000) considered the case of σ^{LV}=70 mN m^{-1} and the following range of solid/vapor surface tension values: (1) σ^{SV}=100 mN m^{-1} (solid line), (2) σ^{SV}=112 mN m^{-1} (dashed-dotted line), (3) σ^{SV}=200 mN m^{-1} (dotted line), and (4) σ^{SV}=270 mN m^{-1} (dashed line). For the coated model proposed in this work (thick lines), σ^{LV}=83 mN m^{-1} and the following range of solid/liquid surface tension values have been studied: (5) σ^{SL}=17 mN m^{-1} (thick dotted line), (6) σ^{SL}=29 mN m^{-1} (thick solid line, base case), (7) σ^{SL}=67 mN m^{-1} (thick dashed line), (8) σ^{SL}=117 mN m^{-1} (thick dashed-dotted line), and (9) σ^{SL}=187 mN m^{-1} (thick dashed-dotted-dotted line).

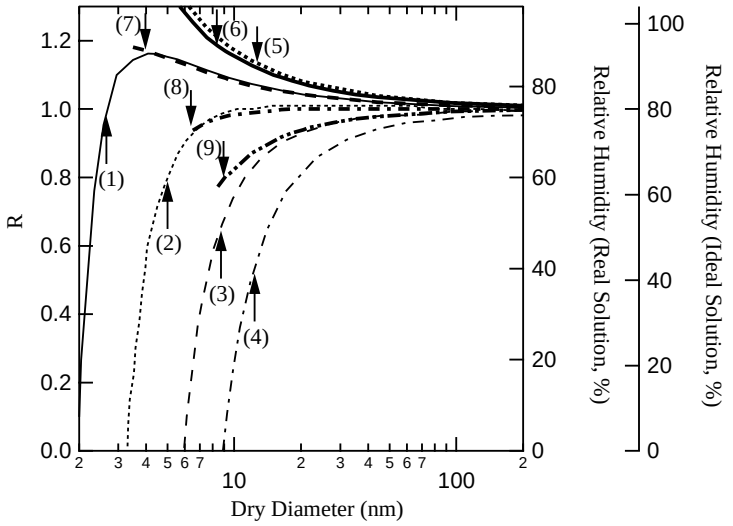

Figure 3.4: Constant deliquescent relative humidity ratio isopleths at $R = 1$ for ranges of solid/liquid surface tension σ^{SL} and liquid/vapor surface tension σ^{LV} for the coated particle model (Adamson, 1996; Wu and Nancollas, 1999). Dry diameter sizes shown here are (1) 8 nm (dashed line), (2) 15 nm (solid line), (3) 35 nm (dotted line), and (4) 50 nm (dashed-dotted line). The shaded area illustrates the current reported measurements of σ^{SL} and σ^{LV}. The circle represents the values used in model.

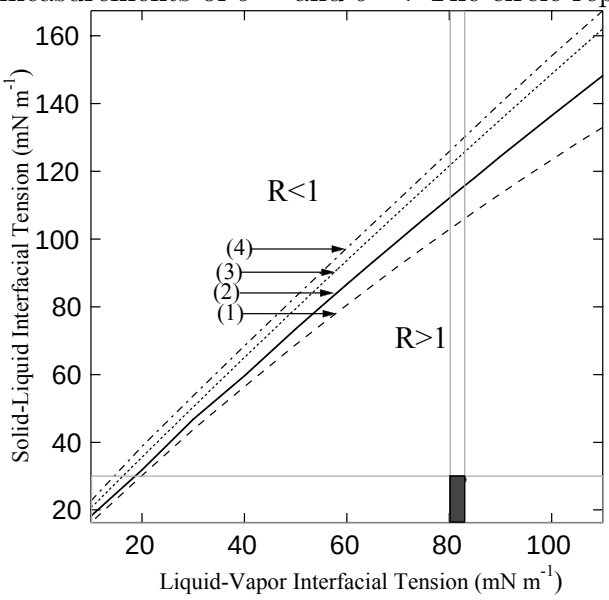

Figure 3.5: Isopleths of $R = 1$ with respect to σ^{SV} and σ^{LV} for the uncoated particle model (Abramzon and Gauberk, 1993; Adamson, 1996). Dry diameter sizes are (1) 8 nm (dashed line), (2) 15 nm (solid line), (3) 35 nm (dotted line), and (4) 50 nm (dashed-dotted line). The shaded area illustrates the current reported measurements of σ^{SV} and σ^{LV}. Circles represent values used Fig. 3.3.

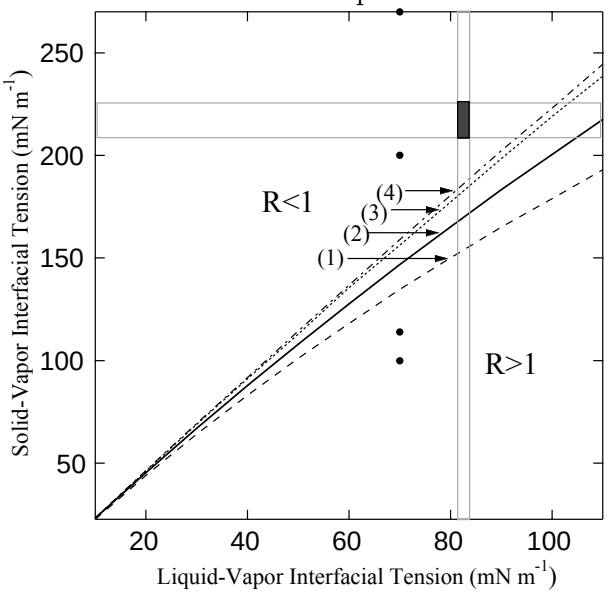

for a 4% increase over the prediction assuming constant density. The effect of this assumption is illustrated in Fig. 3.2.

An additional simplifying assumption in the model is that the crystal, its coating, and the droplet are all spherical. (This assumption is employed in both the coated and uncoated models.) For the coated model, the determining factor in the calculation is the shape of the coated particle. Some crystal species including ammonium sulfate are nearly spherical. Typical atmospheric particles such as mixtures of inorganic salts with organic impurities are likely to be nearly amorphous in the dry state rather than forming crystals, and such amorphous solids can be appropriately considered spherical. Nearest–neighbor and surface–defect considerations suggest that even those particles that tend to be cuboidal when dry will have their corners rounded by the presence of adsorbed water layers (Allen et al., 1998). For particles smaller than 10 nm coated by three or more layers of water molecules, the coated particle is likely to have curvature similar to a sphere of equal mass. To bound the uncertainty in shape, the effect of a cubic crystal is illustrated in section 3.4.

3.3 Hygroscopic Growth and Stability

The equilibria predicted by Eq. (3.8) and (3.9) determined for the coated and uncoated modelsmay be stable, unstable or metastable under humid atmospheric conditions. To assess the stability of the predicted equilibria, we evaluate

$$\frac{\partial^2 G^{\text{deliq}}_{\text{coated}}}{\partial x^2_{\text{NaCl}}} \approx \frac{\partial \Delta G^{\text{deliq}}_{\text{coated}}}{\partial x_{\text{NaCl}}}. \tag{3.12}$$

This second derivative of the free energy describes the change of the slope of the free energy and represents a minimum in free energy internal to the parameter boundaries

if and only if

$$\frac{\partial^2 G^{\text{deliq}}_{\text{coated}}}{\partial x^2_{\text{NaCl}}} > 0. \tag{3.13}$$

Such a minimum will form a stable equilibrium, as small perturbations will return to this value. Unstable equilibria are characterized by

$$\frac{\partial^2 G^{\text{deliq}}_{\text{coated}}}{\partial x^2_{\text{NaCl}}} < 0, \tag{3.14}$$

where x_{NaCl} is the mole fraction of sodium chloride dissolved in the aqueous phase. An equilibrium satisfying this condition will be a local maximum. This value is in equilibrium, but any infinitesimally small perturbations will drive the particle to a lower free energy state. Since there is a finite amount of salt in a fixed dry diameter particle that can dissolve, the problem also has extreme bounding values that may represent stable states at

$$x_{\text{NaCl}} = 0 \tag{3.15}$$

and at

$$x_{\text{NaCl}} = 1. \tag{3.16}$$

Stability is attributed to the lowest free energy configuration even if it is a bounding point.

The hygroscopic growth factor predicted for subsaturated relative humidity by the coated and uncoated ("prompt") models show significant differences. Figure 3.6 illustrates the prompt deliquescence of the uncoated model and the multiple–equilibria region of the coated model. Both models predict two equilibria between deliquescence and efflorescence, namely for relative humidities below 75%, where the upper wet branch is metastable with respect to the dry branch in this region (Tang et al., 1986). However, the coated model predicts a three–equilibria region between 80% and 87%, prompting an investigation of which equilibrium is the stable one. Figure

Figure 3.6: Predicted hygroscopic growth factor of 15 nm dry diameter NaCl particles for (1) coated and (2) uncoated deliquescence models.

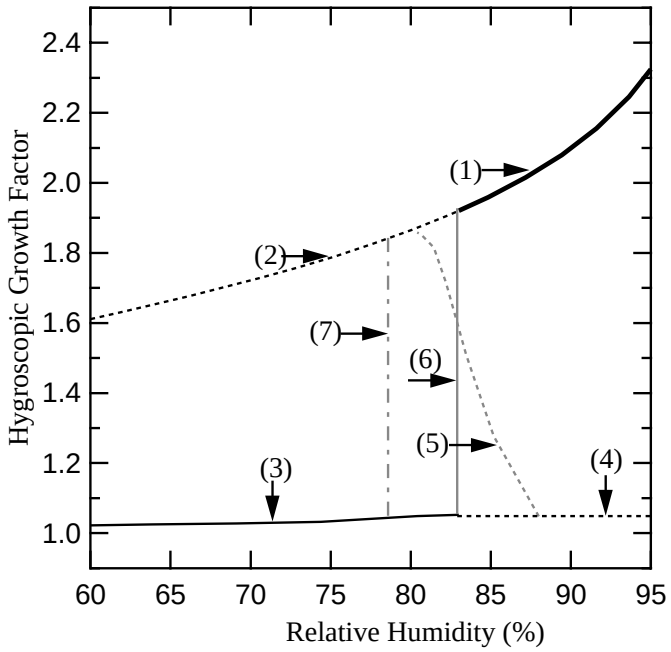

3.7 shows the effect of different model assumptions for the dry model on the predicted hygroscopic growth.

At constant relative humidity, the stability of each equilibrium is determined by the second derivative of the free energy surface with respect to either a constant amount of condensed water or a constant amount of dissolved NaCl. Figure 3.8 shows examples of the free energy surface for the equilibrium regions of the hygroscopic growth factor behavior at relative humidities of 73% and 75% (in the two–equilibrium region), 81%, 83%, and 85% (in the three–equilibrium region), and 90% (in the one–equilibrium region). To facilitate interpretation of these three–dimensional surfaces, Fig. 3.9 illustrates a slice through the free–energy minimum trough of each surface plotted against the mass ratio of condensed water. In the two–equilibria region below 80%, the dry equilibrium is more stable than the wet. In the three–equilibria

Figure 3.7: Predicted hygroscopic growth curves with dry and coated models for the uncoated particle model: (1) ideal solution, constant molar partial volume $\bar{v}$, and σ^{LV}=70 mN m^{-1} (solid line), (2) ideal solution, measured $\bar{v}$, and σ^{LV}=70 mN m^{-1}(dotted line), (3) ideal solution, measured $\bar{v}$, and σ^{LV}=83 mN m^{-1} (dashed line), 4 real solution, constant $\bar{v}$, and σ^{LV}=70 mN m^{-1} (dashed line). For the coated model, one curve is shown for (5) real solution, measured $\bar{v}$, and σ^{LV}=83 mN m^{-1} (dashed-dotted line). The dotted lines represent deliquescence. The grey dashed–dotted line represents unstable equilibria in coated model.

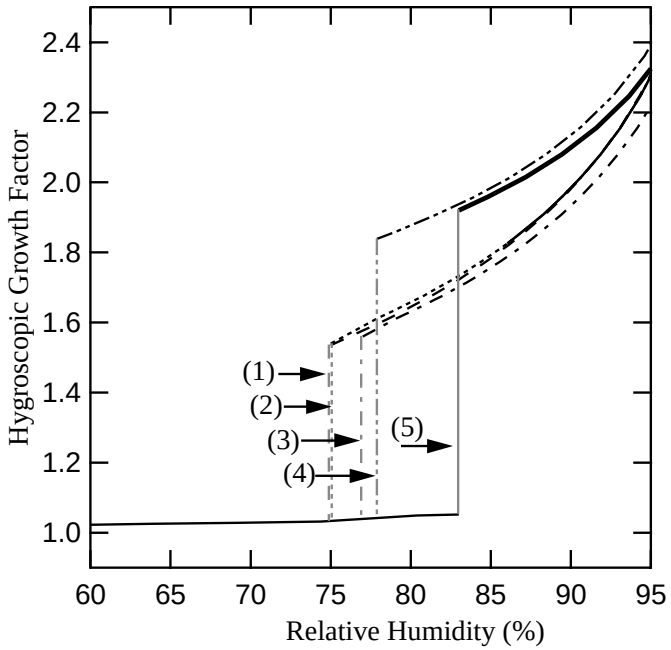

Figure 3.8: Three-dimensional Gibbs free energy surface plotted against condensed water and dissolved NaCl at various relative humidites.

region, the dry equation continues to have the minimum equilibrium from 80% to 83%. The difference is that a third unstable equilibrium exists where the free energy goes through a maximum value. Since this value is a maximum the equilibrium is clearly unstable, so the stable value is given by one of the extreme endpoints; at 81% relative humidity the dry branch has the lower free energy and will be stable. At 83% relative humidity, the dry and wet particles have equal free energy, so deliquescence occurs. Above this relative humidity, the most stable equilibrium continues to be the wet branch, and this continues into the one–equilibrium region above 87%.

This transition from dry to wet equilibrium is summarized in Fig. 3.10, in which the free energy of the dry, wet and deliquescing branches are plotted. The dry branch has the lowest free energy up to 83% relative humidity when it is crossed by the wet branch in the coated model. The uncoated model has a substantially higher dry free energy, resulting in crossing the wet branch at a lower relative humidity. This model (with an appropriate solid–vapor surface tension and without idealizations) predicts the transition from dry to wet at 78%.

3.4 Dependence of Deliquescence Relative Humidity on Particle Size

To illustrate the consequences of this behavior for deliquescence and hygroscopic growth of small particles, Fig. 3.12 and 4.1 show, respectively, the free energies and growth factors of particles between 3 nm and 100 nm dry diameter. At 100 nm, the deliquescence relative humidity of NaCl particles is negligibly different from

Figure 3.9: Minimum Gibbs free energy plotted against condensed water at various relative humidites.

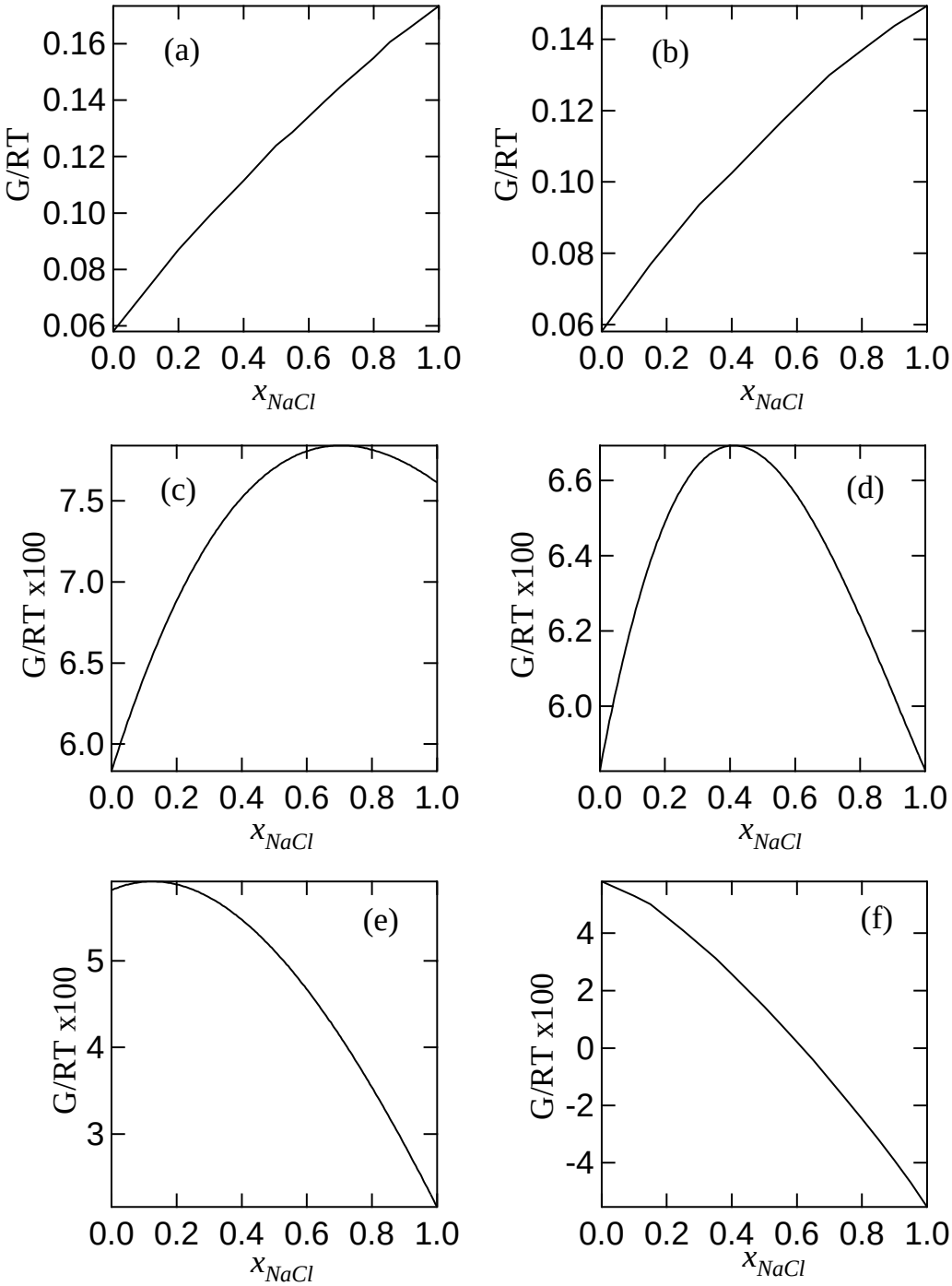

Figure 3.10: Gibbs free energy of the wet (dashed), dry (dotted), and deliquescence (solid) branches of coated model (15 nm). The dashed-dotted line represents Gibbs free energy of dry particle in dry model.

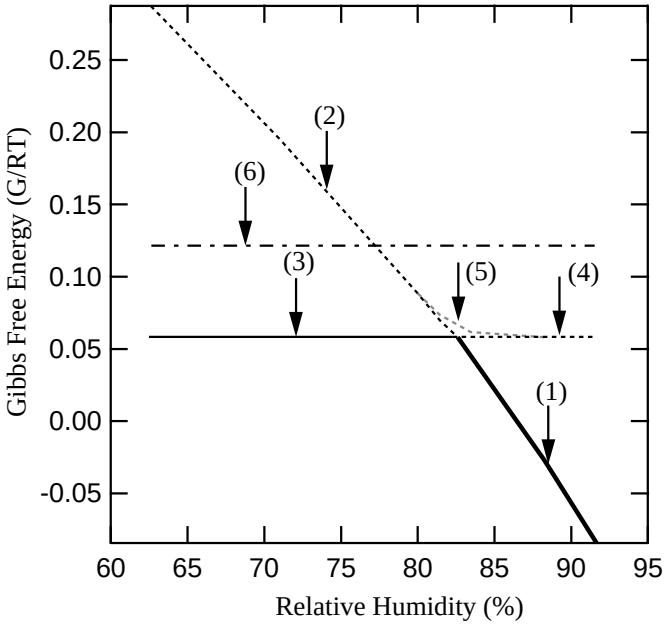

the bulk value at 75%. The increase in deliquescence relative humidity with size decreasing from 100 nm to 15 nm is almost 9% from the initial 75% to 83% relative humidity. For an 5–nm particle, the deliquescence relative humidity increases further to 84%. However, note that at this size the adsorption of three monolayers is predicted before reaching 80% relative humidity, already accounting for a growth factor of approximately 1.2.

For smaller particles and lower growth factors, the uncertainty of the liquid surface tensions are larger, so we have estimated the uncertainty in neglecting this effect with a simple Tolman length approximation (Defay et al., 1966). While clearly not as accurate as more recent models of surface effects in clusters (Girshick and Chiu, 1990; Wilemski, 1995), Fig. 3.13 provides a reasonable bound on the estimated uncertainty with growth factor for these small sizes. The primary effect is that the steepness of the negative slope of the unstable equilibria is increased, although the deliquescence relative humidity changes by only 5%. In general, the higher growth factors ($GF > 1.5$) are insensitive to this problem, although just prior to disappearance of the salt crystal a similar phase ambiguity is encountered when the shrinking crystal is reduced to a finite number (< 100) of "solid" molecules. Figure 3.13 shows schematically the regions of the hygroscopic growth where size–dependent surface tensions may be most important, indicating where the uncertainty of the model is higher.

Figure 3.14 shows that a coated cubic crystal would have a 2% higher deliquescence relative humidity using an estimated surface energy approach (Defay et al., 1966), providing an upper bound on the uncertainty associated with crystal shape effects.

Figure 3.11: Predicted hygroscopic growth curves of NaCl particles at various dry diameters.

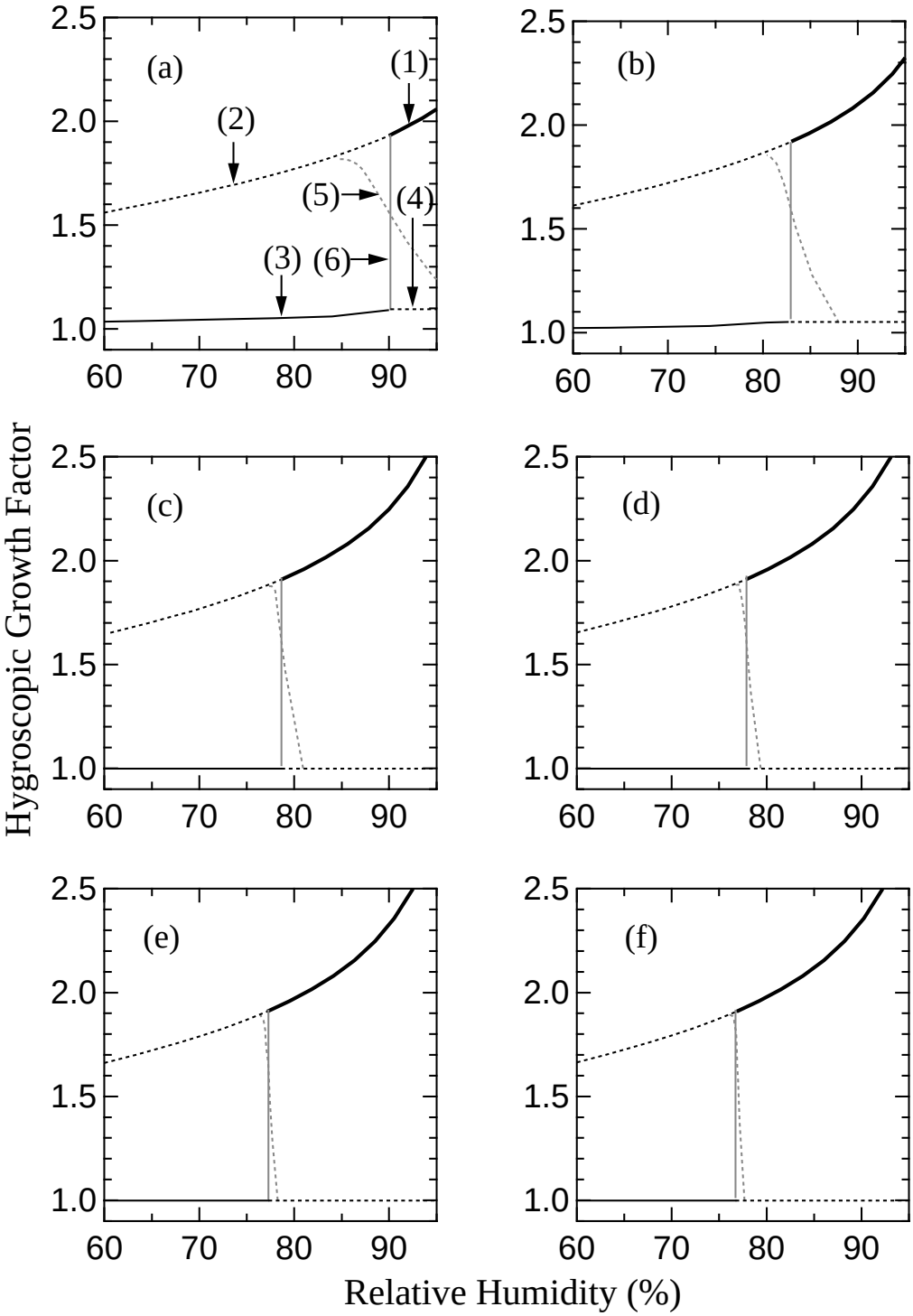

Figure 3.12: Gibbs free energy of NaCl particles at various dry diameters.

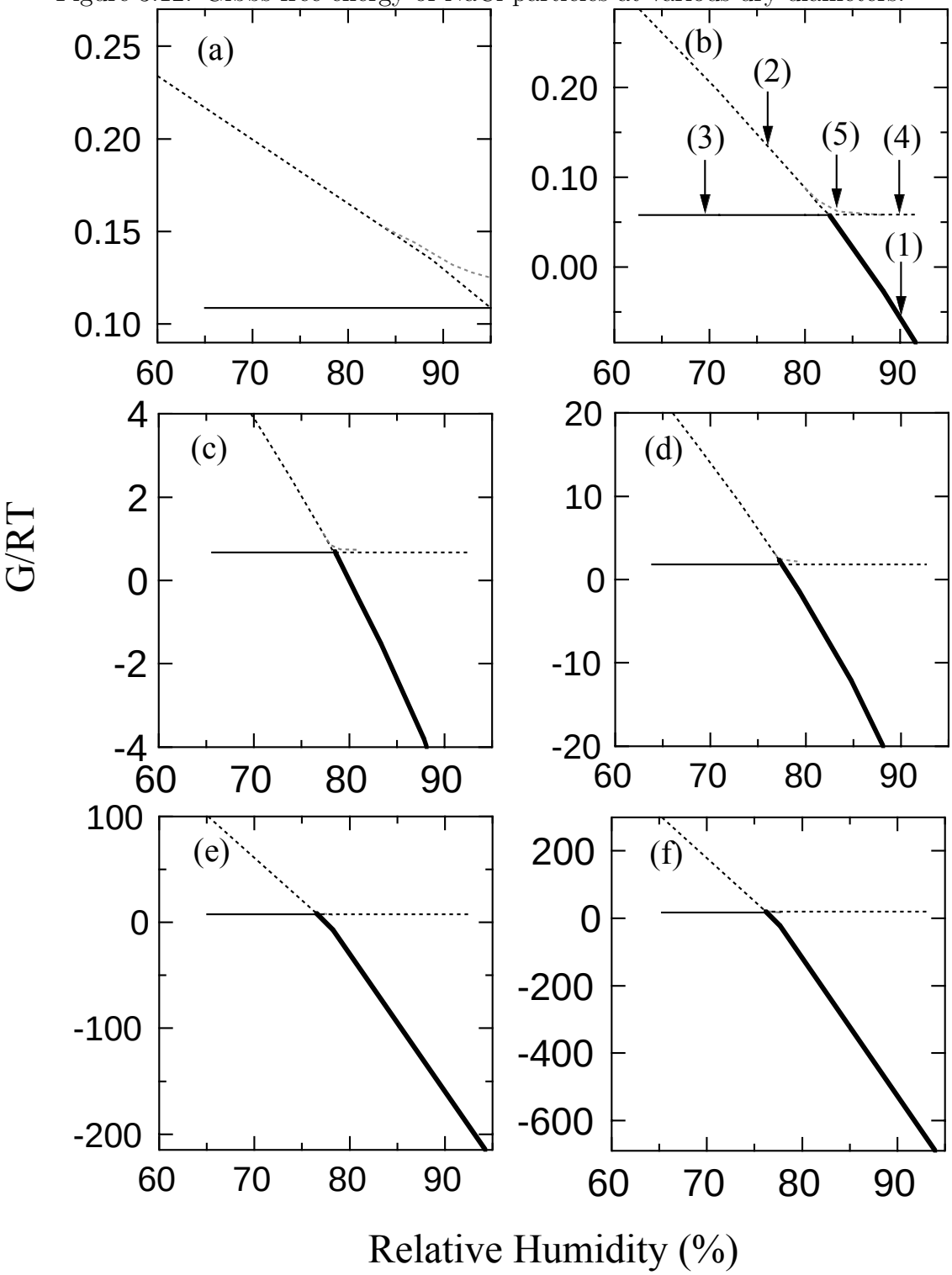

Figure 3.13: Estimated error in predicted hygroscopic growth factor of 15 nm dry diameter NaCl particles for due to size–dependent surface energy artifacts. The coated particle model is shown for (1) constant σ^{LV}= 83 mN m^{-1} and (2) size–dependent surface tension calculated based on Tolman length (Defay et al., 1966).

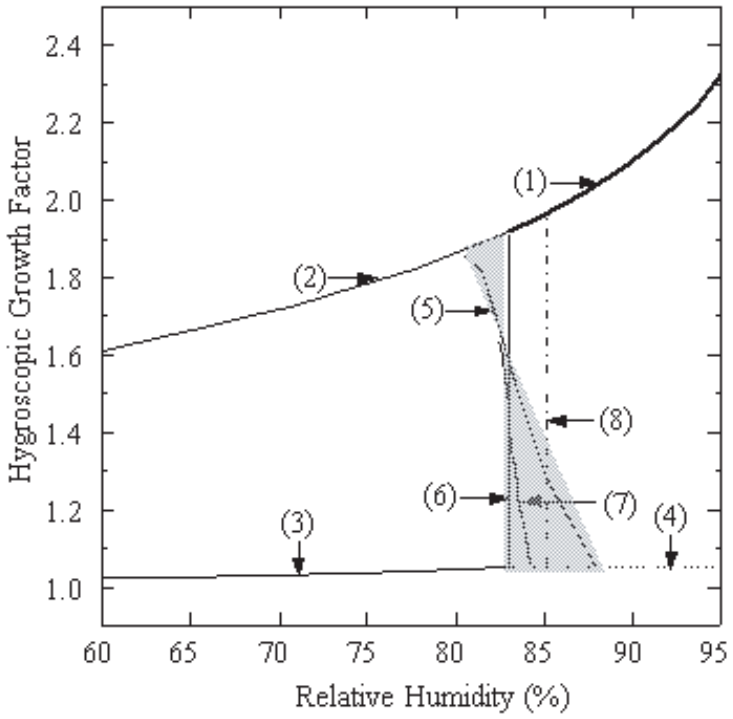

Figure 3.14: Predicted hygroscopic growth factor of 15 nm dry diameter NaCl particles for the coated model with (1) spherical NaCl crystals and (2) cubic NaCl crystals.

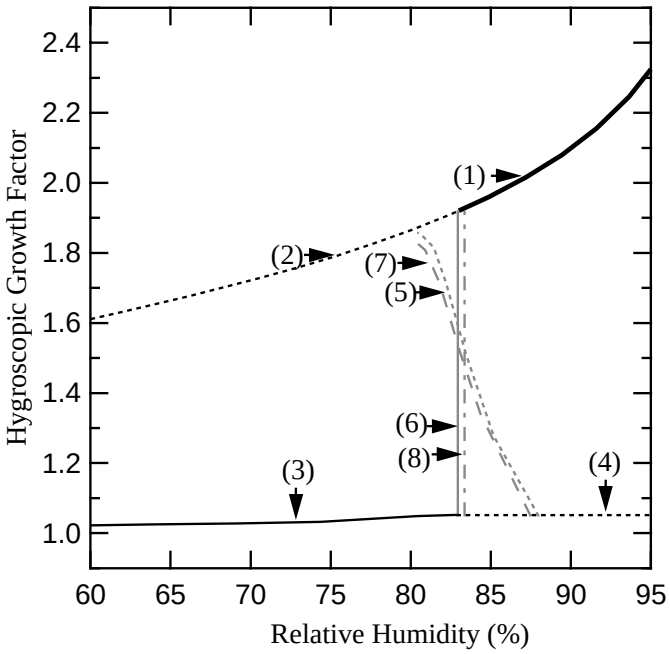

3.5 Growth of $(NH_4)_2SO_4$ and Malonic Acid Particles Small Particles

Both inorganic salts and organic species are expected to exhibit analogous behavior in reaching deliquescence. Exact calculations for many species and mixtures are not possible as the needed solid/liquid, liquid/vapor, or solid/vapor surface tensions have not been measured accurately (Defay et al., 1966; Adamson, 1996). Some information is available for ammonium sulfate and malonic acid (Pruppacher and Klett1997; Tang and Munkelwitz, 1994), so the predicted hygroscopic growth for 15 nm particles, is illustrated in Fig. 3.15. Since σ^{SL} for malonic acid is not well known, we have done the calculation for the range of 20 to 40 mN m^{-1}.The change in deliquescence point from bulk to 15 nm is similar for ammonium sulfate, going from 80% to 88%.

Figure 3.15: Predicted hygroscopic curves of 15 nm sulfate (a) and malonic acid (b). In both panels, dashed lines represent the wet branches. For sulfate, grey dotted line represents unstable equilibrium region using σ^{SL}=29 nN m^{-1}. For malonic acid, 20 (grey dotted line) and 40 nN (grey dashed-dotted line) m^{-1} of σ^{SL} are used. The markers represent data from Tang and Munkelwitz (1994) (circles) and Hämeri et al. (2000) (circles).

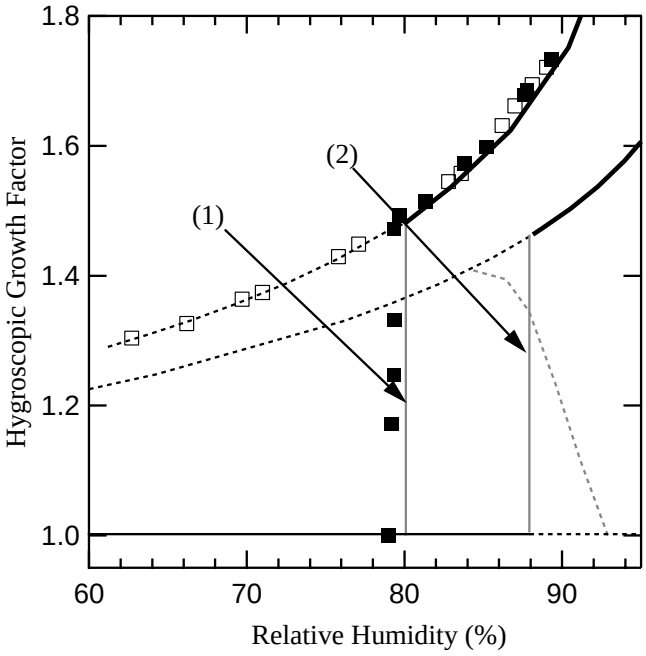

Solubility data are available for malonic acid, but no data on the solid/liquid surface tension were identified. As a result, we have used two different values that are on the low and high end of typical solid/liquid surface tension values. Malonic acid deliquesces at a relative humidity of 76% for bulk solutions, but for 15 nm particles deliquescence occurs at 82% relative humidity for $\sigma^{SL} = 20$ mN m^{-1} or 75% for $\sigma^{SL} = 40$ mN m^{-1}4. In the latter case, the solid/liquid surface tension is sufficiently high that the deliquescence relative humidity actually decreases for a 15 nm dry diameter particle.

In summary, for the three species studied similar increases in deliquescence relative humidity were found, as is illustrated in Fig. 3.16. Between bulk behavior and 5 nm particles, sodium chloride, ammonium sulfate, and malonic acid all increase between 8% and 10% in deliquescence relative humidity. This result (and the well–behaved nature of the relationship) suggests that the behavior is generally true for water–soluble salts.

Since a large part of this phenomenon results from the Kelvin effect increasing the surface energy for forming small particles, this result is expected to be quite general even for those surfaces for which data are not available. An exception to this rule would occur if the surface energy of the solid/liquid interface overwhelmed the energy of the liquid/vapor interface. While some organic species have low liquid/vapor surface tensions, it seems unlikely that they have sufficiently high solid/liquid surface tensions to compensate for the Kelvin effect.

An alternative scenario may arise in the atmosphere for wetting organic species or mixtures which exist in the absence of water as liquids rather than solids in atmospheric conditions. In this case a liquid, non–aqueous core is surrounded by saturated

Figure 3.16: Dependence of predicted deliquescence relative humidities on particle dry diameter for (1) sodium chloride (solid line), (2) ammonium sulfate (short–dashed line), (3) malonic acid with $\sigma^{\mathrm{SL}} = 20$ mN m^{-1} (long–dashed line) and (4) malonic acid with $\sigma^{\mathrm{SL}} = 40$ mN m^{-1}. These calculations are based on the coated model.

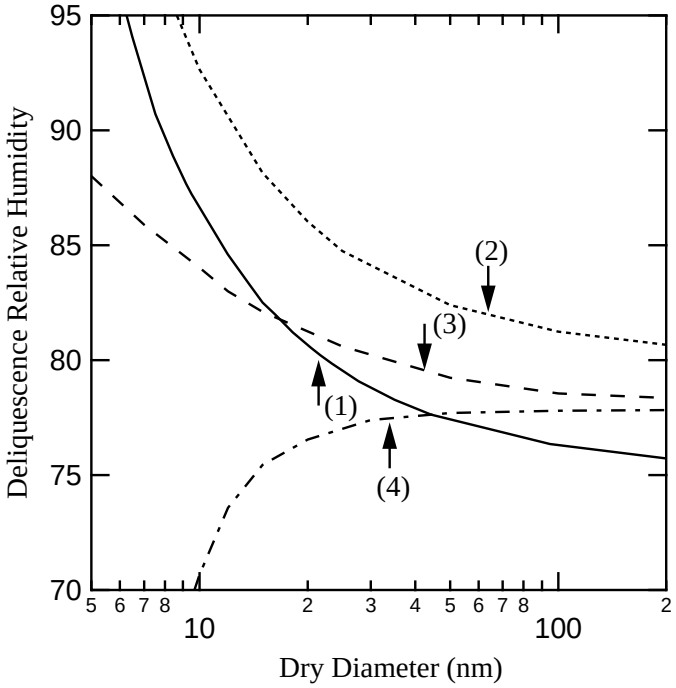

water, so that the relevant interfaces are the liquid/liquid interface between the organic liquid and the aqueous solution, and then the liquid/vapor interface with air. This scenario could result in contradictory behavior, as the organic liquid may coat the aqueous phase rather than vice versa (Cruz and Pandis, 2000).

3.6 Interpretation of Measurements

Recent work by Hämeri et al (2000). provides at least a preliminary opportunity to compare with measurements of this phenomenon. Their data show deliquescence relative humidities of 83% and 87% for dry diameters of 15 and 8 nm in ammonium sulfate particles, comparing well with the predicted values of $81 \pm 3\%$ and $83 \pm 5\%$, both illustrated in Fig. 3.17. However, they measured a few data points intermediate to deliquescence that occur in the range that the model predicts to represent only unstable equilibria. One possible explanation is that the residence time for humidification between the two differential mobility analyzers was insufficient to reach equilibrium with the water vapor. The measured data points might then represent transient values for incompletely grown particles rather than equilibria. Long residence times required for some water vapor equilibria have been noted by investigators with time–varying observations techniques for larger particles (Tang et al., 1986).

Another possibility is that these small ammonium sulfate particles were contaminated by organic species during particle production and analysis. The authors report contamination of less than 1% of the ammonium sulfate bulk solution, but it seems possible that a surface–active contaminant may have been concentrated by the particle formation process as has been observed in other systems (Quinn et al., 1975; Blanchard and Syzdek, 1970). To understand the role that contamination may have

Figure 3.17: Comparison of predicted hygroscopic growth curves with Hameri et al. (2000). Two dry diameters studied are 8 (a) and 15 (b) nm. The solid and dashed lines represent 100% sulfate and 90% sulfate + 10% malonic acid. The grey dotted lines represent unstable equilibria in coated model.

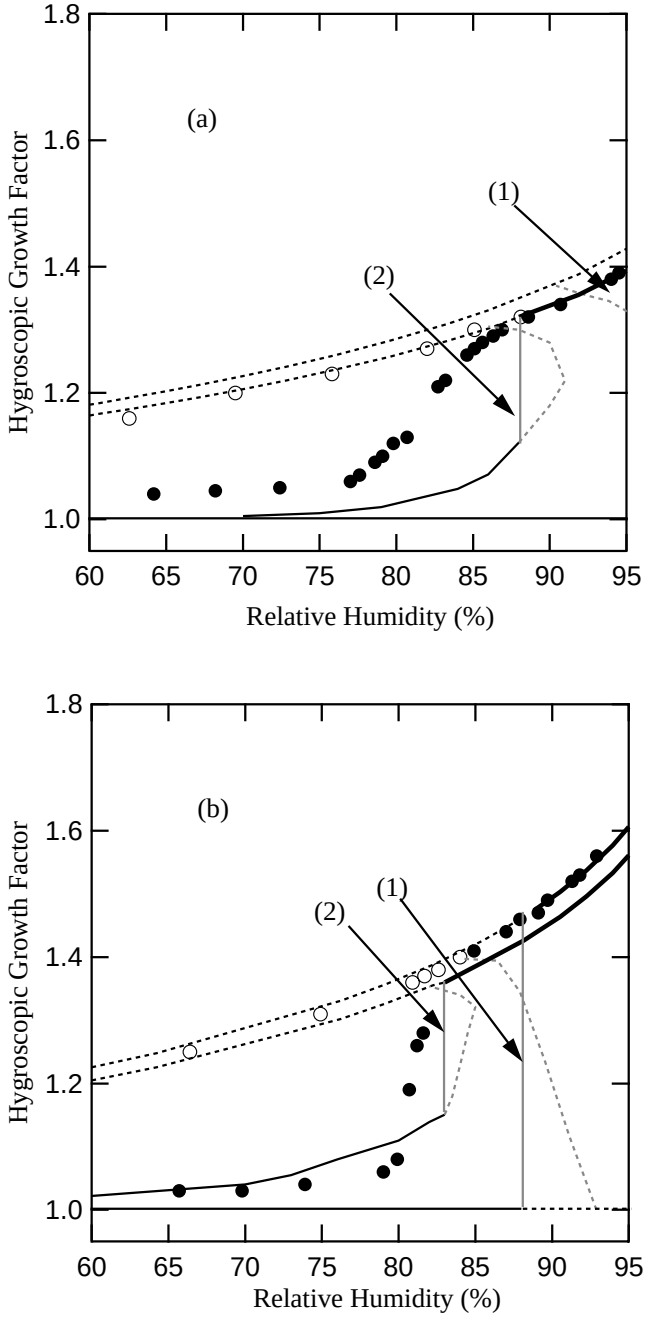

played in these measurements of ammonium sulfate particles, we have shown in Fig. 3.17 the hygroscopic growth for ammonium sulfate with 1% and 10% organic contaminant, where we have used malonic acid to represent a contaminating species. While a 1% organic mixture shows behavior similar in slope to that observed, it is not sufficient to account for the early growth measured. A mixture of ammonium sulfate with 10% malonic acid represents a reasonable approximation of the deliquescence slope, and also matches the measured data better after deliquescence.

Resolving this discrepancy from experiment may be possible. To check if the particles in the deliquescing region have reached stability, it would be possible to add a humidity–controlled flow tube with an increased residence time. If the results vary with residence time, the measured points clearly do not represent stable equilibria. Variation in the relative humidity in the flow tube will also need to be eschewed to preclude anomalous results. Resolving the issue of contamination may be more difficult to resolve, since removing trace organic impurities even in clean laboratory conditions is problematic. Alternatively the composition of semi–volatile species in 15 nm particles could be measured, but since this measurement is not currently possible, it may be difficult to establish the purity of the particles produced.

Despite these uncertainties, hygroscopic growth experiments are capable of measuring stable (and sometimes metastable) equilibria formed when small particles deliquesce. Additional experiments might be able to not only confirm the increase in deliquescence relative humidity with decreasing particle size (even though they are unable to measure transient states in the deliquescing region), but also to allow size–dependent surface tension measurements, by measuring the deliquescence relative humidity of 3–nm particles.

3.7 Conclusions

A more accurate model of the deliquescence of coated particles smaller than 100 nm diameter predicts that the deliquescence relative humidity will increase as particle size is decreased. This approach relies on bulk surface tension values but the trend is independent of the exact values chosen. The result is dependent on the shape of the dry and coated particle and assumes that the particle will have adsorbed water on its surface. These assumptions are appropriate for a range of soluble atmospheric constituents and their mixtures.

Three example systems have been studied here in detail: NaCl, $(NH_4)_2SO_4$, and malonic acid. While the increase in deliquescence point with decreasing particle size is consistent, a dearth of data for the behavior of interfaces for sulfate salts and organic species results in increased uncertainties in those predictions. Hygroscopic growth measurements of ammonium sulfate particles taken by another group (Hämeri et al., 2000) are consistent with the predicted deliquescence relative humidities for 8 and 15 nm particles, but data taken in the deliquescing region cannot be explained. Additional experiments are suggested that may be able not only to resolve these discrepancies and but also to provide a means to measure the size–dependent surface tension of particles as small as 3 nm dry diameter.

References

Abramzon, A.A., and R.D. Gauberk, *Zh. Prek. Khim., 66,*, 1428, 1993.

Adams, P.J., J.H. Seinfeld, and D.M. Koch, Global concentrations of tropospheric sulfate, nitrate, and ammonium aerosol simulated in a general circulation model, *J. Geophys. Res., 104,* 13,791-13,823, 1999.

Adamson, A.W., *Physical Chemistry of Surfaces*, John Wiley, New York, 1990.

Allen, H.C., M.L. Mecartney, and J.C. Hemminger, Minimizing transmission electron microscopy beam damage during the study of surface reactions on sodium chloride, *Microsc. Microanal., 4,* 23-33, 1998.

Barraclough, P.B., and P.G. Hall, Adsorption of water–vapor by lithium-fluoride, sodium-fluoride and sodium-fluoride, *Surface Sci., 46,* 393-417, 1974.

Blanchard, D.C., and L. Syzdek, *Science, 170*, 626, 1970.

Davis, H.T., *Statistical Mechanics of Phases, Interfaces, and Thin Films,* VCH, New York, 1996.

Defay, R., I. Prigogine, and A. Bellemans, *Surface Tension and Adsorption,* Longmans Green, London, 1966.

Espenschied, W.F., E. Matijevic, and M. Kerker, *J. Phys. Chem., 68,*, 2831, 1964.

Estel, J., H. Hoinkes, H. Kaarmann, H. Nahr, and H. Wilsch, Problem of water adsorption on alkali-halide cleavage panes, investigated by secondary ion mass-spectrocopy, *Surface Sci., 54,* 393-418, 1976.

Finlayson–Pitts, B.J., and J.C. Hemminger, Physical chemistry of airborne sea salt particles and their components, *J. Phys. Chem. A, 104,* 11463-11477, 2000.

Fisher, L.R., and J.N. Israelachvili, Direct experimental verification of the Kelvin equation for capillary condensation, *Nature, 277*, 548-549, 1979.

Foster, M.C., and G.E. Ewing, An infrared spectroscopic study of water thin films on NaCl (100), *Surf. Sci., 428*, 102-106, 1999.

Foster, M.C., and G.E. Ewing, Adsorption of water on the NaCl(001) surface. II. An infrared study at ambient temperatures, *J. Chem. Phys., 112*, 6817-6826, 2000.

Ghosal, S., and J.C. Hemminger, Effect of water on the HNO3 pressure dependence of the reaction between gas-phase HNO3 and NaCl surfaces, *J. Phys. Chem.*

A, 103, 4777-4781, 1999.

Girshick, S.L., and C.-P. Chiu, Kinetic nucleation theory: A new expression for the rate of homogeneous nucleation from an ideal supersaturated vapor, *J. Chem. Phys., 93,* 1273-1277, 1990.

Hämeri, K., M. Väkevä, H.C. Hansson, and A. Laaksonen, Hygroscopic growth of ultrafine ammonium sulfate aerosol measured using a ultrafine tandem differential mobility analyzer, *J. Geophys. Res., 105,* 22,231-22,242, 2000.

Lad, R.A., Adsorption of water on sodium chloride – effect of prior exposure to hydrogen chloride carbon dioxide and water vapor, *Surface Sci., 12,*, 37 (1968).

Mirabel, P., H. Reiss, and R.K. Bowles, A theory for the deliquescence of small particles, *J. Chem. Phys., 113,* 8200-8205, 2000.

Peters, S.J., and G.E. Ewing, Thin film water on NaCl(100) under ambient conditions: An infrared study, *Langmuir, 13*, 6345-6348, 1997a.

Peters, S.J., and G.E. Ewing, Water on salt: An infrared study of adsorbed H2O on NaCl(100) under ambient conditions, *J. Phys. Chem. B, 101*, 10,880-10,886, 1997b.

Prenni, A.J., P.J. DeMott, S.M. Kreidenweis, D.E. Sherman, L.M. Russell, and Y. Ming, The effects of low molecular weight dicarboxylic acids on cloud formation, *J. Phys. Chem. A, 105,* 11240-11248, 2001.

Pruppacher, H.R., and J.D. Klett, *Microphysics of Clouds and Precipitation*, Kluwer Acad., Norwell, Mass., 1997.

Quinn, J.A., R.A. Steinbrook, and J.L. Anderson, Breaking bubbles and the water-to-air transport of particulate matter, *Chem. Eng. Sci., 30,* 1177-1184, 1975.

Tang, I.N., H.R. Munkelwitz, and N. Wang, Water activity measurements with single suspended droplets – The NaCl – H_2O and KCl – H_2O systems, *J. Colloid*

Interface Sci., 114, 409-415, 1986.

Tang, I.N., and H.R. Munkelwitz, Aerosol phase transformation and growth in the atmosphere, *J. Appl. Meteorol., 33,* 792-796, 1994.

Wang, Z.L., J.M. Petroski, T.C. Green, and M.A. El–Sayed, Shape transformation and surface melting of cubic and tetrahedral platinum nanocrystals, *J. Phys. Chem. B., 102*, 6145-6151, 1998.

Weis, D.D., and G.E. Ewing, *J. Geophys. Res., 104,* Water content and morphology of sodium chloride aerosol particles, 21275-21285, 1999.

Wilemski, G., The Kelvin equation and self-consistent nucleation theory, *J. Chem. Phys., 103,* 1119-1126, 1995.

Wu, W., and G.H. Nancollas, Determination of interfacial tension from crystallization and dissolution data: a comparison with other methods, *Adv. Colloid Interface Sci., 79,* 229-279, 1999.

Chapter 4

Predicted Hygroscopic Growth of Sea Salt Aerosol

4.1 Chemical Composition of Sea Salt Aerosol

Sodium chloride (NaCl) is the major inorganic component of sea salt particles that are produced at the ocean surface. Both dissolved and particulate organic components in seawater are added to atmospheric aerosol by these same ocean processes. Typically only 10% or less of the total organic particle mass has been resolved into individual species (Rogge et al., 1993). Gas chromatography-mass spectrometry (GC-MS) has provided detailed speciation of insoluble compounds and those water-soluble compounds that can be derivatized (Saxena and Hildemann, 1996). The concentrations of 49 organic compounds in aerosol over the western Atlantic Ocean have been identified, and most of the species that were detected are long-chain insoluble species (Duce et al., 1983). More polar substances, including dicarboxylic and ketocarboxylic acids, have also been identified in marine aerosol in the Pacific Ocean (Kawamura and Gagosian, 1990). Saxena and Hildemann (1996) postulate that a significant part of the unidentified organic aerosol mass consists of water-soluble polar species. Hence, in

addition to ambient measurements of the organic composition of sea salt aerosol our estimate of the complete composition (especially the polar constituents) will include compounds identified in seawater samples (Riley and Chester, 1971).

Measured Sea Salt Particle Organic Composition Single particle measurements of sea salt aerosol suggest that organic species account for 5% to 50% of dry sea salt aerosol mass (Middlebrook et al., 1998). This concentration range is significantly higher than the organic fraction found in seawater, which is typically 0.01% of the total dry components in bulk seawater (most of which is NaCl) (Riley and Chester, 1971). Studies of bubble bursting processes suggest that the formation of surface layers on seawater in which low surface tension species are enhanced may result in higher organic concentrations in the particles that form from bubble bursting (Hoffmann and Duce, 1976). Laboratory work also suggests that even in well-mixed conditions, high molecular weight species may form particles preferentially during the film-breaking process (Quinn et al., 1975). Alternatively, this enhancement of the organic fraction of seawater may result from secondary organic condensation from the vapor phase, in which case, the composition of the organic species will be dependent on local atmospheric sources of biogenic and anthropogenic volatile organic compounds. In this work, we will only treat the simpler case, in which the organic species present in sea salt particles are assumed to be derived from seawater.

Field measurements have reported the carbon number and concentration ranges of long-chain nonpolar compound classes (Gagosian et al., 1981; Gogou et al., 1998). Samples of marine aerosol were collected at Marshall Island in the western equatorial Pacific (11°20′N, 162°20′E) and Crete in the eastern Mediterranean (35°20′N, 25°42′E). Table 4.1 shows that the reported marine aerosol concentrations from different locations share a similar range of carbon number for the compounds identified.

Table 4.1: Direct measurements of sea salt particle chemical composition from Duce et al. (1983) and Gogou et al. (1998).

	Location 1: Island of Crete [a]		Location 2:Marshall Islands	
Compound Type	Carbon Number Range	Total Concentration(ng m^{3})	Carbon Number Range	Total Concentration(ng m^{3})
Aliphaticalkanes	15–40	5.09–35.24	21–36	0.020–0.16
PAHs		0.07-2.0		
n-Alkanals	15–30	0.9–16.85		
Alkanones	10–31	0.4–5.12		
n-Alkanols	12–30	2.74–94.50	13–20	0.060–0.255
Fatty acids and their salts	8–32	24.26–124.30	13–32	0.163–5.051

[a] *Gogou et al. [1998]*

Duce et al. [1983]

Of the 49 organic species identified in direct measurements of sea salt particles, all are long-chain monofunctional compounds that tend to be insoluble (Duce et al., 1983). A small number of multifunctional compounds including diacids have been observed but account for less than $< 2\%$ of the observed organic mass (Kawamura et al., 1996). The majority of aerosol mass that is resolved into separate compound classes consists of alkanes, alkanols and acids. The common carbon number per molecule ranges roughly from 10 to 40 (Gogou et al., 1998). The concentration distribution of each of these compound classes with respect to carbon number generally peaks for compounds with 20 to 30 carbons per molecule with lower concentrations of both longer and shorter carbon chain compounds accounting for smaller mass fractions. The carbon number distribution in the estimated sea salt composition for insoluble compounds is provided in Table 2 from the measurements of Gogou et al. (1998) and Gagosian et al. (1981).

Seawater Organic Composition Of the many organic species present in seawater, only long-chain alkanes, alkanols, and acids have been identified in sea salt aerosol. The identified fraction accounts for less than $< 10\%$ of the organic mass. The remaining fraction is likely to be similar in composition to the soluble compounds found in seawater, since these compound classes are difficult to analyze in ambient aerosol and are unlikely to decompose in aqueous solutions at atmospheric conditions. Consequently, our composite sea salt particle composition relies on seawater analysis for the estimated concentrations of soluble compounds.

Since we are interested in the relative fractions of each organic species that are present in seawater and most organic species are reported on an absolute basis, we need to first estimate the total fraction of organic mass in seawater. The basis for this calculation is the fraction of organic matter that is retained after ultrafiltration, so

that organic matter larger than 0.2 μm is not included. This nonparticulate organic carbon content of ocean waters ranges from 0.3 to 1 mg [C] L^{-1} with the influence of geographical locations, seasons, and biological activities (Menzel and Ryther, 1970). A typical value of 0.65 mg [C] L^{-1} is used here to represent the total organic carbon content of seawater. To convert from organic carbon mass to total organic mass, Turpin and Lim (2001) suggest average factors of 1.3 and 3.2 mg mg [C] $^{-1}$ for water-insoluble and water-soluble compounds, respectively. Benner et al. (1992) report that high molecular weight compounds account for 25% to 35% of total nonparticulate organic mass. Using the average value of 30%, the remaining 70% of the total organic content consists of low molecular weight compounds. The assumptions that low molecular weight compounds are water-soluble and high molecular weight compounds are water-insoluble provide an estimated conversion factor of 2.2 mg mg $[C]^{-1}$ for seawater. The average organic mass in seawater is then $\sim$ 1.4 mg L^{-1}.

Measurements of individual low molecular weight compounds reveal that high concentrations of malic acid (300 μg L^{-1} or 21% of the estimated nonparticulate organic mass) and citric acid (140 μg L^{-1} or 10% of the estimated nonparticulate organic mass) were observed along the Atlantic Coast (Creac'h, 1955). Amino acids were measured to account for 10–25 μg L^{-1} in the Irish Sea (or 1% of the estimated nonparticulate organic mass) (Riley and Segar, 1970). These three types of acids account for $\sim$ 31% of the nonparticulate organic mass, whereas 70% are expected to be low molecular weight compounds. The remaining 39% of low molecular weight compounds are thought to be similar compounds and so are modeled here by assuming that this measured ratio of malic acid to citric acid is appropriate for the entire low molecular weight fraction, such that malic acid is used to represent 48% of the organic mass and citric acid represents 22%.

Of the high molecular weight compounds, only the monosaccharides are soluble. Benner et al. (1992) report soluble carbohydrate concentrations up to 33%, although here we have used a more conservative estimate of 10%. Galactose, xylose, rhamnose, fucose, glucose, mannose, and arabinose have been measured in seawater in many locations around the world (Aluwihare et al., 1997). Since thermodynamic data for most of these sugars are unavailable, we have grouped them in two categories according to their solubility and have modeled each category using the properties of two well-studied sugars, fructose and glucose (Velezmoro and Meirelles, 1998; Peres and Macedo, 1997; Comesana et al., 1999). The very soluble compounds (galactose, rhamnose, mannose, xylose) account for about half of the monosaccharides present (4.7% of the total nonparticulate organic mass) and are represented by fructose because of its similar solubility and low deliquescence point. The slightly less soluble compounds (glucose, fucose, arabinose) account for the other half of the monosaccharides present (4.8% of the total nonparticulate organic mass) and are represented by glucose.

For insoluble compounds the concentration distributions of alkanes, alkanols, and acids are similar in seawater and sea salt particles. The seawater measurements are more complete and provide a better statistical representation of typical composition. The resulting model of sea salt aerosol composition is given in Table 4.1.

4.2 Predicted Hygroscopic Growth of Sea Salt Particles

Particle hygroscopic growth describes water uptake from the vapor phase by soluble substances present in particles. The hygroscopic growth factor (GF) serves as a quantitative description of the amount of water taken up using a ratio of the diameter

Table 4.2: Composite sea salt particle composition estimated from direct measurements of marine aerosol and from seawater composition.

Chain length	Fraction [a]	Compound type	Fraction	Species	Fraction[c]
Low molecular weight [d]	70%	Malic acid	48%	Malic acid	48%
		Citric acid	22%	Citric acid	22%
High molecular weight [d]	30%	Monosaccharides	10%	Glucose	4.8%
				Fructose	4.7%
		Insoluble compounds	20%	C25 Alkane	0.073%
				C27 Alkane	0.15%
				C29 Alkane	0.19%
				C31 Alkane	0.15%
				C33 Alkane	0.073%
				C24 Alkanol	0.065%
				C26 Alkanol	0.28%
				C28 Alkanol	0.44%
				C30 Alkanol	0.28%
				C32 Alkanol	0.065%
				C14 Acid	1.8%
				C15 Acid	4.0%
				C16 Acid	5.2%
				C17 Acid	4.0%
				C18 Acid	1.8%
				C22 Acid	0.23%
				C24 Acid	0.83%
				C26 Acid	1.3%
				C28 Acid	0.83%
				C30 Acid	0.23%

a $\frac{\text{a a o eac olecular ei t}}{\text{otal r anic a}}$

$\frac{\text{a o eac y e}}{\text{otal r anic a}}$

c $\frac{\text{a o eac S ecie}}{\text{otal r anic a}}$

[d]High molecular weight compounds are dened here as having molecular weights larger than 180 amu; low molecular weight compounds have molecular weights smaller than 180 amu.

at ambient humidity ($D_{p,\mathrm{RH}}$) relative to the original dry particle size ($D_{p,\mathrm{dry}}$) and is given by Hämeri et al. (2000) as

$$\mathrm{GF(RH)} = \frac{D_{p,\mathrm{RH}}}{D_{p,\mathrm{dry}}}. \tag{4.1}$$

In hygroscopic growth factor measurements the relative humidity is lowered below the efflorescence point to dry out the particles, and then the humidity is increased to obtain the dependence of particle growth factors as relative humidity increases (Cruz and Pandis, 2000).

To describe this complex mixture, we have made a series of assumptions about sea salt particles based on incomplete data about their composition. In this section we use these simplifications to study this simplified behavior for sea salt particle mixtures in bulk solutions and in particles of different sizes. All of the experimental data used here were measured at 298 K, so the predictions here are only accurate near 298 K because the model does not include parameterizations of the temperature dependence of the solution properties. Section 4.2 evaluates these assumptions, the accuracy of the limited data available, and their importance to our conclusions. These simplifications to describe sea salt particle chemical equilibria are that (1) insoluble species exist in particles as independent solid phases that adsorb a negligible amount of water, (2) secondary inorganic components of seawater (Mg^{2+}, Ca^{2+} and SO_4^{2-}) have negligible interactions with organic species, and (3) insoluble organic compounds in sea salt are represented by the molecular weight and density of the range of alkanes, acids, and alcohols in Table 4.1; soluble organic compounds in sea salt are represented by the molecular weight, density, solubility, activity, and surface tensions of the mixture of malic acid, citric acid, glucose, and fructose given in Table 4.1.

In addition, we assume here that sea salt formation mechanisms are chemically

homogeneous, such that sea salt particles present in the atmosphere are internal mixtures representative of the estimated organic (and inorganic) composition. Few data are available to evaluate this assumption for sea salt, but a comparison of internally mixed and externally mixed aerosol growth is described by Ming and Russell (2001).

Sea Salt Organic Species in Bulk Solutions These assumptions constrain the equilibrium behavior of the mixture, providing a description of the internally mixed behavior of sea salt particles. Organic species provide some additional ions that dissolve below the deliquescence point of sodium chloride but also some insoluble material that does not dissolve at all (even though they may be present in particles that do take up water). The net effect is to create particles that take up more water at lower humidities but less water overall than either a pure sodium chloride or a strictly inorganic seawater solution. In this study, the basis for comparison is taken to be constant dry mass of both soluble and insoluble components (that is, all nonwater mass).

This section considers the case of a bulk quantity of solution, namely, one in which the interfacial energy contribution on a mass basis is negligible because the particle diameter is effectively infinite (and hence the amount of interfacial area relative to the volume of the "particle" is small). In the system studied here, we approach this limit for diameters > 1000 nm.

Sea salt with 30% organic composition

Figure 4.1 shows the hygroscopic growth of the sea salt mixture that includes 30% of the estimated organic composition. The comparison shows differences in water uptake below and above 75% (NaCl deliquescence) compared to inorganic sea salt (with 0% organic composition). Both curves take up water below 75%, although the 30%

Figure 4.1: Predicted hygroscopic growth for bulk solutions of varying organic composition. The compositions studied are (1) 30% organic species and 70% inorganic salts (base case, solid line), (2) a lower organic content case of 10% organic species and 90% inorganic salts (dashed-dotted-dotted line), (3) a higher organic content case of 50% organic species and 50% inorganic salts (dashed line), (4) 100% organic species (dashed-dotted line), (5) 100% inorganic salts found in seawater (thin solid line), and (6) 100% NaCl (thin dotted line).

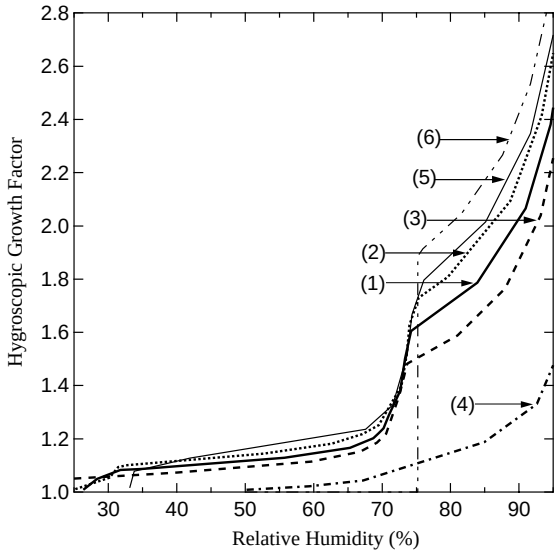

organic case has a higher initial hygroscopic growth since fructose dissolves at 62% relative humidity. In addition, the internal mixture of organic species and inorganic salts takes up more water than the sum of both species independently because of the organic-electrolyte interactions (Andrews and Larson, 1993; Hansson et al., 1998).

At 75% relative humidity the sodium chloride that constitutes the majority of the solute present dissolves resulting in a steeply sloped hygroscopic growth curve. Above this relative humidity the hygroscopic growth is significantly lower than both pure sodium chloride and 15% lower than inorganic seawater because 9% of the dry mass

consists of insoluble organic compounds and 15% consists of the remaining soluble compounds citric acid, glucose, and malic acid. These three soluble compounds dissolve as relative humidity increases, at 84%, 86%, and 87%, respectively. Above this relative humidity only the very insoluble compounds remain undissolved, resulting in lower hygroscopic growth than the strictly inorganic salt composition.

Varied organic composition

Since the fraction of sea salt particles that consists of organic species has not been well characterized by measurements and also will vary with local seawater concentrations, Figure 4.1 also compares the influence of differing fractions (10% and 50%) of the same estimated organic composition to the base case composition of 30% organic. The 10% organic case is within 5% of the hygroscopic growth of the inorganic sea salt composition, so that few differences would be discernible by measurement techniques. The 50% organic case has 25% less growth than the inorganic case.

In this comparison we have kept the relative concentration of each organic species constant. As a consequence, the fraction of organic mass that dissolves at each successive deliquescence point is similar, thus maintaining the shape of the hygroscopic growth curves but shifting them to lower magnitudes as the organic fraction (and hence the insoluble mass) is increased. If the types and relative amounts of organic species are also varied, then the qualitative features of the hygroscopic growth curve also change. The effect of changing the composition of the estimated sea salt organic fraction is discussed in section 4.3.

Sea Salt Particle Size-Dependent Behavior In order to extend the model to the behavior of particles of specific submicron diameters, the interfacial energy terms in (**??**) become important. Figure 4.2 illustrates that for a given composition and

relative humidity, a smaller particle will take up less water than a larger particle. For atmospheric aerosol particles the range of diameters for which this model applies is 5 to 1000 nm. Above 1000 nm the effect of surface tension is negligible for the compositions and relative humidity ranges of interest here. Below 5 nm the size-independent bulk surface tension on which (**??**) relies may not accurately represent the submacroscopic molecular interactions among the finite number of molecules in these clusters (Girshick and Chiu, 1990; Wilemski, 1995).

Particles of 165 nm diameter differ by $< 5\%$ from the bulk solution. Decreasing the diameter to 75 and 50 nm shows additional decreases in hygroscopic growth, but for dry particle sizes of 35 and 15 nm the shape of the curve in the deliquescence region shifts from positively sloped past vertical to negatively sloped. This slope is caused by the surface tension of the liquid/vapor interface competing with the dissolution of NaCl after reaching the solubility limit. The negative slope results in three predicted equilibria for a small range of relative humidities near the deliquescence point, where the third equilibrium is the partially wet particle (and the first two are the dry and wet states).

Deliquescence is predicted to occur when the Gibbs free energy of the wet particle (as given by equation (2.1)) is less than that of the dry particle. For the mixtures studied here, the sodium chloride as well as other species will adsorb water prior to deliquescence such that the dry particle will be coated with a layer of water (Peters and Ewing, 1997a, 1997b; Foster and Ewing, 1999, 2000). Since we have used experimental data from bulk surfaces to describe adsorption onto particles of finite diameters, we have omitted here contributions from the disjoining pressure of the initial aqueous film on the particle surface (Israelachvili, 1996; Adamson, 1990). Preliminary experiments of water adsorption on small particles show that water will

Figure 4.2: Predicted hygroscopic growth of particles with varying dry diameters at organic contents of (a) 10%, (b) 30%, and (c) 50%. The dry diameters shown are (1) bulk case (solid line), (2) 15 nm (dashed line), (3) 35 nm (dashed-dotted-dotted line), (4) 50 nm (thin solid line), (5) 75 nm (thin dashed line), and (6) 165 nm (thin dotted line). For curves with multiple equilibria near deliquescence, shaded lines show the deliquescence path and shaded dotted lines show unstable equilibria.

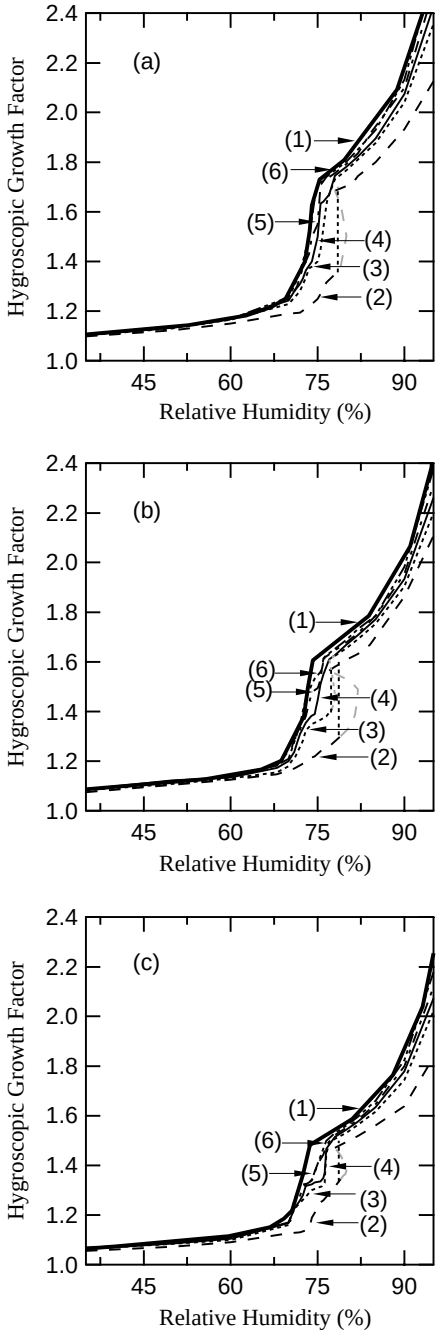

adsorb on particles smaller than 400 nm, but there is some evidence that the amount adsorbed below the deliquescence relative humidity is enhanced over a bulk surface (Weis and Ewing, 1996). Clearly more experimental studies are needed to evaluate this approach.

The straight vertical line for each case in Figure 4.3a shows the relative humidity at which the wet particle free energy drops below the dry. The free energy of the partially wet state is higher than both the wet and dry states at all relative humidities, so this state represents an unstable equilibrium. Since the mixtures here include compounds (e.g., magnesium sulfate) which take up water below 70% relative humidity, the "dry" state will include some water associated with components other than NaCl. For example, for 15 nm sea salt particles with 10% organic composition, deliquescence occurs at 78% relative humidity when the free energy of the wet particle has decreased to $3.50 \times 10^{-20} \times RT$, which is just below the free energy of the dry particle at $3.56 \times 10^{-20} \times RT$ (at lower relative humidities, the free energy of the wet particle is higher than the dry particle). At this relative humidity the free energy of the partially wet particle is $3.65 \times 10^{-20} \times RT$, so that it is less stable than both dry and wet states. Russell and Ming (2001) discuss the stability of these partially wet states in detail, as well as the sensitivity of this result to the value of the solid/liquid surface tension. For the sea salt mixtures described here, in the absence of data for solid/liquid surface tensions for other species, the solid/liquid interface is approximated by measured values for NaCl ($\sigma^{\mathrm{SL}} = 29$ mN m^{-1}) and the liquid/vapor interface is calculated as a mixture of saturated NaCl solution ($\sigma^{\mathrm{LV}} = 83$ mN m^{-1}) with contributions from dissolved organic species calculated as described in section **??**.

The same trends are seen in all of the particle sizes shown, including a jump in water uptake that occurs in each curve when the remaining NaCl dissolves as the

relative humidity reaches 75%. Outside of the relative humidities near the deliquescence region in which rapid growth occurs, the hygroscopic growth decreases almost linearly with dry particle sizes between 165 and 15 nm.

Comparison to Measured Hygroscopic Growth of Ambient Particles Berg et al. (1998), Swietlicki et al. (2000), and Zhou et al. (2001) have measured the hygroscopic growth of ambient particles in marine environments in the Southern Ocean, the northeastern Atlantic Ocean, and the Arctic Ocean, respectively. Their results are consistent with the presence of two or more types of particles, one of which was frequently similar in growth characteristics to sea salt. Another particle type that appeared frequently (classified in the above studies as "less hygroscopic") seemed to have low water uptake properties that would be similar to particles that were primarily composed of organic species. Their measured hygroscopic growth factors for particles of 15, 35, 50, 75, and 165 nm in diameter are illustrated in Figure 4.3.

Figure 4.3b shows that for 35-nm-diameter measurements the particle classes identified as "sea salt" had hygroscopic growth properties similar to inorganic sea salt mixed with between 10% and 30% organics. The Arctic Ocean results are almost identical to the 30% organic case, while the northeastern Atlantic Ocean sea salt particles measured during ACE2 have $< 10\%$ organic compounds and are only slightly less hygroscopic than is predicted for pure inorganic sea salt (with 0% organics). For 50-nm particles in Figure 4.3c and 75 nm particles in Figure 4.3d the 10% organic case provides a good prediction of the hygroscopic growth, but the 165-nm case in Figure 4.3e has a lower hygroscopic growth that compares better with the growth for $\sim 20\%$ organic compounds. The error bars show that the reported uncertainty in the measurement is comparable to the difference between the 10% and 30% organic cases, limiting our ability to draw more specific conclusions. An alternative interpretation

Figure 4.3: Predicted hygroscopic growth of particles with varying organic contents at a range of particle sizes. The sizes shown are (a) 15 nm, (b) 35 nm, (c) 50 nm, (d) 75 nm, and (e) 165 nm. The compositions shown are (1) 30% organic species and 70% inorganic salts (base case, solid line), (2) a lower organic content case of 10% organic species and 90% inorganic salts (dashed-dotted-dotted line), (3) a higher organic content case of 50% organic species and 50% inorganic salts (dashed line), and (4) a 100% organic content case (dashed-dotted line). For curves with multiple equilibria near deliquescence in Figures 4.3a and 4.3b, shaded lines show the deliquescence path and shaded dotted lines show unstable equilibria. In addition, the plot illustrates recent measurements of ambient particle growth from field project data reported by Berg et al. (1998) (ACE1, triangles), Swietlicki et al. (2000) (ACE2, circles), and Zhou et al. (2001) (AOE, squares). The particles were grouped by those authors as particles similar to sea salt (solid symbols), particles that are more hygroscopic than sulfate (shaded symbols), and particles that are less hygroscopic than sulfate (open symbols). The error bars on the symbols indicate the standard deviation for each category during the project.

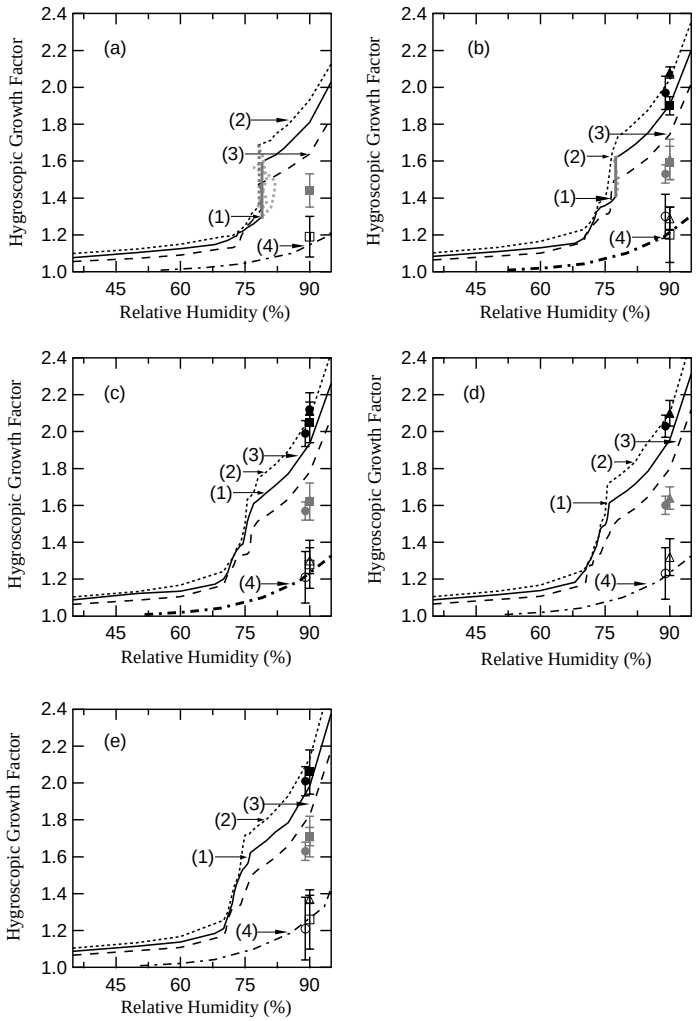

is that some non-sea-salt sulfate was also present that would reduce the hygroscopic growth. Since particle composition measurements associated with each of these particle types are not available, this comparison serves only to highlight the consistency of the measurements with sea salt particles containing organic species.

In addition, the northeastern Atlantic Ocean and Arctic Ocean samples that included the particle type identified as "less hygroscopic" (Swietlicki et al., 2000; Zhou et al., 2001) are consistent with a 100% mixture of the estimated sea salt organic composition (with no inorganic ions present). While there are certainly infinite combinations of organic species that yield similar hygroscopic behavior, this result does suggest that this type of particle is consistent with ocean-derived organic particles that have little or no inorganic salts present.

The hygroscopic growth measurements also frequently reported a "more hygroscopic" category of observed particle growth. The "more hygroscopic" type particles are likely to include a significant fraction of ammonium sulfate based on the presence of both ammonium and sulfate ions in associated bulk filter measurements (Quinn et al., 1998; 2000). Nonetheless, these calculations indicate that the hygroscopic growth measured would also be consistent with a mixture of sea salt with $\sim$ 50% marine organic species. The variability indicated by the bounds of the whiskers on the measured hygroscopic growth values shows that there was a significant standard deviation in the hygroscopicities of the particles measured in each field project. This variability suggests that different compositions of particles were found on different days.

4.3 Model Uncertainties

Testing the model sensitivity to assumptions and its uncertainties with experimental data challenges the robustness of our conclusions. We have calculated the equilibria predicted when each of our assumptions is relaxed. This approach includes the neglect of interactions of secondary inorganic ions with organic species, the estimated organic composition, the presumed internal mixing of sea salt particle components, and the phase state of nonaqueous components. In addition, we have estimated the model error propagated by the experimental errors in data used to make our empirical parameterizations. This calculation serves to provide an indication of the most productive directions for reducing the uncertainties in the hygroscopic growth.

Sensitivity to Nonaqueous Particle Phases To facilitate the search for the minimum free energy configuration that satisfies equation (**??**), it is convenient to constrain the components or parts of components that do not dissolve into separate solid or liquid phase as determined by their pure component properties. Since excess properties are not additive, the assumption does not hold for combinations of organic solids that can form liquids because the mixture melting point is lower than any of the melting points of the individual solids (Peters et al., 2000). Relaxing this assumption showed that the insoluble organic mixture described in Table 4.1 will form a nonaqueous phase liquid (NAPL) and that this configuration results in a lower Gibbs free energy for the system, as illustrated in Figure 4.4.

The hygroscopic growth properties of the particles that include NAPL states are identical to the configuration with solid organic species since neither the solids nor the NAPL components take up water. Small changes are predicted for the particle density and surface interactions, although these considerations are arguably more dependent on the morphology and mixing homogeneity (which have not been considered here).

Figure 4.4: Gibbs free energy of system phase equilibrium for individual solid phases for undissolved component (dashed line) and for a nonaqueous phase liquid mixture of undissolved organic species (solid line).

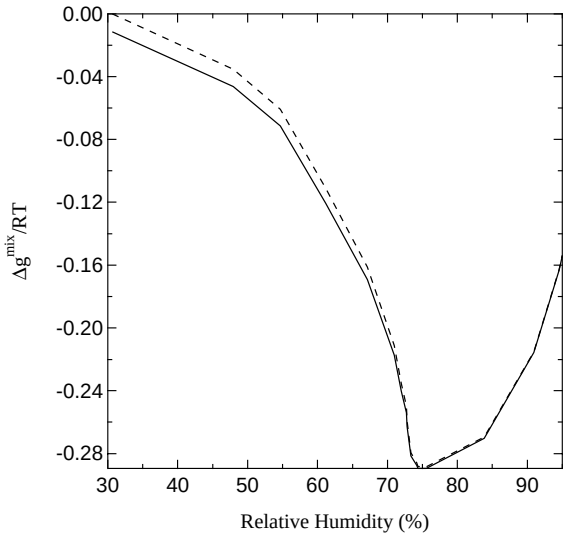

Sensitivity to Secondary Inorganic Ion Interactions With Organic Species

Including the electrolyte-organic interactions following the approach of Xie et al. (1997) requires experimental data for the activity coefficients of the electrolyte with a range of organic compounds, as discussed by Ming and Russell (2001). Since these data are not currently available for the secondary inorganic ions present in seawater (namely, Mg^{2+}, Ca^{2+}, and SO_4^{2-} ions), the organic-electrolyte interactions for these species have been neglected in the preceding hygroscopic growth calculations. We have estimated the magnitude of the error incurred by this assumption by comparing the growth factors with (1) no organic-electrolyte interactions for Mg^{2+}, Ca^{2+}, and SO_4^{2-} ions or (2) treating each Mg^{2+}, Ca^{2+}, and SO_4^{2-} ion as two additional Na^+ or Cl^- ions. The latter scenario considers a "worst-case" scenario in which the "salting out" effect of sulfate ions are double that of each chloride ion. Figure 4.5 shows that because sulfate accounts for only 3.5% of the inorganic salt mass there is less than a

Figure 4.5: Effect of organic-electrolyte interactions for secondary inorganic ions (Mg^{2+}, SO_4^{2-}, and Ca^{2+}) on hygroscopic growth. The hygroscopic growth for the base case composition (30% organics and 70% inorganic salts) was calculated assuming (1) that these secondary ions had no interactions with organic species (solid line) and (2) that each secondary inorganic ion had twice the "salting-out" effect of Na^+ or Cl^- (dashed line).

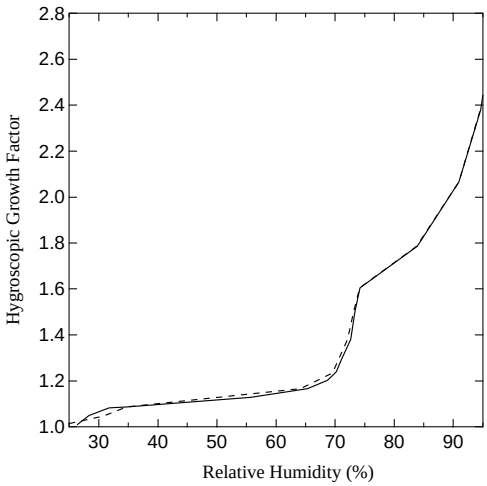

2% difference between the two assumptions in the deliquescence region and negligible differences elsewhere.

Even though these secondary inorganic ions account for $\sim 15\%$ of the total ions in sea salt, the interactions of these ions with different classes of organic compounds has only a small effect on the predicted growth according to the bounding scenarios investigated here. These results suggest that these additional interactions have a negligible impact on hygroscopic growth (unless their organic interactions are significantly stronger than the model Na^+ and Cl^- ions), although major distinctions will occur in the deliquescence region.

Sensitivity to Estimated Organic Composition The limited availability of

data on the behavior of soluble and slightly soluble organic components has resulted in the simplified description of those components given in Table 4.1. While we cannot study the possible role of specific species whose thermodynamic behavior has not been characterized, we can compare the behavior of the components for which we do have data. In order to better illustrate differences from the base case behavior, we have omitted Mg^{2+} for this comparison.

The insoluble organic species are described as a detailed mixture of 20 species, but since they do not dissolve in the aqueous phase, their only role in particle properties is in how they contribute to the particle density and surface interactions. The surface properties will also rely heavily on individual particle morphologies. Figure 4.6a shows the difference between the estimated organic composition and a mixture of all-insoluble organic species. Removing the soluble organic species entirely reduces the hygroscopic growth by 10%.

The soluble species can also have very different influences on the hygroscopic growth, since the more soluble components deliquesce at lower relative humidities. In addition, the smaller organic ion species will take up more water on a mass basis. Figures 4.6b and 4.6c show the effect of replacing the mixture of soluble organic species with each of the four pure soluble components. A clear distinction appears below 70% relative humidity when fructose is removed, since no other species dissolves below 50%. In Figure 4.6b, at 70% the glucose dissolves and above 72% relative humidity the behavior of both the pure glucose and the pure fructose cases becomes indistinguishable from the base case organic mixture. Small differences can also be seen when malic acid or citric acid are considered in Fig. 4.6c, since neither dissolves before NaCl deliquesces.

Figure 4.6: Sensitivity of predicted hygroscopic growth to different organic species for (a) insoluble organic components, (b) sugars, and (c) organic acids. Base case of (1) 30% organics and 70% inorganic salts (solid line) is compared to an all-insoluble case with (2) 30% insoluble organics and 70% inorganic salts (dotted line) (Figure 4.6a); an all-glucose case with (3) 24% glucose, 6% insoluble organics, and 70% inorganic salts (dotted line) and an all-fructose case with (4) 24% fructose, 6% insoluble organics, and 70% inorganic salts (dashed line) (Figure 4.6b); and an all-malic acid case with (5) 24% malic acid, 6% insoluble organics, and 70% inorganic salts (dotted line) and an all-citric acid case with (6) 24% citric acid, 6% insoluble organics, and 70% inorganic salts (dashed line) (Figure 4.6c).

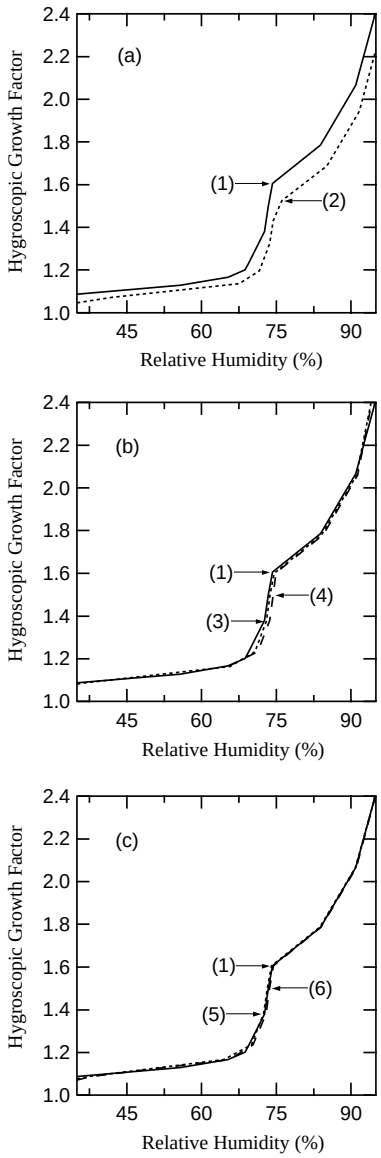

Sensitivity to Empirical Correlations All of the chemical activities and interfacial energies in equation (**??**) for pure components and their mixtures are derived from measurements in which experimental uncertainties are inherent. Since such errors can propagate in a calculation as complex as the one described here, we have varied individual empirical parameters in order to quantify the aggregate uncertainty in the model. While this calculation does not span the entire range of parameter space, it provides appropriate bounds on the uncertainties and some idea of the critical measurements required to improve model accuracy.

The experimental data are correlated in the model to estimate interaction parameters for each of the types of compounds described in the model. The five types of interactions needed to describe organic mixtures in sea salt are (1) interactions between multifunctional groups and water, (2) interactions between sugars and water, (3) interactions between carboxylic acids and water, (4) interactions between sugars and electrolytes, and (5) interactions between carboxylic acids and electrolytes. Table 4.3 summarizes these sensitivity studies: each sensitivity test was conducted by running the model with the extreme high and low values of the reported experimental data in the references given. Since the model is more sensitive at humidities near the deliquescence point, each calculation has been done at both a low relative humidity near deliquescence (73%) and a higher relative humidity (84%). The resulting changes in predicted hygroscopic growth are described by the percentage change in relative humidity. The estimated experimental uncertainties are within 5% change in the predicted equilibrium relative humidity. The so-called "salting out" effect between carboxylic acids and electrolytes can change the fraction of ions dissolved by up to 20%, resulting in up to a 4.2% difference in the equilibrium relative humidity at 73% relative humidity or up to a 1.6% difference at 84% relative humidity.

Table 4.3: Sensitivity of model predictions to experimental uncertainty in data used to correlate empirical parameters.

Correlated parameter	Reference	Uncertainty of experimental measurements	Sensitivity of predicted RH at	
			73%	84%
Interaction parameters between CH_n and H_2O in multifunctional compounds	*Mertl*, 1972	±0.1% (mole fraction)	±1.0%	±0.6%
Interaction parameters between sugars and H_2O	*Peres and Macedo*, 1996	±0.44% (RH)	±3.4%	±1.0%
Interaction parameters between acids and H_2O	*Velezmoro et al.*, 1998	±0.15% (RH)	±2.9%	±1.0%
Interaction parameters between acids and H_2O	*Apelblat et al.*, 1995	±4% (RH)	±1.6%	±1.1%
Interaction parameters between sugars and ions	*Comesana et al.*, 1999	±0.5% (RH)	±3.1%	±1.0%
Interaction parameters between acids and ions	*Herz and Hiebenthal*, 1929	±20% (mol L^{-1})	±4.2%	±1.4%

4.4 Conclusions

For the seawater organic species studied here, the presence of only 30% organic species in atmospheric particles at relative humidities higher than 50% reduces the predicted hygroscopic growth for an equilibrium internal mixture by 15% from the growth predicted for purely inorganic sea salt. Organic mass fractions of 50% or higher reduce growth by 25% compared to inorganic sea salt or eliminate water uptake entirely in subsaturated conditions. This effect may have important implications for particle behavior used for calculating global aerosol optical depths, since the magnitude is comparable to the inorganic composition differences studied by Adams et al. (1999). Comparison to ambient hygroscopic growth factor measurements suggests that organic fractions of 10% to 30% are consistent with measured hygroscopic growth of ambient particles.

Significant uncertainties remain in the identification of the exact speciated composition of organic particles of marine origin. In addition, the behavior of the majority of existing organic species are not well characterized in complex mixtures with electrolytes in water. The sensitivity studies suggest that while the magnitude of the effect will vary with the exact speciated composition, the largest uncertainty lies in identifying the fraction of organic mass in the particle and the proportion of that organic mass that is soluble, slightly soluble, or insoluble.

References

Abrams, D.S., and J.M. Prausnitz, Statistical thermodynamics of liquid mixtures: A new expression for the excess Gibbs energy of partly or completely miscible systems, *AIChE J., 21,* 116-128, 1975.

Adams, P.J., J.H. Seinfeld, and D.M. Koch, Global concentrations of tropospheric sulfate, nitrate, and ammonium aerosol simulated in a general circulation model, *J. Geophys. Res., 104,* 13,791-13,823, 1999.

Adamson, A.W., *Physical Chemistry of Surfaces*, John Wiley, New York, 1990.

Aluwihare, L.I., D.J. Repeta, and R.F. Chen, A major biopolymeric component to dissolved organic carbon in surface seawater, *Nature, 387,* 166-169, 1997.

Andrews, E., and S.M. Larson, Effect of surfactant layers on the size changes of aerosol-particles as a function of relative-humidity, *Environ. Sci. Technol., 27,* 857-865, 1993.

Apelblat, A., M. Dov, J. Wisniak, and J. Zabicky, The vapour pressure of water over saturated aqueous solutions of malic, tartaric, and citric acids, at temperatures from 288 K to 323 K, *J. Chem. Thermodyn., 27,* 35-41, 1995.

Benner, R., J.D. Pakulski, M. McCarthy, J.I. Hedges, and P.G. Hatcher, Bulk chemical characteristics of dissolved organic-matter in the ocean, *Science, 255,* 1561-1564, 1992.

Berg, O.H., E. Swietlicki, and R. Krejci, Hygroscopic growth of aerosol particles in the marine boundary layer over the Pacific and Southern Oceans during the First Aerosol Characterization Experiment (ACE 1), *J. Geophys. Res., 103,* 16,535-16,545, 1998.

Blanchard, D.C., Sea-to-air transport of surface active material, *Science, 146,* 396-397, 1964.

Blanchard, D.C., The production, distribution, and bacterial enrichment of sea-salt aerosol, in *Air-Sea Exchange of Gases and Particles*, pp. 407-454, D. Reidel, Norwell, Mass., 1983.

Clegg, S.L., K.S. Pitzer, and P. Brimblecombe, Thermodynamics of multicomponent, miscible, ionic-solutions, 2, mixtures including unsymmetrical electrolytes, *J. Phys. Chem., 96,* 9470-9479, 1992. (Correction, *J. Phys. Chem., 98,* 1368, 1994, and Correction, *J. Phys. Chem., 99*, 6755, 1995.)

Clegg, S.L., P. Brimblecombe, and A.S. Wexler, Thermodynamic model of the system H^+-NH_4^+-SO_4^{2-}-NO_3^--H_2O at tropospheric temperatures, *J. Phys. Chem. A, 102,* 2137-2154, 1998.

Clegg, S.L., J.H. Seinfeld, and P. Brimblecombe, Thermodynamic modelling of aqueous aerosols containing electrolytes and dissolved organic compounds, *J. Aerosol Sci., 32,* 713-738, 2001.

Comesana, J.F., A. Correa, and K. Sereno, Measurements of water activity in "sugar" plus sodium chloride plus water systems at 25 C, *J. Chem. Eng. Data, 44,* 1132-1134, 1999.

Creac'h, P.V., Presence of citric and malic acids in littoral marine waters, *Hebd. Seances Acad. Sci., 240,* 2551-2553, 1955.

Cruz, C.N., and S.N. Pandis, Deliquesence and hygroscopic growth of mixed inorganic-organic atmospheric aerosol, *Environ. Sci. Technol., 34,* 4313-4319, 2000.

Duce, R.A., V.A. Mohnen, P.R. Zimmerman, D. Grosjean, W. Cautreels, R. Chatfield, R. Jaenicke, J.A. Ogren, E. D. Pellizzari, and G.T. Wallace, Organic material in the global troposphere, *Rev. Geophys., 21,* 921-952, 1983.

Foster, M., and G.E. Ewing, An infrared spectroscopic study of water thin films on NaCl (100), *Surf. Sci., 428*, 102-106, 1999.

Foster, M.C., and G.E. Ewing, Adsorption of water on the NaCl(001) surface. II. An infrared study at ambient temperatures, *J. Chem. Phys., 112*, 6817-6826, 2000.

Fredenslund, A., J. Gmehling, and P. Rasmussen, *Vapor-Liquid Equilibrium Using*

UNIFAC, Elsevier Sci., New York, 1977.

Freier, R.K., *Aqueous Solutions: Data for Inorganic and Organic Compounds*, W. de Gruyter, New York, 1976.

Gagosian, R.B., E.T. Peltzer, and O.C. Zafiriou, Atmospheric transport of continentally derived lipids to the tropical North Pacific, *Nature, 291,* 312-315, 1981.

Girshick, S.L., and C.-P. Chiu, Kinetic nucleation theory: A new expression for the rate of homogeneous nucleation from an ideal supersaturated vapor, *J. Chem. Phys., 93,* 1273-1277, 1990.

Gmehling, J., From UNIFAC to modified UNIFAC to PSRK with the help of DDB, *Fluid Phase Equilibr., 107,* 1-29, 1995.

Gmehling J., P. Rasmussen, and A. Fredenslund, Vapor-liquid equilibria by UNIFAC group contribution: Revision and extension, 2, *Ind. Eng. Chem. Process Des. Dev., 21,* 118-127, 1982.

Gogou, A.I., M. Apostolaki, and E.G. Stephanou, Determination of organic molecular markers in marine aerosols and sediments: One-step flash chromatography compound class fractionation and capillary gas chromatographic analysis, *J. Chromatogr. A, 799,* 215-231, 1998.

Hämeri, K., M. Väkevä, H.C. Hansson, and A. Laaksonen, Hygroscopic growth of ultrafine ammonium sulfate aerosol measured using a ultrafine tandem differential mobility analyzer, *J. Geophys. Res., 105,* 22,231-22,242, 2000.

Hansson, H.C., M.J. Rood, S. Koloutsou-Vakakis, K. Hämeri, D. Orsini, and A. Wiedensohler, NaCl aerosol particle hygroscopicity dependence on mixing with organic compounds, *J. Atmos. Chem., 31,* 321-346, 1998.

Haywood, J.M., and V. Ramaswamy, Global sensitivity studies of the direct radiative forcing due to anthropogenic sulfate and black carbon aerosols, *J. Geophys.*

Res., 103, 6043-6058, 1998.

Haywood, J.M., V. Ramaswamy, and B.J.Soden, Tropospheric aerosol climate forcing in clear-sky satellite observations over the oceans, *Science, 283,* 1299-1303, 1999.

Herz, W., and F. Hiebenthal, Über Löslichkeitsbeeinflussungen, *Z. Anorg. Allg. Chem., 177,* 363-380, 1929.

Hoffman, E.J., and R.A. Duce, Factors influencing the organic carbon content of marine aerosol: A laboratory study, *J. Geophys. Res., 81,* 3667-3670, 1976.

Israelachvili, J.N., *Intermolecular and Surface Forces,* Academic, San Diego, Calif., 1996.

Kawamura, K., and R.B. Gagosian, Midchain ketocarboxylic acids in the remote marine atmosphere: Distribution patterns and possible formation mechanisms, *J. Atmos. Chem., 11,* 107-122, 1990.

Kawamura K, R. Semere, Y. Imai, Y. Fujii, and M. Hayashi, Water soluble dicarboxylic acids and related compounds in Antarctic aerosols, *J. Geophys. Res., 101,* 18,721-18,728, 1996.

Kojima, K., S.J. Zhang, and T. Hiaki, Measuring methods of infinite dilution activity coefficients and a database for systems including water, *Fluid Phase Equilibr., 131,* 145-179, 1997.

Li, J.D., H.M. Polka, and J. Gmehling, A G(E) model for single and mixed-solvent electrolyte system, 1, Model and results for strong electrolytes, *Fluid Phase Equilibr., 94,* 89-114, 1994.

Li, Z.B., Y.G. Li, and J.F. Lu, Surface tension model for concentrated electrolyte aqueous solutions by the Pitzer equation, *Ind. Eng. Chem. Res., 38,* 1133-1139, 1999.

Li, Z.D., A.L. Williams, and M.J. Rood, Influence of soluble surfactant properties on the activation of aerosol particles containing inorganic solute, *J. Atmos. Sci., 55,* 1859-1866, 1998.

Lyman, W.J., W.F. Reehl, and D.H. Rosenblatt, *Handbook of Chemical Property Estimation Methods: Environmental Behavior of Organic Compounds*, Am. Chem. Soc., Washington, D.C., 1990.

Menzel, D.W., and J.H. Ryther, Distribution and cycling of organic matter in the oceans, in *Symposium on Organic Matter in Natural Waters*, edited by D. W. Hood, Inst. of Mar. Sci., pp. 31-54, Univ. of Alaska, Fairbanks, 1970.

Mertl, I., Liquid-vapor equilibrium 50. Prediction of multicomponent vapor-liquid equilibria from binary parameters in systems with limited miscibility, *Collect. Czech. Chem. Commun., 37,* 375-411, 1972.

Michalewicz, Z., and G. Nazhiyath, Genocop III: A co-evolutionary algorithm for numerical optimization problems with nonlinear constraints, in *Proc. 2nd IEEE International Conference on Evolutionary Computation, Perth, 2,* pp. 647-651, Inst. of Electr. and Electr. Eng., New York, 1995.

Middlebrook, A.M., D.M. Murphy, and D.S. Thomson, Observations of organic material in individual marine particles at Cape Grim during the First Aerosol Characterization Experiment (ACE 1), *J. Geophys. Res., 103,* 16,475-16,483, 1998.

Ming, Y., and L.M. Russell, Thermodynamic equilibrium of aqueous solutions of organic-electrolyte mixtures in aerosol particles, *AIChE J.*, submitted, 2001.

Mirabel, P., H. Reiss, and R.K. Bowles, A theory for the deliquescence of small particles, *J. Chem. Phys., 113,* 8200-8205, 2000.

Nath, S., Surface tension of nonideal binary liquid mixtures as a function of composition, *J. Colloid Interface Sci., 209,* 116-122, 1999.

Peres, A.M., and E.A. Macedo, A modified UNIFAC model for the calculation of thermodynamic properties of aqueous and non-aqueous solutions containing sugars, *Fluid Phase Equilibr., 139,* 47-74, 1997.

Peters, S.J., and G.E. Ewing, Thin film water on NaCl(100) under ambient conditions: An infrared study, *Langmuir, 13*, 6345-6348, 1997a.

Peters, S.J., and G.E. Ewing, Water on salt: An infrared study of adsorbed H2O on NaCl(100) under ambient conditions, *J. Phys. Chem. B, 101*, 10,880-10,886, 1997b.

Peters, C.A., K.H. Wammer, and C.D. Knightes, Multicomponent NAPL solidification thermodynamics, *Trans. Porous Med., 38,* 57-77, 2000.

Pitzer, K.S., Ion interaction approach: Theory and data, in *Activity Coefficients in Electrolyte Solutions,* edited by K. S. Pitzer, pp. 75-153, CRC Press, Boca Raton, Fla., 1991.

Pividal, K.A., and S.I. Sandler, Neighbor effects on the group contribution method–Infinite dilution activity-coefficients of binary-systems containing primary amines and alcohols, *J. Chem. Eng. Data, 35,* 53-60, 1990.

Quinn, J.A., R.A. Steinbrook, and J.L. Anderson, Breaking bubbles and the water-to-air transport of particulate matter, *Chem. Eng. Sci., 30,* 1177-1184, 1975.

Quinn, P.K., D.J. Coffman, V.N. Kapustin, T.S. Bates, and D.S. Covert, Aerosol optical properties in the marine boundary layer during the First Aerosol Characterization Experiment (ACE 1) and the underlying chemical and physical aerosol properties, *J. Geophys. Res., 103,* 16,547-16,564, 1998.

Quinn, P.K., T.S. Bates, D.J. Coffman, T.L. Miller, J.E. Johnson, D.S. Covert, J.-P. Putaud, C. Neusü, and T. Novakov, A comparison of aerosol chemical and optical properties from the 1st and 2nd Aerosol Characterization Experiments, *Tellus, Ser.*

B, 52, 239-257, 2000.

Reid, R.C., J.M. Prausnitz, and B.E. Poling, *The Properties of Gases and Liquids,* McGraw-Hill, New York, 1987.

Riley, J.P., and R. Chester, *Introduction to Marine Chemistry,* Academic, San Diego, Calif., 1971.

Riley, J.P., and D. Segar, Seasonal variation of the free and combined dissolved amino acids in the Irish Sea, *J. Mar. Biol. Assoc. U. K., 50,* 713-720, 1970.

Rogge, W.F., M.A. Mazurek, L.M. Hildemann, G.R. Cass, and B.R.T. Simoneit, Quantification of urban organic aerosols at a molecular level: Identification, abundance and seasonal variation, *Atmos. Environ., Part A, 27,* 1309-1330, 1993.

Saxena, P., and L.M. Hildemann, Water-soluble organics in atmospheric particles: A critical review of the literature and application of thermodynamics to identify candidate compounds, *J. Atmos. Chem., 24,* 57-109, 1996.

Saxena, P., and L.M. Hildemann, Water absorption by organics: Survey of laboratory evidence and evaluation of UNIFAC for estimating water activity, *Environ. Sci. Technol., 31,* 3318-3324, 1997.

Seinfeld, J.H., and S.N. Pandis, *Atmoshpeirc Chemistry and Physics,* John Wiley, New York, 1997.

Stokes, R.H., and R.A. Robinson, Interactions in aqueous nonelectrolyte solutions, I, Solute-solvent equilibria, *J. Phys. Chem., 70,* 2126-2130, 1966.

Swietlicki, E., et al., Hygroscopic properties of aerosol particles in the northeastern Atlantic during ACE-2, *Tellus, Ser. B, 52,* 750-778, 2000.

Tang, I.N., and H.R. Munkelwitz, Aerosol phase transformation and growth in the atmosphere, *J. Appl. Meteorol., 33,* 792-796, 1994.

Tang, I.N., A.C. Tridico, and K.H. Fung, Thermodynamic and optical properties

of sea salt aerosols, *J. Geophys. Res., 102,* 23,269-23,275, 1997.

Turpin, B.J., and H.J. Lim, Species contributions to PM2.5 mass concentrations: Revisiting common assumptions for estimating organic mass, *Aerosol Sci. Technol., 35,* 602-610, 2001.

Velezmoro, C.E., and A.J.A. Meirelles, Water activity in solutions containing organic acids, *Dry Technol., 16,* 1789-1805, 1998.

Weis, D.D., and G.E. Ewing, Infrared spectroscopic signatures of $(NH_4)_2SO4$ aerosols, *J. Geophys. Res., 101*, 18,709-18,720, 1996.

Wilemski, G., The Kelvin equation and self-consistent nucleation theory, *J. Chem. Phys., 103,* 1119-1126, 1995.

Wu, H.S., and S.I. Sandler, Proximity effects on the predictions of the UNIFAC model, 1, ethers, *AIChE J., 35,* 168-172, 1989.

Wu, H.S., and S.I. Sandler, Use of ab initio-quantum mechanics calculations in group contribution methods, 2, Test of new groups in UNIFAC, *Ind. Eng. Chem. Res., 30,* 889-897, 1991.

Xie, W.H., W.Y. Shiu, and D. Mackay, A review of the effect of salts on the solubility of organic compounds in seawater, *Mar. Environ. Res., 44,* 429-444, 1997.

Zhang, Y., C. Seigneur, J.H. Seinfeld, M. Jacobson, S.L. Clegg, and F.S. Binkowski, A comparative review of inorganic aerosol thermodynamic equilibrium modules: Similarities, differences, and their likely causes, *Atmos. Environ., 34,* 117-137, 2000.

Zhou, J., E. Swietlicki, O.H. Berg, P.P. Aalto, K. Hämeri, E.D. Nilsson, and C. Leck, Hygroscopic properties of aerosol particles over the central Arctic Ocean during summer, *J. Geophys. Res.,* in press, 2001.

Chapter 5

Fog Formation in Polluted Rural Environment

5.1 Case Study and Model Description

The Po Valley is a highly populated area under the impact of agricultural and industrial pollution. Fog forms frequently during the fall-winter season (30% of the time) as a result of ground temperature inversion favored by the surrounding mountain ranges. The Po Valley Fog Experiment 1989 was an extensive fog microphysics study, which took place at the FISBAT field station of S. Pietro Capofiume in November, 1990 (Fuzzi et al., 1992). The measured meteorological data include temperature, relative humidity (RH) and liquid water content (LWC) and gas-phase concentrations of SO_2, NO, NO_2, HNO_3, NH_3 and O_3 (Wobrock et al., 1992). In fog events, the interstitial aerosol and fog droplets were sampled by an inertial impactor and a Counterflow Virtual Impactor (CVI), respectively (Noone et al., 1989). The nominal cutoff diameter of the CVI was 5 μm. The accumulation-mode (dry diameter range 0.1 – 1.0 μm) size distributions of the dry interstitial and residual aerosol were determined by the Optical Particle Counters (OPCs) after sampling (Noone et al., 1992). A Tandem

Differential Mobility Analyzer (TDMA) was used to measure the hygroscopic growth factors of particles at submicron sizes (Svenningsson et al., 1992).

Both ammonium nitrate (NH_4NO_3) and ammonium sulfate ($(NH_4)_2SO_4$) account for approximately half of the inorganic aerosol mass in the Po Valley (Hallberg et al., 1992). Decesari et al. (2001) investigated the annual cycle of carbonaceous fraction of aerosol in the Po Valley in 1998 – 1999 with the same experimental techniques as Decesari et al. (2000) and found that 47% of organic mass was water soluble in November. Based on the functional group-level composition derived from HNMR, the organic fraction of particle mass was represented as a mixture of seven soluble organic compounds commonly found in the atmosphere (Fuzzi et al., 2001). There are two types of aerosol particles with different hygroscopicity: more and less hygroscopic particles. The average hygroscopic growth factors of both aerosols were measured to be 1.5 and 1.1 at 85% RH, respectively (Svenningsson et al., 1992).

This study uses a model with detailed aerosol dynamics (Russell and Seinfeld, 1998). The initial size distribution of aerosol is composed of two log-normal distributions: the accumulation-mode one fitted from the pre-fog measurement (Noone et al., 1992) and the nucleation-mode one assumed to be typical of rural aerosol (Jaenicke, 1993). The size distributions of the more and less hygroscopic particles are determined from their number fractions measured by Svenningsson et al. (1992). The chemical composition of aerosol is assumed to be independent of size due to the lack of size-resolved composition information. The inorganic fractions of more and less hygroscopic particles are 80% and 15%, respectively, based on the measured hygroscopic growth factors. The inorganic fraction is composed of 50% NH_4NO_3 and 50% $(NH_4)_2SO_4$. The organic fraction contains 53% insoluble compounds, while the seven water soluble compounds make up the rest of organic mass following the composition

suggested by Fuzzi et al. (2001). The surface tension of droplets are related to organic concentration based on Facchini et al. (2000).

The microphysical processes implemented in the model include condensation, coagulation and nucleation. The condensation and evaporation rates of nitric acid are calculated according to the approaches proposed by Makar et al. (1998) and Mozukewich (1993). The measurements of mass accommodation coefficient of nitric acid range from 0.19 at 268 K to 0.07 at 293 K (DeMore et al., 1994). A value of 0.15 is interpolated for the temperature of interest for this study (around 275 K). The measured concentrations of HNO_3 and NH_3 (Facchini et al., 1992) are used directly by this model. The aqueous phase oxidation of SO_2 in the fog system is negligible due to very low concentrations of SO_2 and oxidant species like O_3 and H_2O_2 in the period of experiment (Facchini et al., 1992). The condensation rate of water is calculated following the approach described in Seinfeld and Pandis (1997). According to the latest measurement by Li et al. (2001), the mass and heat accommodation coefficients of water used in the model are 0.2 and 1, respectively. The cutoff relative humidity, above which the mass transport of water between vapor and particles turns kinetic-controlled, is 99% (Pandis et al., 1990). The solution activities are calculated according to a thermodynamic model of aqueous solution containing both inorganic and organic compounds (Ming and Russell, 2002).

5.2 Results

We simulate Event 1 (November 10 – 11) and Event 4 (November 15 – 16) among a series of fog events observed in the Po Valley Fog Experiment. Model results and sensitivities to some key factors are discussed in details for Event 1, which is the base

case of our study, while Event 4 is to be briefly described given its similarity to Event 1.

Event 1: Base Case The first fog event spans two consecutive durations: one-hour pre-fog period (from 19:00 to 20:00, November 10) and five-hour fog period (from 20:00 PM, November 10 to 1:00, November 11) (all local time).

Pre-fog Period

The atmosphere remains below the cutoff relative humidity 99% in the pre-fog period. The distribution of water between ambient air and particles is at equilibrium. The water uptake by particles is calculated accordingly.

The size distributions of the less and more hygroscopic particles at the beginning and end of the pre-fog event are presented in Figure 5.1. As a result of high concentrations of HNO_3 and NH_3, NH_4NO_3 condenses onto particles and grows them. For the less hygroscopic particles, the diameter of the peak nucleation-mode concentration changes from 0.015 μm to 0.04 μm. The total particle number in that mode decreases by 15% due to coagulation. The condensation process also shifts the distribution towards larger sizes in the accumulation mode, but to a lesser extent. Similarly, the more hygroscopic particles experience growth in both modes. Nonetheless, the growth of the more hygroscopic particles in the accumulation mode is much more significant than that of the less hygroscopic particles. The diameter of the peak concentration of the more hygroscopic particles shifts from 1.5 μm to 2 μm. Because the more hygroscopic particles have a higher growth factor than the less hygroscopic particles at the same dry diameter and relative humidity, the surface area available for condensation is more abundant, and thus enhances the condensation process for the more hygroscopic particles.

Figure 5.1: Size distribution of particles at 19:00 (thin lines) and 20:00 (thick lines). For comparison, the thin dotted and dashed lines represent the size distribution of both aerosols at 19:00 in Event1. The distributions of the more hygroscopic particles are represented by dashed lines. The overall distributions of the more hygroscopic and less hygroscopic particles are represented by solid lines.

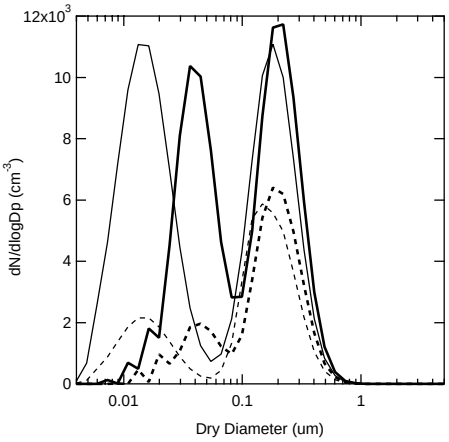

The size-resolved chemical compositions of both types of aerosol at the end of the pre-fog event (20:00) are plotted in Figure 5.2. The initial compositions at 19:00 are assumed to be uniform across the whole size range, since no size-resolved chemical composition is available. For the less hygroscopic particles, NH_4NO_3, $(NH_4)_2SO_4$ and organic compounds initially account for 7.5%, 7.5% and 85% of total dry mass, respectively. At 20:00, the average fraction of NH_4NO_3 is approximately 95% for particles smaller than 0.1 μm and 10% for particles larger than 1 μm. In the accumulation mode, this fraction gradually decreases from 95% to 10%, as particle size increases from 0.1 μm to 1 μm. The behavior of the more hygroscopic particles follows a similar pattern. The average fraction of NH_4NO_3 for particles less than 0.1 μm increases from 40% at 19:00 to nearly 98% at 20:00, while it remains almost unchanged at 40% for particles larger than 1 μm. In the accumulation mode, this fraction decreases almost linearly with the logarithmic dry diameter from 96% at 0.1 μm to 56% at 1 μm at

Figure 5.2: Fractions of NH_4NO_3 (gray column), $(NH_4)_2SO_4$ (black column) and organic species (white column) in (a) the less and (b) more hygroscopic particles at 20:00 in Event 1.

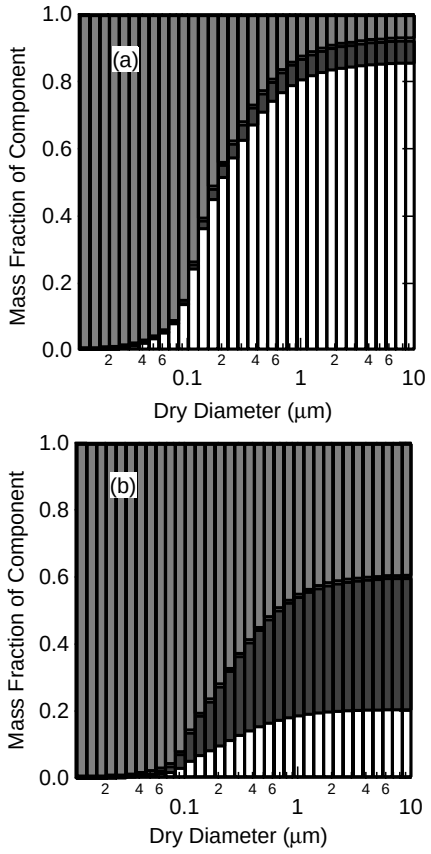

20:00, as compared to constant 40% at 19:00.

The hygroscopic growth factors of particles are dependent on chemical composition and ambient relative humidity. As shown by Figure 5.2, the mass fraction of NH_4NO_3 considerably increases for the sub-micron particles as a result of condensation. This change in chemical composition increases hygroscopicity as shown in Figure 5.3. For the less hygroscopic particles, the initial hygroscopic growth factor at 19:00 is approximately 1.1 at 85% relative humidity and increases with dry particle

Figure 5.3: Predicted hygroscopic growth factors of the less and more hygroscopic particles at 20:00 in Event 1 , represented by the thick dotted and thick dashed lines, respectively. For comparison, the thin dotted and dashed lines represent the predicted growth factors of both aerosols at 19:00.

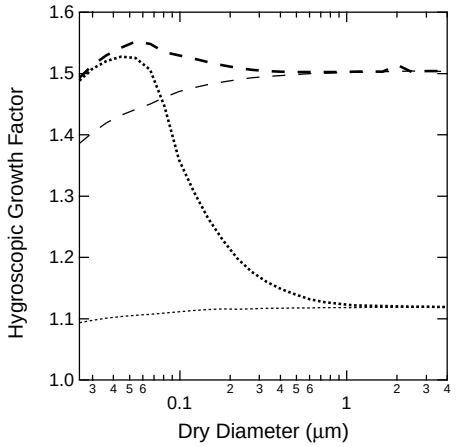

diameter due to the Kelvin effect. At 20:00, the hygroscopic growth factors for all sizes are higher than their initial values to different extents. The growth factors are over 1.5 for particles smaller than 0.1 μm and almost unchanged for particles greater than 1 μm. The particles in the accumulation mode have lower growth factors with increasing size. The increase in hygroscopicity is less significant for the more hygroscopic particles.

Fog Period

As a result of decreasing temperature, the relative humidity of ambient air reaches supersaturation at 20:00. As shown by Panel (a) of Figure 5.4, despite the fluctuation associated with the measured temperature profile (Wobrock et al., 1992), the general trend clearly describes a cooling process of air that is necessary for fog formation. The smooth temperature profile used in this simulation agrees with measurements well. The temperature starts from 275.4 K at 20:00, and gradually drops to 273.7 K

at 1:00 next day. The average temperature gradient is 0.34 K hour^{-1}. The simulated LWC and supersaturation are plotted in Panels (b) and (c), respectively. The supersaturation quickly reaches 0.025% at 20:30 and remains relatively constant until 11:30. During the same time period, the LWC rise from 19 mg m^{-3} at 20:00 to 150 mg m^{-3} at 21:30. The fog event begins to dissipate after 21:30. The LWC keeps on decreasing until it drops back to 0 mg m^{-3} at 1:00, while the supersaturation increases to a maximum of 0.03% from 21:30 to 22:15. After slowly decreasing to 0.022% at 0:20, the supersaturation rapidly drops back to 0% at 0:50 causing the end of fog.

The cutoff diameter used to separate droplets from interstitial aerosol in the CVI was 6 μm in Event 1. The activation diameters can be calculated from model simulation based on this cutoff value. In Figure 5.5, the calculated activation diameters of two types of aerosol are plotted against time in the first hour of fog formation (from 20:00 to 21:00). As a result of enhancing supersaturation, the activation diameters decrease for both aerosols. The curves are stepwise due to the limited number of size bins in our model. For the less hygroscopic particles, the activation diameter drops to 0.5 μm from 1.1 μm at the start of fog. CCN activation extends to the more hygroscopic particles as small as 0.4 μm, while only the less hygroscopic ones greater than 0.74 μm can activate at low supersaturation. The average CCN concentration is 149 cm^{-3}, among which 20 and 129 cm^{-3} are from the less and more hygroscopic particles, respectively.

The residual particle fractions in the first hour of fog formation are calculated from the activation diameter curves in Figure 5.6. For example, the more hygroscopic particles with dry diameter at 0.5 μm do not grow larger than 6 μm, the cutoff diameter for the CVI to sample droplets in Event 1, until 20:12. Since no particles in that size bin are collected by the CVI from 20:00 to 20:12, the calculated average

Figure 5.4: Temperature, Liquid Water Content (LWC) and supersaturation in Event 1. In Panel (a), the thin solid line with error bars represents measured temperature (Wobrock et al, 1992). The temperature profile used in this study is represented by the thick solid line. In Panel (b), the measured LWC (Fuzzi et al., 1992) is represented by squares with error bars. The thick solid and dotted lines represent the predicted LWC using decreased surface tension and constant surface tension of water, respectively. In Panel (c), the thick solid and dotted lines represent the predicted supersaturation using decreased surface tension and constant surface tension of water, respectively.

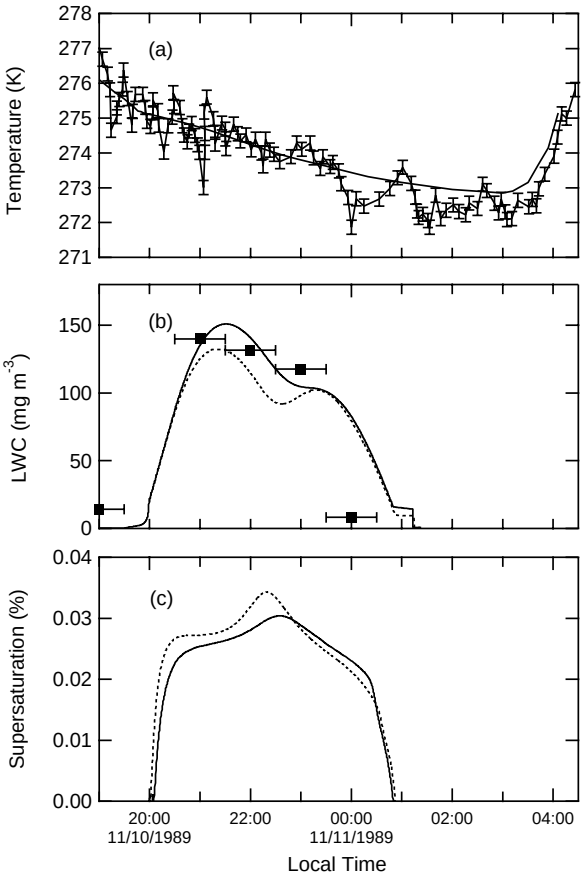

Figure 5.5: Activation diameters of the less and more hygroscopic particles from 20:00 to 21:00 in Event 1. The solid black and gray lines represent the less and more hygroscopic particles with decreased surface tension, respectively. The dotted black and gray lines represent the less and more hygroscopic particles with constant surface tension of water, respectively.

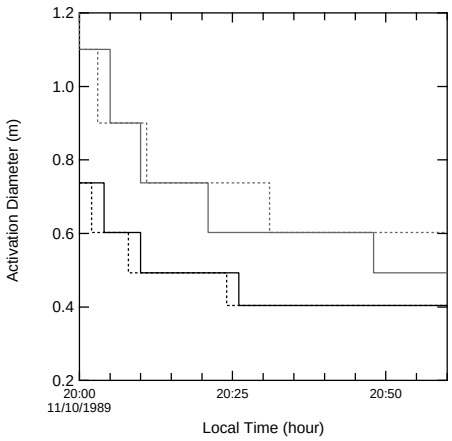

residual particle fraction from 20:00 to 21:00 stays at 80%. The less hygroscopic particles in the size bins lower than 0.5 μm are unable to activate and grow bigger than 6 μm. The residual number fraction increases to 47% for 0.6 μm, and further to 82% for 0.74 μm. 97% of the particles with dry diameter at 0.9 μm are counted as residual particles. All particles larger than 1.1 μm have 100% residual fraction. As compared to the less hygroscopic particles, the more hygroscopic particles as small as 0.4 μm are capable of activating to droplets and have a residual fraction of 43%. The residual particle fraction reaches 100% when the particle diameter is larger than 0.74 μm. The overall residual particle fraction is derived from averaging the fractions of both aerosols based on their number fractions. It is compared with the measured residual particle fractions (Noone et al., 1992). The simulation agrees well with measurements when the dry diameter is less than 0.5 μm. Both model simulation and measurement show that droplet activation does not happen to particles smaller

than 0.33 μm. There is a regime of relatively constant residual fraction between 0.5 and 0.7 μm in measurements, which was attributed to the difference in activation diameters of the more and less hygroscopic particles by Noone et al. (1992). They hypothesize that the more hygroscopic particles in this size range (0.5 – 0.7 μm) can activate as CCN, while the less hygroscopic particles cannot. In our model, CCN activation occurs for the less hygroscopic particles as small as 0.5 μm. In return, the residual fraction generally increases with dry diameter in the size range from 0.33 to 0.8 μm, without levelling off between 0.5 and 0.7 μm. As a result of strong entrainment unique to Event 1, a significant fraction (over 0.3) of particles larger than 0.8 μm did not activate in field measurement. In all other fog events, the measured residual particle fractions of particles larger than 0.8 μm were above 0.9 and consistent with the model. In Figure 5.7, the overall residual particle fraction is speciated into NH_4NO_3, $(NH_4)_2SO_4$ and organic compounds, which account for 45%, 21% and 34% of total CCN mass, respectively.

Event 4 Figure 5.8 summarizes the temperature, LWC and supersaturation in the simulation of Event 4. By using a temperature trend close to measurement, our model reaches a good agreement between the predicted and observed LWC. The temperature decreases at a rate of 0.8 K hour^{-1} in Event 4, faster than 0.34 K $^{-1}$ in Event 1. Consequently, the maximum LWC in Event 4 is 360 mg m^{-3}, more than twice as high as in Event 1. Despite higher cooling rate and LWC, the maximum supersaturation in Event 4 is 0.032%, only slightly higher than 0.030% in Event 1.

Sensitivity The simulation of CCN activation involves understanding processes on three levels: individual particles, entire particle population and dual–phase system consisting of vapor and particles. Among the factors determining the condensation of water onto a single particle are its surface tension and chemical composition, both

Figure 5.6: Average residual particle fractions of particles from 20:00 to 21:00 in Event 1. The solid gray line and black lines represent the residual particle fractions of the less and more hygroscopic particles with decreased surface tension, respectively. The dotted gray and black lines represent the residual particle fractions of the less and more hygroscopic particles with constant surface tension of water, respectively. The thick solid and dotted lines represent the overall residual particle fractions of particles with decreased surface tension and constant surface tension of water, respectively. The measured residual particle fraction in Event 1 is represented by the solid line with squares (Noone et al., 1992).

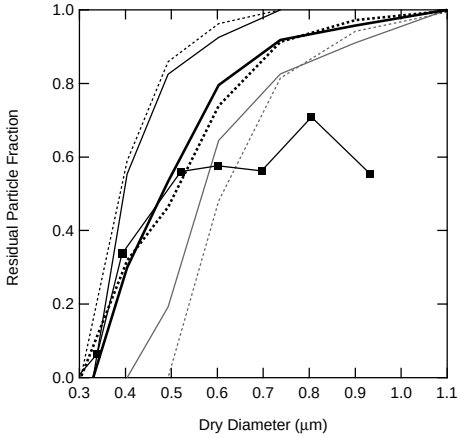

Figure 5.7: Contributions of NH_4NO_3 (white), $(NH_4)_2SO_4$ (gray) and organic compounds (black) to the average residual particle fractions of particles from 20:00 to 21:00 in Event 1.

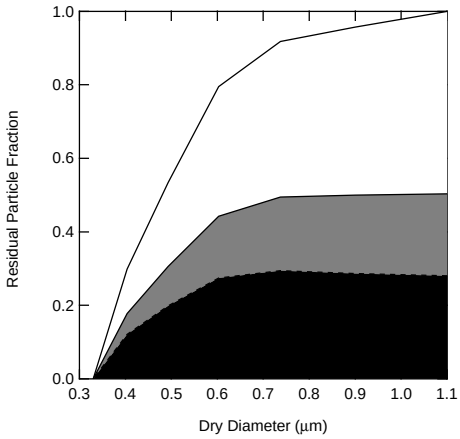

Figure 5.8: Temperature, Liquid Water Content (LWC) and supersaturation in Event 4. In Panel (a), the thin solid line with error bars represents measured temperature (Wobrock et al, 1992). The temperature profile used in this study is represented by the thick solid line. In Panel (b), the measured and predicted LWC (Fuzzi et al., 1992) is represented by squares with error bars and solid line. In Panel (C), the predicted supersaturation is represented by solid line.

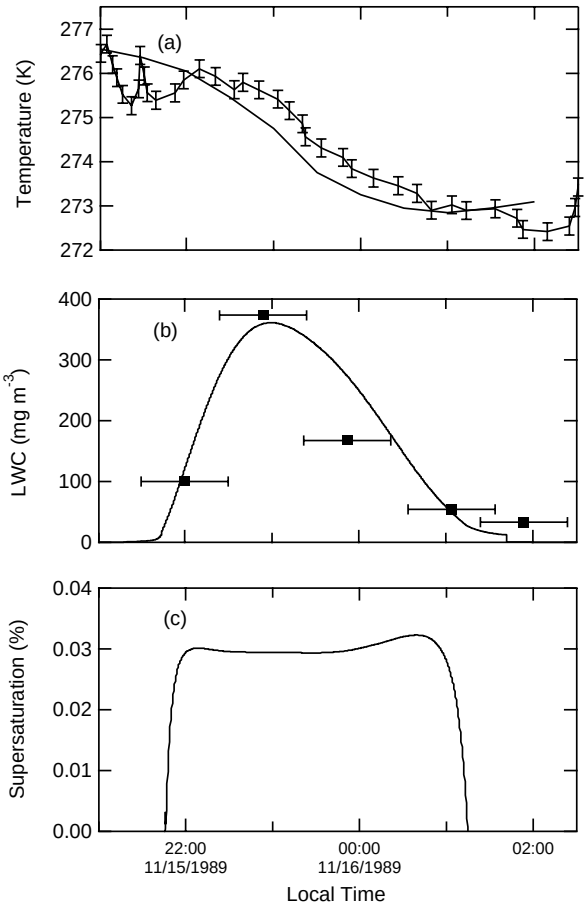

of which are altered by organic components. The collective condensation rate of the whole population translates into the change of LWC and supersaturation, which in return controls water condensation of individual particles. Total water content is no longer conserved as a result of wet deposition. Varying total water content affects the relationship between LWC and supersaturation. We examine the influences of those factors on fog simulation and identify the ones to which the model results are most sensitive.

Surface Tension

The presence of surface–active organic compounds expedites water condensation by lowering surface tension of droplets as compared to pure water. The simulation of fog period is rerun by using a higher surface tension of water. The results are compared with the base case in Figure 5.4. The water condensation in the comparative case is slower than in the base case due to increased surface tension. The LWC in the comparative case reaches a maximum 132 mg m^{-3} at 21:15 as compared to 150 mg m^{-3} in the base case. As the opposite process to condensation, water evaporation in the comparative case also takes place at a lower rate than in the base case. Unlike the base case, the decelerated evaporation leads to a second maximum LWC in the comparative case. The supersaturation with higher surface tension remains relatively constant in most time of fog event. The maximum supersaturation is 0.035%, higher than 0.03% in the base case. The higher supersaturation in the comparative case prompts the more hygroscopic particles to grow faster than in the base case, while the growth of the less hygroscopic particles is delayed as a result of increased surface tension (Figure 5.5). The residual particle fraction with higher surface is compared to the base case in Figure 5.6. The average CCN concentration in this case is 147

cm^{-3}, only slightly lower than 149 cm^{-3} in the base case.

Chemical Composition

We study three alternative chemical compositions: the more hygroscopic particles composed of 100% inorganic salts (50% NH_4NO_3 and 50% $(NH_4)_2SO_4$) (the inorganic case); all soluble organic component as malic acid (the soluble case); and all organic components as insoluble (the insoluble case). The model results are summarized in Figure 5.9. The substitution of 20% organic components with salts for the more hygroscopic particles increases the number of ions available for dissolution and particle surface tension at the same time, whereas both effects work in opposite directions in affecting CCN efficiency. Our model results show that the effect of increased surface tension, which retards water uptake by particles, outweights the gain in CCN efficiency due to solvation. The LWC in the inorganic case is 7% lower than in the base, while the supersaturation is 10% higher. Malic acid has a smaller molecular weight than all the model compounds used in the base, thus resulting in more organic ions per unit dry particle mass. Consequently the LWC in the soluble case is 3% higher than in the base case. For most of fog lifetime, the supersaturation in the soluble case is slightly (within 1%) lower than in the base case. Treating all inorganic components as insoluble reduces ions available for solvation. This effect is reflected by the LWC 4% lower than in the base case and supersaturation 2% higher than in the base case. As shown in Figure 5.10, the residual particle fraction in the soluble case is higher than the base case, while the fraction in the insoluble case is lower. In the inorganic case, particles larger than 0.6 μm have higher residual fractions than those in the base case, while particles smaller than 0.6 μm have lower residual fractions. The average CCN concentrations in the inorganic, soluble and insoluble cases are 135,

147 and 156 cm^{-3}, as compared to 149 cm^{-3} in the base case.

Condensation

The condensation of NH_4NO_3 prior to fog increases the inorganic fractions of both the more and less hygroscopic particles and total soluble mass. In order to assess the effect of condensation on CCN efficiency, we simulate both stages of fog event with all microphysical processes in the base case except condensation of non-water gas species (namely NO_2, SO_2 and NH_3). In the pre-fog period, the absence of condensation leaves the chemical compositions of particles little changed. The predicted LWC and supersaturation are compared with the base case in Figure 5.9. The comparative case has a maximum LWC of 120 mg m^{-3}, considerably lower than 150 mg m^{-3} in the base case. After rising rapidly to 0.03%, the supersaturation in the comparative case keeps relatively constant until 21:00, and further peaks at 0.037% at 22:00. For comparison, the maximum supersaturation in the base case is 0.03%. Despite higher residual particle fractions (Figure 5.10), the average CCN concentration in the case without condensation is 118 cm^{-3}, 20% lower than in the base case.

Wet Deposition

Dry particle mass together with absorbed liquid water is removed from the atmosphere spontaneously as a result of wet deposition in the base case. We study two comparative schemes concerning wet deposition to assess its influence on model results. The wet deposition of particles is completely turned off in the first case. Thus the fog system is treated as a closed one, in which the total water content and particle mass are conserved. Though the assumption of a closed system is not strictly applicable to any fog system, a fog event of short duration (e.g. within 1 hour) may behave

Figure 5.9: Influence of composition and condensation on the predicted liquid Water Content (LWC) (a) and supersaturation (b) in Event 1. The base case is represented by the solid line. The other compositions are base on converting the organic fractions in the base case composition to inorganic salts, malic acid and insoluble organic species and represented by the dotted, dashed and dotted-dashed lines, respectively. The results without condensation are represented by the dotted-dotted-dashed line.

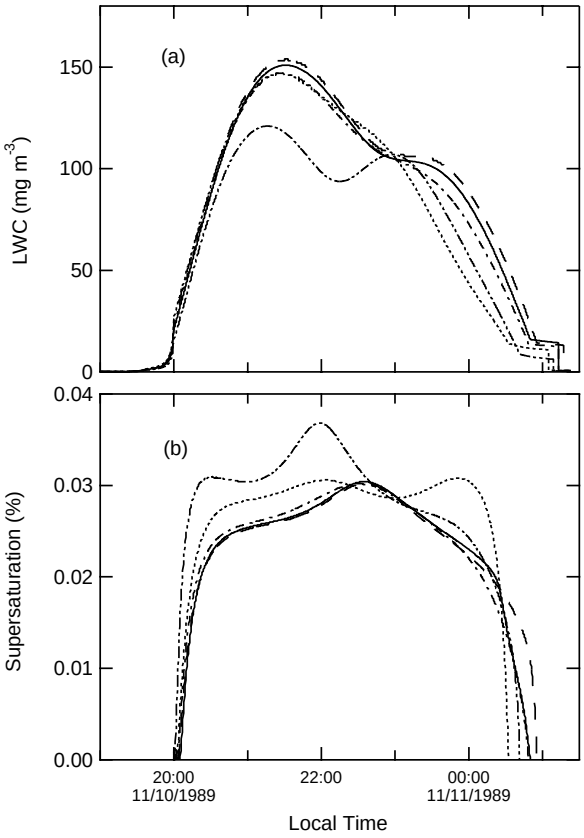

Figure 5.10: Influence of composition and condensation on the residual particle fractions of particles in Event 1. The thin gray and thin black lines represent the residual particle fractions of the less and more hygroscopic particles, respectively. The thick black lines represent the overall residual particle fractions. The base case is represented by the solid line. The other compositions are base on converting the organic fractions in the base case composition to inorganic salts, malic acid and insoluble organic species and represented by the dotted, dashed and dotted-dashed lines, respectively. The results without condensation are represented by the dotted-dotted-dashed lines.

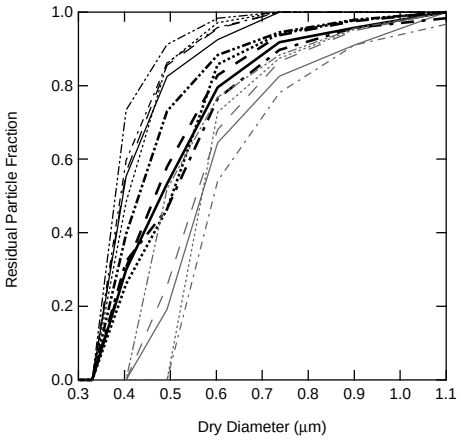

like a closed one given the negligible removal of particles and liquid water through wet deposition in the lifetime of fog. The second scheme only allows dry particle mass to deposit, whereas total water content is conserved. The assumption behind this scheme is that all liquid water removed by wet deposition is capable of evaporating back into the atmosphere instantaneously. Figure 5.11 compares the model results for these schemes with the base case. Both schemes produce similar trends of LWC, which keeps on increasing with decreasing temperature. The conserved total water content in both schemes gives rise to a maximum LWC of 595 mg m^{-3} at 0:10, much higher than 150 mg m^{-3} in the base case. The supersaturation in the first scheme increases rapidly to 0.022% from 20:00 to 20:35 and starts to gradually decrease to 0.008% at 1:00 thereafter. Fluctuation with increasing amplitude is characteristic of the simulated supersaturation in the second scheme. A maximum supersaturation of 0.066% is reached at 0:50.

5.3 Discussion

The Köhler equation describes the distribution of water between supersaturated vapor and droplets at equilibrium by quantifying the solvation and surface tension effects in CCN activation. Figure 5.12 presents the critical supersaturation S_c necessary for particle activation and corresponding droplet sizes $D_{p,c}$. At the same dry diameter, the more hygroscopic particles activate at a critical supersaturation 30% lower than the less hygroscopic ones, while the droplets resulting from more hygroscopic particles are 15% bigger than those from less hygroscopic particles.

The characteristic timescale for water to reach equilibrium between vapor and droplets is longer than that for mass transport at low supersaturation (Chuang et al.,

Figure 5.11: Liquid Water Content (LWC) (a) and supersaturation (b) using different schemes of wet deposition in Event 1. In the base case (solid line), deposition of both dry particles and liquid water is allowed. Two comparative schemes are: no deposition of either dry particles or liquid water (dotted line) and deposition of only dry particles (dashed line).

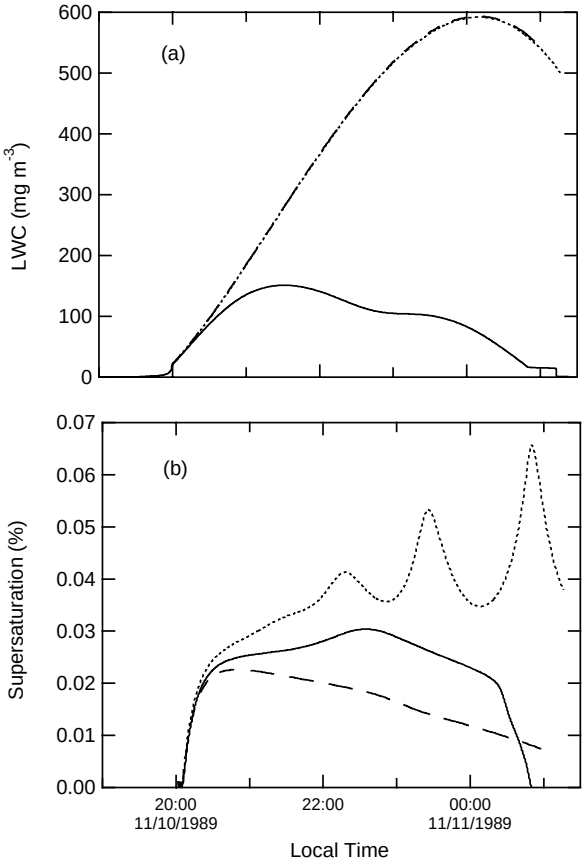

Figure 5.12: Critical supersaturation and wet diameter with decreased surface tension (solid lines) and with constant surface tension (dashed lines) for the less (gray lines) and more (black lines) hygroscopic particles.

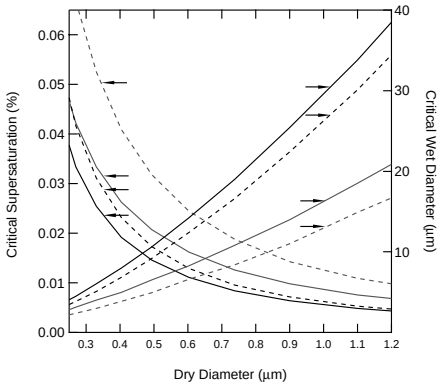

1997). In this scenario, no enough time is available for water to reach equilibrium, so the kinetic wet diameter is always lower than the equilibrium diameter calculated from the Köhler equation. Such a lagging in water condensation is evident from comparing the path of a growing particle as calculated in our kinetic simulation to the equilibrium path as represented by the Köler curve in Figure 5.13. For a more hygroscopic particle with dry diameter at 0.33 μm, the critical supersaturation S_c and droplet diameter $D_{p,c}$ of the Köhler curve are 0.025% and 6.0 μm. At supersaturation lower than S_c, the kinetic droplet diameter is 9% smaller than the equilibrium diameter in average.

There are two questions concerning CCN activation unanswered by the Köhler curve. (1) Since droplets are not capable of reaching equilibrium with water vapor that has a supersaturation exceeding S_c, the equilibrium-based Köhler curve provides no hint to particle growth in that regime. (2) The decreasing branch of the Köhler curve, which holds once droplets grow beyond $D_{p,c}$, is thermodynamically unstable. Droplets in that regime tend to grow freely at a specific supersaturation, instead of staying at equilibrium sizes, given the unavoidable energy perturbation. The problem

Figure 5.13: Kinetic (dashed line) and equilibrium (solid line) paths of a more hygroscopic particle with dry diameter at 0.33 μm.

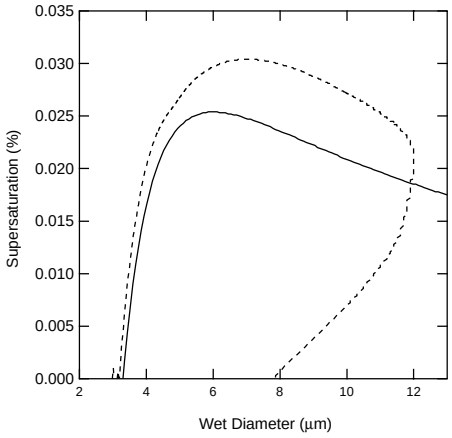

is further complicated by the fact that droplets will grow infinitely as supersaturation drops towards 0% according to the Köhler curve. One implication of this behavior is that the LWC of fog will keep on increasing when supersaturation is maintained. Obviously, it contradicts the observed dissipation stage of fog. Kinetic simulations help to answer these questions. As shown by the example in Figure 5.13, the droplet continues to grow after the actual supersaturation S exceeds S_c, since the difference $S - Sc$ provides the driving force for mass transport of water between vapor and droplet and determines its direction. If S stays above S_c as represented by the Köhler curve, the droplet experiences continuous growth in Figure 5.13. The droplet begins to shrink when S drops below Sc corresponding to the wet diameter, which is 0.019% at 12 μm. The process of shrinking gives rise to the dissipation of fog. In the regime of growth ($S > S_c$), the Köhler curve underestimates droplet size by up to 80%. In the regime of shrinking ($S > S_c$), the overestimation by using the Köhler curve could well amount to several times.

Figure 5.14: Activation diameters of the less and more hygroscopic particles from 20:00 to 22:30 in Event 1. The solid gray and black lines represent the less and more hygroscopic particles using kinetic simulation, respectively. The dashed gray and black lines represent the less and more hygroscopic particles with equilibrium calculation, respectively.

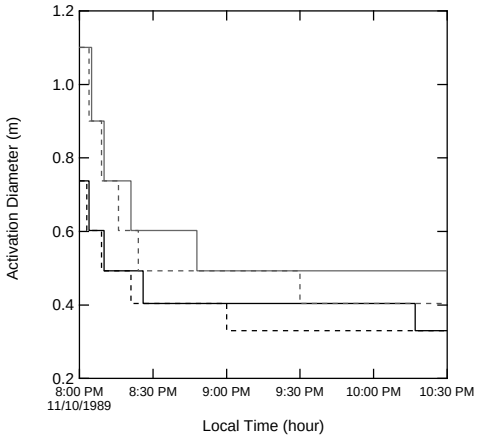

The equilibrium activation diameter at the supersaturation from kinetic simulation is calculated with the Köhler equation and compared to the kinetic activation diameter in Figure 5.14. For both types of particles, the equilibrium activation diameter agrees with the kinetic one in the time from 20:00 to 20:15, when the supersaturation is below 0.015%.Then the kinetic activation diameter begins to fall behind the equilibrium one. For the less hygroscopic particles, the equilibrium activation diameter decreases to 0.5 μm at 20:24, whereas it does not occur for the kinetic one until 20:48. Similarly the time for the more hygroscopic particles at 0.33 μm to activate is delayed from 21:00 for the equilibrium case to 22:17 for the kinetic case. The fog system studied here is obviously kinetic-controlled. Kinetic simulation is in need for the purpose of understanding the evolution of LWC and supersaturation in fog events. This observation is consistent with the finding of Chuang et al. (1997) given the weak supersaturation of fog (maximum 0.03%).

Surface-active organic compounds have an effect of lowering the surface tension of droplets (Facchini et al., 2000). We use the Köhler equation to calculate the critical supersaturation for both types of particles with the constant surface tension of water and compare them to the base case using decreased surface tension in Figure 5.12. Higher surface tension increases the critical supersaturation for both types of particles at a certain dry diameter, though this effect is more obvious for the less hygroscopic particle as a result of high organic fraction. The activation diameter at 0.025% with constant surface tension are 0.60 μm and 0.39 μm for the less and more hygroscopic particles, respectively, as compared to 0.40 μm and 0.33 μm with decreased surface tension. This increase in activation diameter causes total CCN concentration to decrease from 149 to 101 cm^{-3} by using the pre-fog size distribution of particles. Mircea et al. (2002) reached a similar estimate that the decreased surface tension due to organic components increases the CCN number concentration of rural aerosol by 97%.

Our kinetic simulation shows that the influence of decreased surface tension on CCN activation is not as important as the equilibrium calculations performed at a fixed maximum supersaturation imply. For the more hygroscopic particles, both of the kinetic activation diameters with constant and decreased surface tension stay at 0.39 μm, while they are 0.49 μm and 0.60 μm for the less hygroscopic particles (Figure 5.5). The difference in CCN concentration is well within 5%. Although lower surface tension reduces critical supersaturation, it also causes particles to grow bigger than they would with constant surface tension (Figure 5.12). The amount of water absorbed by individual CCN increases as a result of decreased surface tension. The increase in LWC with decreased surface tension suppresses supersaturation, which determines activation diameter. These two factors, the reduced critical supersaturation

required for CCN activation and suppressed supersaturation in fog, work in opposite directions. The former causes particles to activate at a lower supersaturation, while the latter decreases the maximum supersaturation that occurs during the fog event. Our simulation shows that two effects cancel out to a large extent. This leaves CCN concentration little changed. For the same reason, our simulation find that the presence of organic components in marine aerosol increases CCN concentration by 6% as compared to using purely inorganic aerosol, instead of 15% estimated by Mircea et al. (2002).

Inorganic salts such as NH_4NO_3 and $(NH_4)_2SO_4$ can contribute more ions for solvation as a result of their high dissociation rates and low molecular weights as compared to organic compounds. However, the critical supersaturation of purely inorganic particles is higher than that of the more hygroscopic particles containing 20% organic species (Figure 5.15) as a result of decreased surface tension. For the more hygroscopic particles mainly composed of inorganic salts, the critical supersaturation is not sensitive to the organic composition. This provides indirect evidences that the solvation effect of organic components are negligible for inorganic-dominant particles. On the other hand, the solubility of organic components plays an important role in determining the CCN efficiency of the organic-dominant less hygroscopic particles. Treating organic fraction as highly soluble small molecules like malic acid decreases the critical supersaturation by 2%, while a totally insoluble organic fraction increases it by 5%.

Figure 5.15: Critical supersaturation of different compositions for the less (gray lines) and more (black lines) hygroscopic particles. The base, inorganic, soluble and insoluble cases are represented by solid, dotted, dashed and dotted-dashed lines, respectively.

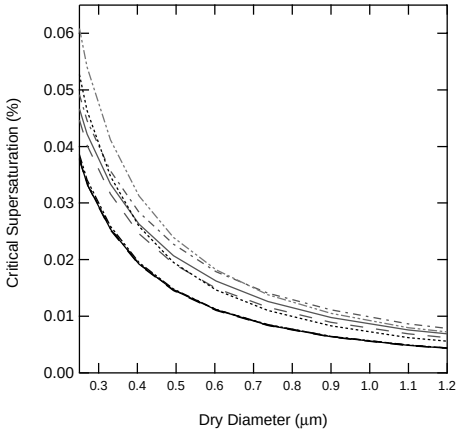

5.4 Conclusions

We simulate a fog event based on field measurements performed in the Po Valley Fog Experiment 1989 with a dynamic aerosol model (Russell and Seinfeld, 1998). The organic composition is represented by seven soluble organic compounds (Fuzzi et al., 2001). The relationship between decreased surface tension of droplets due to surface-active organic species and organic concentration measured by Facchini et al. (2000) is employed to calculated surface tension. The maximum supersaturation in the fog period is 0.03%, while the activation diameters are 0.6 μm and 0.4 μm for the less and more hygroscopic particles, respectively. The calculated residual particle fraction is in good agreement with measurements (Noone et al., 1992). The CCN concentration increases by 7% as a result of decreased surface tension caused by organic components. The critical supersaturation for organic-dominant particles is sensitive to organic composition. The condensation of inorganic salts like NH_4NO_3

enhances the hygroscopicity and CCN efficiency of particles. Soluble compounds have an effect of lowering critical supersaturation by 20%.

References

Chuang, P. Y., Charlson, R. J., and Seinfeld, J. H. (1997). Kinetic Limitations on Droplet Formation in Clouds, *Nature* 390:594-596.

Corrigan, C. E., and Novakov, T. (1999). Cloud Condensation Nucleus Activity of Organic Compounds: A Laboratory Study, *Atmos. Environ.* 33A:2661-2668.

Cruz, C. N. and Pandis, S. N. (1997). A Study of the Ability of Pure Secondary Organic Aerosol to Act as Cloud Condensation Nuclei, *Atmos. Environ.* 31A:2205-2214.

Cruz, C. N. and Pandis, S. N. (2000). Deliquesence and Hygroscopic Growth of Mixed Inorganic–Organic Atmoshperic Aerosol, *Environ. Sci. Technol.* 34:4313-4319.

Decesari, S., Facchini, M. C., Fuzzi, S., and Tagliavini, E. (2000). Characterization of Water-Soluble Organic Compounds in Atmospheric Aerosol: A New Approach, *J. Geophys. Res.* 105:1481-1489.

Decesari, S., Facchini, M. C., Matta, E., Lettini, F., Mircea, M., Fuzzi, S., Tagliavini, E., and Putaud, J. P. (2001). Chemical Features and Seasonal Variation of Fine Aerosol Water-soluble Organic Compounds in the Po Valley, Italy, *Atmos. Environ.* 35:3691-3699.

DeMore, W. B., Sander, S. P., Howard, C. J., Ravishankara, A. R., Golden, D. M., Kolb, C. E., Hampson, R. F., Molina, M. J., and Kurylo, M. J. (1994). Chemical Kinetics and Photochemical Data for Use in Stratospheric Modeling, JPL 94-26, Jet

Propul. Lab., Calif. Inst. of Technol., Pasadena.

Duce, R. A., Mohnen, V. A., Zimmerman, P. R., Grosjean, D., Cautreels, W., Chatfield, R., Jaenicke, R., Ogren, J. A., Pellizzari, E. D., and Wallace, G. T. (1983). Organic Material in the Global Troposhpere, *Rev. Geophys.* 21:921-952.

Facchini, M. C., Fuzzi, S., Kessel, M., Wobrock, W., Jaeschke, W., Arends, B. G., Mols, J. J., Berner, A., Solly, J., Kruisz, C., Reischl, G., Pahl, S., Hallberg, A., Ogren, J. A., Fierlingeroberlinninger, H., Marzorati, A., and Schell, D. (1992). The Chemistry of Sulfur and Nitrogen Species in a Fog System – A Multiphase Approach, *Tellus B* 44:505-521.

Facchini, M. C., Decesari, S., Mircea, M., Fuzzi, S., and Loglio, G. (2000) Surface Tension of Atmospheric Wet Aerosol and Cloud/Fog Droplets in Relation to Their Organic Carbon Content and Chemical Composition, *Atmos. Environ.* 34:4853-4857.

Fuzzi, S., Decesari, S., Facchini, M. C., Matta, E., Mircea, M., and Tagliavini, E. (2001). A Simplified Model of the Water Soluble Organic Component of Atmospheric Aerosols, *Geophys. Res. Lett.* 28:4079-4082.

Hallberg, A., Ogren, J. A., Noone, K. J., Heintzenberg, J., Berner, A., Solly, I., Kruisz, C., Reischl, G., Fuzzi, S., Facchini, M. C., Hansson, H. C., Wiedensohler, A., Svenningsson, I. B. (1992). Phase Partitioning for Different Aerosol Species in Fog, *Tellus B* 44:545-555.

Haywood, J. M. and Ramaswamy, V. (1998). Global sensitivity studies of the direct radiative forcing due to anthropogenic sulfate and black carbon aerosols, *J. Geophys. Res.* 103:6043-6058.

Jaenicke, R. (1993). Tropospheric Aerosols, in *Aerosol–Cloud–Climate Interactions*, edited by P. V. Hobbs. Academic Press, San Diego, CA.

Li, Y. Q., Davidovits, P., Shi, Q., Jayne, J. T., Kolb, C. E., Worsnop, D. R.

(2001). Mass and Thermal Accommodation Coefficients of H_2O(g) on Liquid Water as a Function of Temperature, *J. Phys. Chem. A* 105:10627-10634.

Majeed, M. A. and Wexler, A. S. (2001). Microphysics of Aqueous Droplets in Clouds and Fogs as Applied to PM-fine Modeling, *Atmos. Environ.* 35:1639-1653.

Makar, P. A., Wiebe, H. A., Staebler, R. M., Li, S. M., and Anlauf, K. (1998). Measurement and Modeling of Particle Nitrate Formation, *J. Geophys. Res.* 103:13095-13110.

Middlebrook, A. M., Murphy, D. M., and Thomson, D. S. (1998). Observations of Organic Material in Individual Marine Particles at Cape Grim During the First Aerosol Characterization Experiment (ACE 1), *J. Geophys. Res.* 103:16475-16483.

Ming, Y., and Russell, L. M. (2002). Thermodynamic Equilibrium of Organic–Electrolyte Mixtures in Aerosol Particles, *AIChE J.* 48:1331-1348.

Mircea, M., Facchini, M. C., Decesari, S., Fuzzi, S., and Charlson, R. J. (2002). The Influence of the Organic Aerosol Component on CCN Supersaturation Spectra for Different Aerosol Types, *Tellus B*, 54:74-81.

Mozurkewich, M. (1993). The Dissociation-Constant of Ammonium-Nitrate and its Dependence on Temperature, Relative-Humidity and Particle-Size, *Atmos. Environ.* 27:261-270.

Noone, K. J., Ogren, J. A., Hallberg, A., Heintzenberg, J., Strom, J., Hansson, H. C., Svenningsson, B., Wiedensohler, A., Fuzzi, S., Facchini, M. C., Arends, B. G., and Berner, A. (1992). Changes in Aerosol Size and Phase Distributions Due to Physical and Chemical Processes in Fog, *Tellus B*, 54:489-504.

Pandis, S. N., Seinfeld, J. H., and Pilinis, C. (1990). Chemical-Composition Differences in Fog and Cloud Droplets of Different Sizes, *Atmos. Environ.*, 24:1957-1969.

Rogge, W. F., Mazurek, M. A., Hildemann, L. M., Cass, G. R., and Simoneit B. R. T. (1993). Quantification of Urban Organic Aerosols at a Molecular–Level – Identification, Abundance and Seasonal–Variation, *Atmos. Environ.* 27A:1309-1330.

Russell, L. M., and Seinfeld, J. H. (1998). Size- and Composition-resolved Externally Mixed Aerosol Model, *Aerosol Sci. Tech.*, 28:403-416.

Russell, L. M., Noone, K. J., Ferek, R. J., Pockalny R. A., Flagan R. C., and Seinfeld J. H. (2000). Combustion Organic Aerosol as Cloud Condensation Nuclei in Ship Tracks, *J. Atmos. Sci.* 57:2591-2606.

Seinfeld, J. H., and Pandis, S. N. (1997) *Atmospheric Chemistry and Physics.* John Wiley & Sons, New York.

Svenningsson, I. B., Hansson, H. C., Wiedensohler, A., Ogren, J. A., Noone, K. J., and Hallberg, A. (1992). Hygroscopic Growth of Aerosol-Particles in the Po Valley, *Tellus B*, 44:556-569.

Wobrock, W., Schell, D., Maser, R., Kessel, M., Jaeschke, W., Fuzzi, S., Facchini, M. C., Orsi, G., Marzorati, A., Winkler, P., Arends, B. G., and Bendix, J. (1992). Meteorological Characteristics of the Po Valley Fog, *Tellus B* 44:469-488.

Chapter 6

Cloud Formation in Clean Marine Environment

6.1 Overview of ACE 1

The First Aerosol Characterization Experiment (ACE 1) was carried out from November 15 to December 14, 1995 over the southwestern Pacific (south of Australia) with the purpose to better understand the chemical, physical, radiative and cloud properties of aerosol and relevant controlling processes in background clean marine environment (Bates et al., 1997a). There were multiple platforms available for instrumental measurements in ACE 1. The NOAA ship *Discoverer* was used as a mobile station to measure the oceanic concentration of DMS, which is essential for a precise calculation of ocean-atmosphere DMS fluxes. Other shipboard measurements include concentrations of gas species (i.e. DMS, ozone, NO, NO_2 and ammonia), mass size distribution, optical and hygroscopic properties of aerosol at sea level. The vertical structure of the lower atmosphere (Marine Boundary Layer (MBL) and free troposphere) and properties of aerosol at different altitudes were measured aboard the NCAR C-130 aircraft. The gas-phase concentrations of ammonia, DMS, OH radicals, H_2SO_4, H_2O_2, number

size distributions, cloud condensation nuclei (CCN) concentration and optical properties of aerosol were among a variety of measurements performed in the research flights of the C-130. The ground-based measurements at Macquarie Island and Cape Grim provided continuous observations of aerosol that were only under the influences of local climatologies.

In two Lagrangian experiments (Lagrangian A and B) in ACE 1, the air mass marked by balloons launched from the *Discoverer* was tracked and sampled in several flights of the C-130. Lagrangian A and B were consisted of Research Flight (RF) 18-20 and 24-26, respectively. The goal of Lagrangian experiments was to study the evolution of aerosol and gas-phase species by continuously measuring the same air mass. In such a way, the interferences resulting from sampling different air mass can be avoided.

6.2 Model Description

We used a numerical model with detailed aerosol dynamics (Russell and Seinfeld, 1998) to simulate the evolution of aerosol and cloud formation in Flight 25, one of the Lagrangian B flights in ACE 1. The same model was utilized by Russell et al. (1999) to study aerosol dynamics in and out of ship tracks in clean and continentally influenced conditions. The size domain in the model is covered by a set of size bins with fixed dry diameters. Gas-phase species are allowed to condense onto aerosol populations at these fixed size bins. In such a way, the size-resolved chemical compositions of an aerosol population can be studied. The model can track multiple types of aerosol characterized by similar compositions simultaneously. The new particle formed from coagulation between two particles of different types and sizes is treated

as belonging to the type of the bigger particle, which contributes more mass and thus is more similar to the new particle in terms of chemical composition than the smaller one. The other microphysical processes included in the model include nucleation and deposition.

There exist two types of externally mixed aerosol in marine environment: sea salt and non-sea-salt (nss) sulfate. Sea salt aerosol is generated from mechanic disturbance of sea water like breaking waves and burble-bursting. Marine organisms produce sulfur-containing DMS, which can be oxidized to SO_2 and further to sulfuric acid after being emitted into the atmosphere and give rise to nss sulfate aerosol. Bates et al. (1998b) showed that sea salt accounts for more than 99% of coarse particle (dry diameter larger than 0.3 μm) mass and around 60% of accumulation-mode particle (dry diameter between 0.08 and 0.3 μm) mass in ACE 1. Experimental data collected during ACE 1 also showed that more than 90% of aerosol particles with dry diameters greater than 0.13 μm contained sea salt and less than 1% of these consist of pure sulfate (Murphy et al., 1998). In order to derive the size distributions of sea salt and nss sulfate aerosols from the overall size distribution measured in field, we assume that all particles larger than 0.3 μm are sea salt aerosol based on the observations in Bates et al. (1998b) and Murphy et al. (1998). The distribution of sea salt particles smaller than 0.3 μm can be extrapolated from that of coarse particles by using the normalized size distribution of sea salt measured by Bowyer et al. (1990). The size distributions of nss sulfate aerosol is simply the difference between the overall distribution and the distribution of sea salt aerosol. The initial size distributions of both types of aerosol used in our study are derived following this approach and plotted in Figure 6.1. Sulfate aerosol dominates the size range of dry diameter less than 0.1 μm and contributes 39% of particles with dry diameters between 0.1 μm

Figure 6.1: Size distributions of marine aerosols at t = 0 hour (thin lines) and t = 20 hour (thick lines). The distributions of sea salt aerosol are represented by dashed lines. The overall distributions of both sea salt and sulfate aerosols are represented by solid lines.

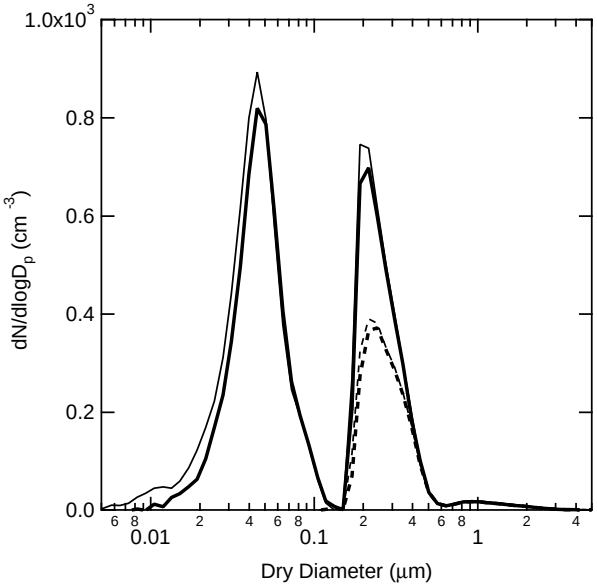

and 0.4 μm, the rest of which along with all particles larger than 0.4 μm are sea salt aerosol.

The production rate of sea salt aerosol at sea-air interface together with its deposition rate determines the atmospheric concentration of sea salt aerosol. Once the concentration of sea salt aerosol reaches steady state, the production and deposition rates must be equal to each other in order to maintain constant concentration. Bates et al. (1998a) related the number concentration of coarse-mode sea salt aerosol to wind speed. The average wind speed during Flight 25 was 5.9 m s^{-1}, at which the average ambient concentration of coarse sea salt aerosol is 11 cm^{-3}. If the size distribution of sea salt aerosol complies with the normalized distribution measured by

Bowyer et al. (1990), the coarse-mode particles account for 32% of all sea salt particles. Therefore the derived total concentration of sea salt aerosol during Flight 25 is 34 cm^{-3}. The production rate of sea salt aerosol used in our study is calculated by computing the deposition rate based on the derived size distribution.

According to the ship-based measurements by Quinn et al. (1998), the average NH_4^+/SO_4^{2-} molar ratio in sulfate aerosol is 0.77 during Flight 25, which is within the range of 0.9 $\pm$ 0.7 from the aircraft-based measurements in MBL (Huebert et al., 1998). Most of the reported NH_4^+/SO_4^{2-} molar ratio in ACE 1 are less than 2 indicating that nss sulfate is only partially neutralized by low pressure of ammonia.

We use the individual organic compounds proposed by Ming and Russell (2001) to represent the composition of organic fraction of sea salt aerosol due to the absence of direct measurements. The model soluble compounds are malic acid (48% of total organic mass), citric acid (22% mass), glucose (4.8%) and fructose (4.7%), while the insoluble ones cover a set of long-chain alkanes, alkanols and acids (total 20.5%). The initial organic mass fractions of sulfate and sea salt aerosols are assumed to be 15% and 10% , respectively, regardless of sizes. Middlebrook et al. (1998) reported an estimated average organic fraction at Cape Grim during ACE 1 on the order of 10% with laser mass spectrometry. Huebert et al. (1998) found that 10 - 47% of the gravimetrical aerosol mass sampled during ACE 1 that cannot be explained by measured ionic mass may consist of organics. The organic fractions assumed in our model are consistent with these observations. The surface tension of droplets are assumed to agree with the measurements by Facchini et al (2000) that quantify the effect of organic components on surface tension in rural conditions. The predicted hygroscopic growth factors of both aerosols based on the compositions we use are in good agreement with measurements (Berg et al., 1997).

The initial gas-phase concentrations of DMS, SO_2 and H_2SO_4 used in our model are based on direct measurements (Bates et al., 1998b). The MBL in Flight 25 extends to 583 m (altitude) based on the Scanning Aerosol Backscatter Lidar (SABL) data (Russell et al., 1998). The SABL image of clouds observed in Flight 25 reveals the altitude of cloud base at around 450 m. The cloud top is at the same altitude as the top of MBL.

We used a typical updraft velocity of 0.5 m s^{-1} and measured lapse rate of 0.00214 K m^{-1}, which translate into a cooling rate of 3.85 K $hour^{-1}$ that is much greater than the cooling rate of 0.34 K $hour^{-1}$ encountered in our study of fog formation. In our model, the temperature of air parcel starts to decrease at this cooling rate once it rises above cloud base.

6.3 Results

The simulation covers a 12-hour duration starting from 8:00. The size distributions of both aerosols at 20:00 are compared with the initial distributions in Figure 6.1. Coagulation and wet deposition are the dominant microphysical processes in affecting particle sizes. The number concentration of sulfate aerosol with diameters less than 0.06 μm decreases by 7% due to coagulation. For coarse sea salt particles larger than 0.6 μm, the removal through wet deposition is expedited as a result of cloud formation outweighting the production rate. Consequently the number concentration of sea salt aerosol at 20:00 in that size range decreases by 8% as compared to that at 8:00. Unlike the polluted fog case, condensable gas species play a negligible role in altering particle size and composition due to their low concentrations in clean marine environment.

Figure 6.2: Profiles of predicted LWC (thin dashed lines) and supersaturation (thin solid lines) in marine cloud. The comparative case represented by the thick lines use purely inorganic compositions for sulfate and sea salt aerosols.

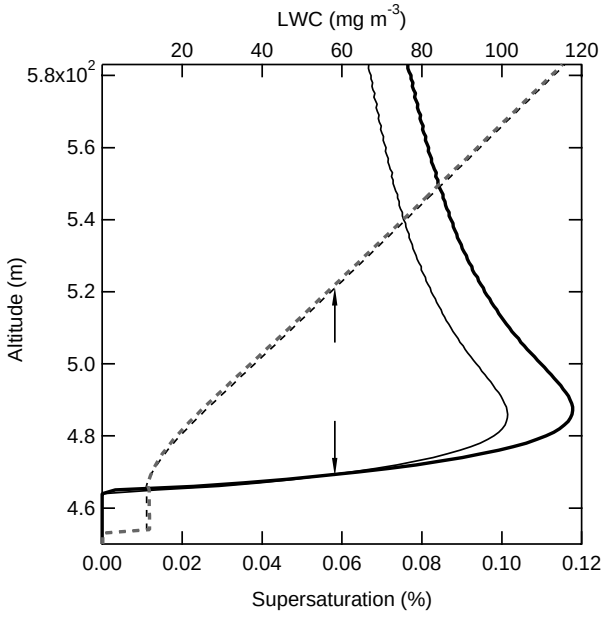

The simulated LWC and supersaturation are plotted against altitude in Figure 6.2. A rapid increase of supersaturation from 0% to 0.10% occurs in the region of 30 m from the cloud bottom. Then the supersaturation gradually decreases to 0.078% at the cloud top. The LWC in fog continuously increases starting from about 0 mg m^{-3} at the bottom to 116 mg m^{-3} at the top. The activation diameters of both aerosols are all 0.13 μm resulting an average CCN concentration of 90 cm^{-3}. The calculated LWC and CCN concentration are in agreement with measurements (Wang et al., 1999).

6.4 Sensitivity

In order to study the influence of organic components of aerosol on cloud formation, we run a comparative simulation treating sulfate and sea salt aerosol as mixtures of only inorganic salts. Meanwhile all other chemical and cloud microphysical conditions remain the same as in the base case. The predicted LWC and supersaturation in the comparative case are compared with those in the base run in Figure 6.2. The maximum supersaturation in the comparative case reaches 0.12%, higher than 0.10% in the base case with organic components present. Correspondingly the LWC in the comparative case is 1% lower than in the base case. The activation diameters of sulfate and sea salt aerosols in the comparative case are 0.15 and 0.19 μm, respectively, higher than 0.13 μm in the base case. Therefore the average CCN in the base case is 84 cm^{-3}, 6% lower than in the base case.

6.5 Discussion and Conclusions

Marine cloud in the clean conditions of ACE 1 differs from radiation fog in the polluted conditions of the Po Valley in two aspects. (1) As possible candidates for CCN under naturally occurring supersaturation, the particles larger than 0.1 μm in ACE 1 are 17 times more abundant than in the Po Valley. As a result of the competition between particles for absorbing liquid water, higher concentration of particles tends to suppress maximum supersaturation in cloud/fog. (2) The cooling rate of air parcel in ACE 1 is 11 times higher than in the Po Valley. As the driving force to sustain supersaturation necessary for cloud/fog formation, fast cooling has an effect of enhancing maximum supersaturation. Consequently the maximum supersaturation of cloud in clean environment is normally higher than that of fog under the influence of

pollution. Our model simulation confirms this conclusion: the predicted maximum supersaturations in ACE 1 and the Po Valley are 0.10% and 0.030%, respectively.

Our calculation shows that sea salt and nss sulfate aerosols contribute 63% and 37% of CNN in Flight 25, respectively. Only particles with diameters greater than 0.13 μm can activate to droplets at a maximum supersaturation of 0.10%. Covert et al. (1998) calculated the CCN concentrations at 0.5% supersaturation of the air flows sampled at Cape Grim during ACE 1 from the measured number size distributions and hygroscopic properties of aerosol. It was found that particles as small as 0.07 μm can act like CCN at 0.5% supersaturation and around 70% of CCN are particles with diameters between 0.08 and 0.2 μm, among which a large fraction may be derived from sea salt. The predicted activation diameter in our study (0.13 μm) is much larger than in Covert et al. (1998) due to the much lower supersaturation reached in our kinetic simulation of fog. Nonetheless both studies agree that sea salt is potentially a major source of CCN in clean marine environment.

There were field measurements showing that surface-active organic components in aerosol can greatly decrease the surface tension of resulting droplets as compared to pure water and purely inorganic solution (Facchini et al., 2000). Such an effect tends to lower the critical supersaturation necessary for aerosol particles of a specific size. On the other hand, organic solutes contribute less ions per unit mass than inorganic salts. In terms of the solvation effect in CCN activation, purely inorganic aerosol is more efficient than aerosol partially composed of organics. Our simulation shows that partially organic aerosol generates a CCN concentration 6% higher than purely inorganic aerosol indicating that the gain in CCN efficiency due to decreased surface tension, which assists in the activation of partially organic aerosol, outweights the loss in solvation. This conclusion is in agreement with a recent study by Mircea et

al. (2002), which estimated an increase of up to 13% in CCN concentration due to the presence of organic components in marine conditions.

References

Bates, T.S., B.J. Huebert, J.L. Gras, F.B. Griffiths, and P.A. Durkee, International Global Atmospheric Chemistry (IGAC) project's first aerosol characterization experiment (ACE 1): Overview, *J. Geophys. Res., 103,* 16297-16318, 1998a.

Bates, T.S., V.N. Kapustin, P.K. Quinn, D.S. Covert, D.J. Coffman, C. Mari, P.A. Durkee, W.J De Bruyn, and E.S. Saltzman, Processes controlling the distribution of aerosol particles in the lower marine boundary layer during the First Aerosol Characterization Experiment (ACE 1), *J. Geophys. Res, 103,* 16369-16383, 1998b.

Berg, O.H., E. Swietlicki, and R. Krejci, Hygroscopic growth of aerosol particles in the marine boundary layer over the Pacific and Southern Oceans during the First Aerosol Characterization Experiment (ACE 1), *J. Geophys. Res., 103,* 16,535-16,545, 1998.

Bowyer, P.A., D.K. Woolf, and E.C. Monahan, Temperature-dependence of the charge and aerosol production associated with a breaking wave in a whitecap simulation tank, *J. Geophys. Res., 95,* 5313-5319, 1990.

Covert, D.S., J.L. Gras, A. Wiedensohler, and F. Stratmann, Comparison of directly measured CCN with CCN modeled from the number-size distribution in the marine boundary layer during ACE 1 at Cape Grim, Tasmania, *J. Geophys. Res., 103,* 16597-16608, 1998.

Facchini, M.C., S. Decesari, M. Mircea, S. Fuzzi, and G. Loglio, Surface Tension of Atmospheric Wet Aerosol and Cloud/Fog Droplets in Relation to Their Organic

Carbon Content and Chemical Composition, *Atmos. Environ., 34,* 4853-4857, 2000.

Huebert, B.J., S.G. Howell, L. Zhuang, J.A. Heath, M.R. Litchy, D.J. Wylie, J.L. Kreidler-Moss, S. Coppicus, and J.E. Pfeiffer, Filter and impactor measurements of anions and cations during the First Aerosol Characterization Experiment (ACE 1) *J. Geophys. Res., 103,* 16493-16509, 1998.

Middlebrook, A.M., D.M. Murphy, and D.S. Thomson, Observations of organic material in individual marine particles at Cape Grim during the First Aerosol Characterization Experiment (ACE 1), *J. Geophys. Res., 103,* 16,475-16,483, 1998.

Mircea, M., M.C. Facchini, S. Decesari, S. Fuzzi, and R.J. Charlson, The Influence of the Organic Aerosol Component on CCN Supersaturation Spectra for Different Aerosol Types, *Tellus B, 54,* 74-81, 2002

Ming, Y., and L.M. Russell, Thermodynamic equilibrium of aqueous solutions of organic-electrolyte mixtures in aerosol particles, *AIChE J.*, submitted, 2001.

Murphy. D.M., J.R. Anderson, P.K. Quinn, L.M. McInnes, F.J. Brechtel, S.M. Kreidenweis, A.M. Middlebrook, M. Posfai, D.S. Thomson, P.R. Buseck, Influence of sea-salt on aerosol radiative properties in the Southern Ocean marine boundary layer, *Nauture, 392,* 62-65, 1998.

Quinn, P.K., D.J. Coffman, V.N. Kapustin, T.S. Bates, D.S. Covert, Aerosol optical properties in the marine boundary layer during the First Aerosol Characterization Experiment (ACE 1) and the underlying chemical and physical aerosol properties, *J Geophys. Res, 103,* 16547-16563, 1998.

Russell, L.M., D.H. Lenschow, K.K. Laursen, P.B. Krummel, S.T. Siems, A.R. Bandy, D.C. Thornton, and T.S. Bates, Bidirectional mixing in an ACE 1 marine boundary layer overlain by a second turbulent layer, *J. Geophys. Res, 103,* 16411-16432, 1998.

Russell, L.M., K.J. Noone, R.J. Ferek, R.A. Pockalny, R.C. Flagan, J.H. Seinfeld, Combustion organic aerosol as cloud condensation nuclei in ship tracks, *J. Atmos. Sci., 57,* 2591-2606, 2000.

Russell, L.M., and J.H. Seinfeld, Size- and Composition-resolved Externally Mixed Aerosol Model, *Aerosol Sci. Tech., 28,* 403-416, 1998.

Wang, Q., K. Suhre, P. Krummel, S. Siems, L.L. Pan, T.S. Bates, J.E. Johnson, D.H. Lenschow, B.J. Heubert, G.L. Kok, R.D. Schillawski, A.S.H. Prevot, and S. Businger, Characteristics of marine boundary layers during two Lagrangian measurement periods 1. General conditions and mean characteristics, *J Geophys. Res., 104,* 21751-21765, 1999.

Chapter 7

Influence of Health-based Policy on Climate

7.1 Model

The Dynamic Integrated Climate-Economy (DICE-99) model (Nordhaus and Boyer, 2000) has been widely used as a policy tool to study the optimal path of green-house gases (GHG) reduction. By maximizing utility of per capita consumption, the model weights the tradeoff between damage caused by global warming and abatement cost. A simplified model of CO_2 cycle and climate predicts its atmospheric concentration, and global mean temperature. DICE-99 also considers the negative radiative forcing of sulfate aerosol as an exogenous variable that parameterizes a specific scenario of economic and social development in affecting global mean temperature. We have modified DICE-99 to include sulfur emission as an endogenous variable that is adjusted to environmental damage and cost of control. In addition to carbon abatement cost and damage caused by global warming already considered by DICE-99, sulfur abatement cost and human health damage due to particulate matter (PM) are also deducted from total economic output.

Emissions Both CO_2 and sulfate aerosol largely result from burning fossil fuels, which is responsible for 84% of CO_2 emission (Subak et al., 1993) and 92% of sulfur emission (Spiro et al., 1992). Consequently both emissions are significantly correlated. Carbon emission is proportional to sulfur emission prior to separate sulfur control specifically targeting sulfur (i.e. scrubbers). This assumption implies that any approach to cut carbon emission through reducing fossil fuel consumption will cut sulfur emission to the same extent.

$$E_S(t) = R_{SC}(t)E_C(t)(1 - \mu_S(t)) \tag{7.1}$$

$E_C(t)$ and $E_S(t)$ denote the carbon and sulfur emissions in period t, while R_{SC}(t) and $\mu_S(t)$ are the sulfur/carbon ratio and sulfur control rate in period t, respectively. In our model, the annual anthropogenic emissions of carbon and sulfur in 1990 are estimated at 6.18 GtC (Wigley, 1991) and 0.071 GtS (Wigley and Raper, 1992), respectively. Natural gas has increased its share of energy supply recently, providing low carbon intensity (CO_2 emission per unit energy) and high efficiency for gas turbines. Fuel switching from coal to gas reduces the ambient concentration of sulfate aerosol, because natural gas has very low sulfur content. We use the projected energy structure in the IPCC SRES B2 scenario (IPCC, 2000) to construct time-dependent sulfur/carbon ratio and find that fuel switching decreases sulfur/carbon ratio from 0.0114 in 1990 to 0.0078 in 2070. Coal begins to regain some market share after 2070 and increases sulfur/cabon ratio back to 0.012 in 2100 (Figure 7.2(a)). The use of alternatives like renewable energy and carbon sequestration produce neither CO_2 nor sulfate aerosol so that their use as a control strategy does not affect this ratio.

Radiative Forcing and Health Effects Radiative forcing due to non-CO_2 GHGs and sulfate aerosol is treated by DICE-99 as exogenous starting from -0.06

W m^{-2} in 1990 and monotonically increases to 1.15 W m^{-2} by 2100 (Nordhaus and Boyer, 2000). In our model, we use a similar approach for non-CO_2 GHG except that the direct radiative forcing of sulfate aerosol is calculated as a linear function of emission (Wigley, 1991):

$$F_{S,dir}(t) = \frac{E_S(t)}{E_S(0)} F_{S,dir}(0) \tag{7.2}$$

$F_{S,dir}(t)$ is the direct radiative forcing of sulfate aerosol in period t. $F_{S,dir}(0)$ in 1990 is estimated at -0.4 W m^{-2} (IPCC, 2001). A logarithmic function is used to simulate the indirect radiative of sulfate aerosol (Wigley, 1991).

$$F_{S,indir}(t) = \frac{1 + \ln(\frac{E_S(t)}{E_{S,o}})}{1 + \ln(\frac{E_S(0)}{E_{S,o}})} F_{S,indir}(0) \tag{7.3}$$

$F_{S,indir}(t)$ is the indirect radiative forcing of sulfate aerosol in period t. $F_{S,indir}(0)$ in 1990 is estimated at -0.5 W m^{-2} (Wigley, 1991). $E_{S,o}$ is the natural emission of sulfur, which is taken to be constant as 0.042 GtS annually (Wigley, 1991). The model assumes that all forcings are linear and globally homogenous.

The $PM_{2.5}$ concentration represents the mass concentration of ambient suspended particles with diameter less than 2.5 μm and represented here as approximately proportional to emissions (Pearce and Crowards, 1996):

$$PM_{2.5}(t) = \frac{E_S(t)}{E_S(0)} PM_{2.5}(0) \tag{7.4}$$

The global average $PM_{2.5}$ weighted by population in 1990 is estimated at 6.2 μg m^{-3} (Davis et al., 1997). Because the life time of sulfate aerosol (days) is much shorter than the time step used in this model (10 years), Equation 7.4 implicitly assumes that sulfate aerosol is instantaneously removed from the atmosphere.

The dose-response function (DRF) of PM_{10} (particles smaller than 10 μm) has been measured to be 1 μg m^{-3} PM_{10} concentration for every 1% increase in mortality (Ostro, 1994). The ratio of $PM_{2.5}$ to PM_{10} in the urban area is estimated at 0.55 (Pope et al., 1995). The derived dose-response function of $PM_{2.5}$ is 1 μg m^{-3} concentration responsible for 1.8% increase in mortality given that health damage is most probably caused by $PM_{2.5}$. The number of human lives lost as a result of particulate matter is calculated as

$$L(t) = b(PM_{2.5}(t) - PM_{2.5}(0))r_M P(t) \tag{7.5}$$

$L(t)$ is the number of lives lost out of the total population $P(t)$ in period t. r_M is the world average mortality rate (0.08%), while b is the DRF constant (1.8%).

The willingness-to-pay method is used to estimate the value of a statistical life (VOSL). Pearce et al. (1994) calculated VOSL for the United Kingdom at 2 million pounds. The estimated VOSL for the United States ranges from 1.2 million dollars to 10.7 million dollars (1990) (World Bank, 1998). This model uses a VOSL of 4 million (1990) for the United States (PACE, 1992). The current and future world average VOSL is adjusted by the ratio of the world average per capita GDP to the per capita GDP in the United States (Markandya, 1994; El-Fadel and Massoud, 2000). The derived world average VOSL is 0.62 million dollars (1990) in 1995.

Abatement Cost Halkos (1994) derived the least cost curves of sulfur abatement with main desulfurization technologies for European countries and found that marginal abatement cost monotonically increases with sulfur control rate. The increase in abatement cost results from resorting to more expensive abatement options after cheaper options have been utilized to control emissions at low control rate. Abatement cost increases drastically as reduction approaches the maximum feasible

Table 7.1: Economic damages and abatement methods in alternative policies.

Case	Control measure(s)	Sulfur emission
No-control	None	Indogenous
IPCC	Fixed sulfur control	The same as in SRES B2
C	Free carbon and fixed sulfur controls	The same as in SRES B2
S	Free sulfur control	Indogenous
CS	Free carbon and sulfur controls	Indogenous

control rate (around 80%). This model uses the cost function of sulfur abatement derived for the UK in Halkos (1994).

7.2 Results

In the policy alternatives summarized in Table 7.1, the optimal paths of carbon and sulfur emissions are calculated by maximizing discounted per capita utility subject to climate and health damages and available control measures. In the no-control case no effort is made to reduce carbon and sulfur emissions for the purpose of mitigating global warming and adverse health effect, while only investment rate is optimized to reduce associated economic damages. The exogenous path of sulfur emission used in the IPCC case is the same as in the IPCC SRES B2 scenario (IPCC, 2000), which implicitly assumes some degree of sulfur emission. The C case employs free carbon control to abate global warming with the exogenous path of sulfur emission in the B2 scenario. The S case allows for only free sulfur control, while both free carbon and free sulfur controls are available as policy tools in the CS case.

The carbon emission increases from 6.3 GtC in 1995 to 12.9 GtC in 2105 (Figure 7.1(e)) in the no-control case. Due to the absence of sulfur control, the sulfur emission in 2105 accordingly stands at 0.145 GtS, more than twice of the 1995 level of

0.070 GtS (Figure 7.1(f)). The global mean temperature increase since pre-industrial times amounts to 2.18 °C in 2105 (Figure 7.1 (a)).

The carbon emission in the IPCC case starts from 6.3 GtC in 1995, and increases to 13.0 GtC in 2105 (Figure 7.1(e)), only slightly higher than in the no-control case, while the sulfur emission follows the fixed path in the SRES B2 scenario by decreasing gradually from 0.070 GtS in 1995 to 0.048 GtS in 2015 (Figure 7.1(f)). As compared to the no-control case, the much lower sulfur emission in the IPCC case reduces the cooling effect of sulfate aerosol and causes an temperature increase of 2.59 °C in 2105, considerably higher than 2.18 °C in the no-control case.

The carbon emission in the C case is reduced in order to abate the economic cost due to global warming, while the sulfur emission remains controlled to the same extent as in the IPCC case. The projected carbon emission in 1995 instantaneously drops to 6.0 GtC as compared to 6.3 GtC in the no-control and IPCC cases (Figure 7.1(e)). Then it grows to 11.4 GtC in 2105, 12% lower than in the IPCC cases. The decreased carbon emission slows down the accumulation of CO_2. Consequently the temperature increase in 2105 is 2.49 °C as compared to 2.59 °C in the IPCC case.

The IPCC and C cases in this study conceptually correspond to the business-as-usual (BAU) and optimization cases in Nordhaus and Boyer (2000), respectively, differing only in the reduction of total economic output due to health damage and sulfur control cost. The differences between the results of two studies are well within 1%. Our reruns of the BAU and optimization cases with the current model parameters reveal no appreciable (well within 1%) difference with the IPCC and C cases.

Sulfur control allows the partial decoupling of carbon and sulfur emissions in the sense that the amount of sulfur emitted into the atmosphere is not necessarily proportional to the corresponding carbon emission. As the only policy option available

Figure 7.1: Projected global mean temperature (a), carbon emission (b), sulfur emission (c), marginal cost of carbon emission (d), marginal cost of sulfur emission (e), per capita consumption (f) and health cost (g) in different policies: No-control (solid line), IPCC (dotted line), C (dashed line), S (dotted-dashed line), and CS (dotted-dotted-dashed line).

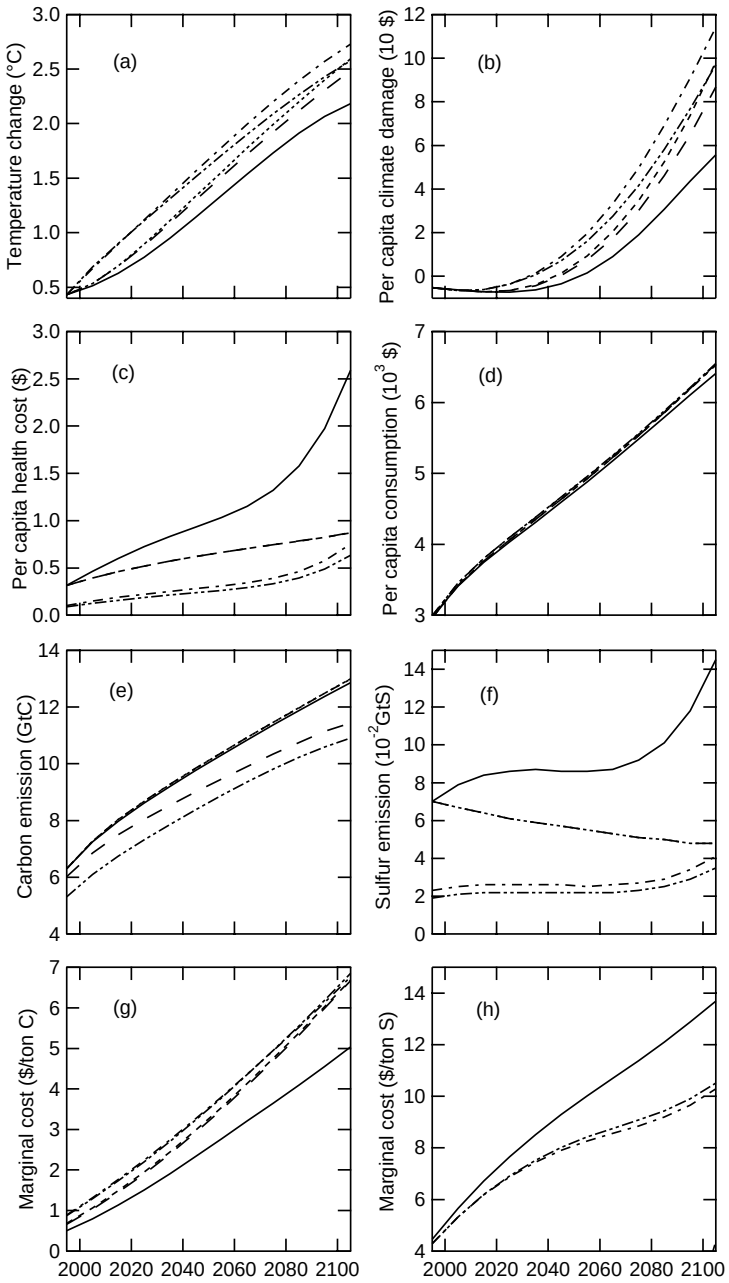

in the S case, sulfur control can be used to abate sulfur emission to lower health cost. The reduced sulfur emission is 0.023 GtS in 1995 and increases to 0.041 GtS in 2105 (Figure 7.1(f)). The lack of carbon control gives rise to carbon emission level close to that in the IPCC case (Figure 7.1(e)). The deeply reduced sulfur emission weakens the cooling effect of sulfate aerosol and, together with high CO_2 emission, exacerbates global warming so that the temperature increase goes up to 2.73 °C in 2105 (Figure 7.1(a)).

Besides reducing carbon emission, the carbon control in the CS case is also capable of lowering sulfur emission, unlike the S case with only sulfur control. Consequently the sulfur emission is 0.019 GtS in 1995 and increases to 0.035 GtS in 2105, 14% lower than the S case. Due to the same reason the optimal carbon emissions are 5.3 in 1995 and 10.9 GtC in 2105, 7% lower than the C case that assumes a fixed path of inadequate sulfur control. Both the carbon and sulfur emissions in the CS case are considerably lower than in the IPCC case. The reduced carbon emission slows down the accumulation of CO_2 in the atmosphere, and thus cools the Earth's climate. On the other hand, the weakened cooling effect of sulfate aerosol due to lower sulfur emission tends to warm the climate. As a result of short lifetime of sulfate aerosol, its effect determines the short-term temperature trend in the CS case. Consequently the temperature from 1995 to 2095 in the CS case is 0.13 °C higher than in the IPCC case. Thereafter the effect of slower accumulation of CO_2 becomes dominant and brings the temperature in the CS case lower than in the IPCC case.

The marginal costs of carbon and sulfur emissions are plotted in Figure 7.1(g) and Figure 7.1(h), respectively. In Figure 7.1(h), the marginal cost of sulfur in the no-control case is as high as 11000 $/ton S due to the high health cost and limited approach to abate sulfur emission. Sulfur control greatly reduces the abatement cost

and lower marginal cost to 8000 $/ton S in the S and CS cases.

Two test cases are used to assess the extent to which these results rely on our assumptions of sulfur/carbon ratio and VOSL. The CS-R (Climate and Health effects with Carbon and Sulfur controls using constant sulfur/carbon Ratio) assumes that the carbon/sulfur ratio R_{SC} in Equation 7.1 remains at the 1990 level for the next 100 years (Figure 7.2(a)). The carbon emission with varying ratio in the CS case is consistently higher than that with constant ratio in the CS-R case (Figure 7.2(c)), while the sulfur emission in the CS case is lower than that in the CS-R case due to higher sulfur/carbon ratio in the CS-R case. Consequently the temperature increase in 2105 in the CS-R case is 2.50 °C, lower than 2.60 °C in the CS case (Figure 7.2(b)).

VOSL is important for pricing health cost, while its value is subject to uncertainty. The CS-V (Climate and Health effects with Carbon and Sulfur controls using lower VOSL) case uses a reduced world average VOSL of 0.2 million. Reduced health cost (CS-V) leads to higher carbon and sulfur emissions than using 0.62 million as VOSL (CS) (Figure 7.2(c) and Figure 7.2(d)). The sulfur emission for the low VOSL (CS-V) in 2105 amounts to 0.062 GtS, which is much higher than 0.035 GtS in the CS case. The lower health costs (CS-V) allow higher sulfate aerosol emission that enhance cooling and reduce global warming to 2.5 °C increase in 2105 as compared to 2.60 °C in the CS case (Figure 7.2(b)).

7.3 Discussion

Hansen et al. (2000) and Manne and Richels (2001) have argued that short-lived CH_4 and N_2O may provide important policy targets for limiting the rate of temperature change in the twenty-first century. Our integrated-assessment model shows that

Figure 7.2: Sensitivity studies with constant sulfur/carbon ratio and low VOSL. Varying (squares) and constant (circles) sulfur/carbon ratios (a), projected global mean temperature (b), carbon emission (c), sulfur emission (d), per capita consumption (e) and health cost (f) in CHCS (solid line), CHCS-R (dotted line) and CHCS-V (dashed line).

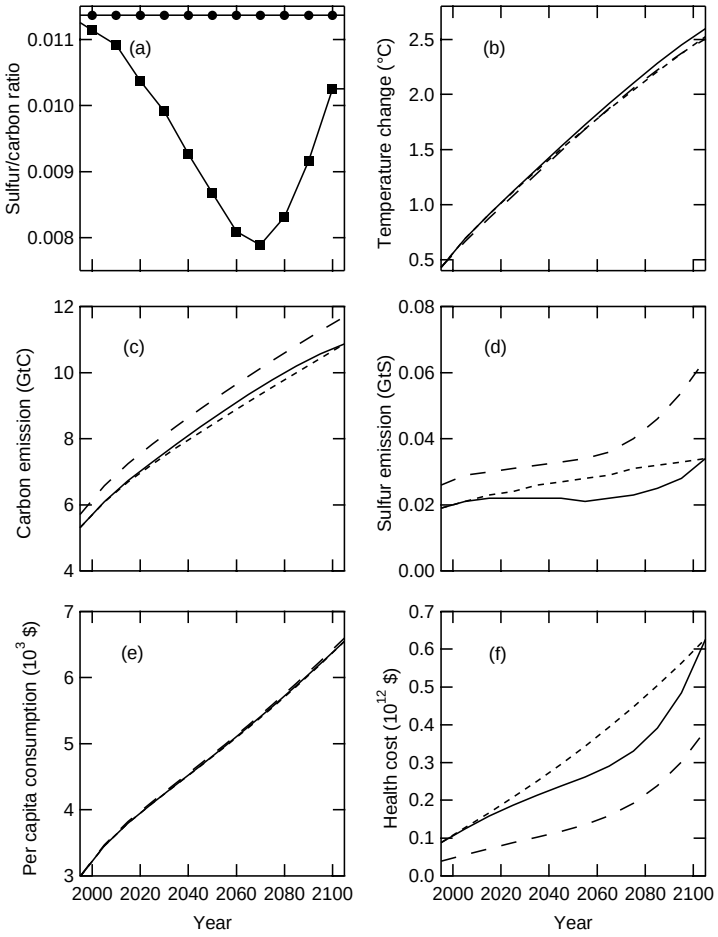

policy will also depend strongly on the emissions of sulfate aerosol because of both their radiative cooling and their detrimental health effects. The negative forcing of sulfate aerosol is capable of lessening global warming, and thus makes sulfate aerosol an important player in determining the trend in future temperature. In the IS92a scenario (Alcamo et al., 1995), sulfur emission continues to rise until it reaches 0.15 GtS in 2050 and stays relatively constant thereafter, doubling the current emission of 0.071 GtS. Though the SRES scenarios reflect a variety of paths in terms of social and economic development and covers a wide range of carbon emissions (between 4 and 30 GtC in 2100), the corresponding sulfate emissions are all lower than the current level to different extents (between 0.02 and 0.06 GtS). The incentive for projected reduction in sulfate emission is the improved air quality and resulting gain in human health (IPCC, 2000).

Our results show that allowing sulfur control (S and CS) significantly lowers sulfur emissions relative to the no-control case that does not have sulfur control as policy option and the SRES B2 scenario. Carbon and sulfur controls (CS) are capable of cutting sulfur emission to 0.019 GtS in 1995 and 0.035 GtS in 2105, a range comparable to the SRES scenarios (IPCC, 2000). These reductions optimize investment, since their high health costs outweight the benefits of mitigating global warming that results from its cooling effect.

Tremendous efforts have been made both by developed countries and by developing countries to curb the emissions of atmospheric pollutants including sulfate (Hao et al., 2000). The reduction in sulfur emission has been realized partially through reducing fossil fuel consumption. Despite the consequent short-term temperature increase, the effect of sulfate aerosol to preclude health damage reduces the accumulation of CO_2. The only strategy to avoid the short term (1995 - 2105) increase in global mean

temperature has been proposed by Hansen et al. (2000) – namely methane reduction. The long term impact of sulfate aerosol controls after 2105 is to lower temperature.

References

Alcamo, J., A. Bouwman, J. Edmonds, A. Grbler, T. Morita, and A. Sugandhy, 1995: An evaluation of the IPCC IS92 emission scenarios, in *Climate Change 1994, Radiative Forcing of Climate Change and An Evaluation of the IPCC IS92 Emission Scenarios*, J.T. Houghton, L.G. Meira Filho, J. Bruce, Hoesung Lee, B.A. Callander, E. Haites, N. Harris and K. Maskell (eds.), Cambridge University Press, Cambridge, pp. 233- 304.

Davis, D.L., Kjellstrom, T., Slooff, R., McGartland, A., Atkinson, D., Barbour, W., Hohenstein, W., Nagelhout, P., Woodruff, T., Divita, F., Wilson, J. and Schwartz, J., Short-term improvements in public health from global-climate policies on fossil-fuel combustion: an interim report,*LANCET*, 350, 1341, 1997.

El-Fadel, M., and Massoud, M., Particulate matter in urban areas, health-based economic assessment, *The Science of the Total Environment*, 257, 133, 2000.

Florig, H.K., *The Benefits of Air Pollution Reduction in China*, Resources for the Future, Washington, DC, 1993.

Halkos, G.E., Evaluation of the direct cost of sulfur abatement under the main desulfurization technologies, *Energy Sources*, 17, 391, 1994.

Hansen, J., Sato, M., Ruedy R., Lacis A., and Oinas, V., Global warming in the twenty-first century: An alternative scenario, *Proc. Natl. Acad. Sci.*, 97, 9875, 2000.

Hall, J.V., Winer, A.M., Kleinman, M.T., Lurmann, F.W., Brajer, V. and Colome, S.D., Valuing the health Benefits of clean air, *Science*, 255, 812, 1992.

Hao, J.M., Wang, S.X., Liu, B.J. and He, K.B., Designation of acid rain and SO2 control zones and control policies in China, *J. Environ. Sci. and Health A*, 35, 1901, 2000.

IPCC, *Third Assessment Report: The Scientific Basis*, R.T. Watson and the Core Writing Team (eds.), Cambridge University Press, UK, 2001.

IPCC, *Special Report Emission Scenairos*, N. Nakicenovic and R. Swart (eds.), Cambridge University Press, UK, 2000.

Manne, A.S., and Richels, R.G., An alternative approach to establishing trade-offs among greenhouse gases, *Nature*, 410, 675, 2001.

Markandya, A., Measuring the External Costs of Fuel Cycles in Developing Countries, in *Social Costs of Energy*, O. Hohmeyer and R.L. Ottinger (eds.), Springer-Verlag, Berlin, 1994.

Nordhaus, W.D. and Boyer, J., *Warming the World: Economic Models of Global Warming*, MIT Press, Cambridge, MA, 2000.

PACE, Environmental Costs of Electricity, PACE University Centre for Environmental Legal Studies. Prepared for the New York State Energy Research and Development Authority and the US Department of Energy, 1992.

Pearce, D., and Crowards, T., Particulate matter and human health in the United Kingdom, *Energy Policy*, 24, 609.

Pope, C.A., III, Thun, M.J., Namboodiri, M.M., Dockery, D.W., Evans, J.S., Speizer, F.E. and Heath, C.W., Jr. Particulate Air Pollution as a Predictor of Mortality in a Prospective Study of U.S. Adults, *Am. J. Respir. Crit. Care Med.*, 151, 669, 1995.

Spiro, P.A., Jacob, D.J., and Logan, J.A., Global inventory of sulfur emission with $1^\circ \times 1^\circ$ resolution, *Journal of Geophysical Research*, 97, 6023, 1992.

Subak, S., Raskin, P., and von Hippel, D., National greenhouse gas accounts: current anthropogenic sources and sinks, *Climatic Change*, 25, 15, 1993.

Wigley, T.M.L., Could reducing fossil-fuel emissions cause global warming?, *Nature*, 349, 503, 1991.

Wigley, T.M.L., and Raper S.C.B., Implications for climate and sea level of revised IPCC emissions scenarios, *Nature*, 357, 293, 1992.

World Bank, The effects of pollution on health: the economic toll, *Pollution Prevention and Abatement Handbook*, 1998.

Chapter 8

Suggestions for Future Research

(1) The thermodynamic model we have developed can satisfactory predict the hygroscopic properties of different types of aerosol containing organic components. Future effort should be made to incorporate this model into general circulation models (GCM) to achieve a precise calculation of liquid water associated with organic aerosol.

(2) Our model solves for the amount of water absorbed by particles at a given RH with an optimization algorithm that searches for the minimum Gibbs free energy. In order to integrate this process into GCM, the model has to be appropriately parameterized to reduce its running time. Such a parameterization has to be computationally efficient while retaining much of the model accuracy.

(3) A global inventory of primary sources of organic aerosol is necessary for modeling organic aerosol on the global scale for the purpose of climate research. Such an inventory should be able to be used to calculate the concentrations of various types of aerosol in the atmosphere and provide valuable information about their chemical compositions, such as polarity and solubility.

(4) An important source of organic aerosol is the gas-to-particle conversion such

as the formation of secondary organic aerosol (SOA). The resulting organic products from photochemical reactions are usually water-soluble, and thus make aerosol particles hydrophilic. Effort should be devoted to understanding the chemical composition of SOA and modeling its hygroscopic property.